NTNU – Trondheim
Norwegian University of
Science and Technology

Development of Asymmeteric Membranes for Oxygen Separation by Tape Casting and Dip Coating

Belma Talic

Chemical Engineering and Biotechnology
Submission date: June 2013
Supervisor: Kjell Wiik, IMTE
Co-supervisor: Jonas Gurauskis, IMTE
Ørjan Fossmark Lohne, IMTE
Hilde Lea Lein, IMTE

Norwegian University of Science and Technology
Department of Materials Science and Engineering

Declaration

I hereby declare that the work presented in this document has been performed independently and in accordance with the rules and regulations of the Norwegian University of Science and Technology (NTNU).

Trondheim, 23. June 2013

Belma Talić

Preface

This thesis is submitted to the Norwegian University of Science and Technology (NTNU) as part of the requirements for the degree of Master of Science ("Sivilingeniør"). The work presented has been carried out at the Department of Materials Science and Engineering at NTNU during the spring of 2013.

First of all I want to thank my main supervisor, Kjell Wiik, for his support and encouragement during these past months. My co-supervisors Ørjan Fossmark Lohne, Hilde Lea Lein and Jonas Gurauskis have also been very helpful and provided me with guidance through the day-to-day lab work. I want to thank Ørjan Fossmark Lohne especially for always keeping an open door and being available for discussions. The rest of the members of the Ceramics group have been valuable for various discussions related to this thesis and their help has been much appreciated. In addition, I want to thank the technical staff at IMT for help with equipment training and acknowledge Eli-Beate Larsen for performing the thermal analysis of my samples.

The past months would not have been as enjoyable if it were not for my classmates. Thanks for all the coffee breaks, monday–cakes on tuesdays and conversations about the most peculiar subjects. I also want to thank Sivert for diverting my mind off this thesis and for always finding a way to make me laugh.

Finally, to my family: hvala što ste uvijek vjerovali u mene.

Abstract

Ceramic membranes made from mixed ionic and electronic conductive oxide materials have received much attention over the last decade due to their ability to separate oxygen from air at 100 % selectivity. The flux through these membranes may be optimized by reducing their thickness. A porous support of the same composition is applied to ensure sufficient mechanical stability. The processing of these so-called asymmetric membranes is addressed in this work; for the technology to become attractive from a commercial point of view, a reliable and cost-effective processing procedure needs to be established.

Phase pure $La_{0.2}Sr_{0.8}Fe_{0.8}Ta_{0.2}O_{3-\delta}$ (LSFTa) and $La_{0.2}Sr_{0.8}Fe_{0.8}Al_{0.2}O_{3-\delta}$ (LSFAl) powders were synthesized by solid state reaction. The powders were used to prepare porous supports by the means of aqueous based tape casting and hot-press lamination. The supports were pre-sintered at various temperatures and dip coated with an ethanol-based suspension containing sub-micrometer sized spray pyrolysis powder. Different parameters believed to affect dense layer formation by dip coating are discussed and related to the experimental observations. It was found that an important criteria for success is to have a similar shrinkage property in the functional and porous layer of the membrane. The most promising asymmetric membrane was obtained for the LSFTa composition where dip coating two times and sintering at 1230°C resulted in a 6–7 μm thick membrane layer and a support with 38 % open porosity.

The fracture strength of LSFAl supports with $\sim$ 64 % porosity was also characterized in this work. Testing 11 specimens with the ball-on-ring method resulted in a characteristic strength of 10.7$\pm$0.5 MPa and a Weibull modulus of 5.9$\pm$1.8.

Sammendrag

Keramiske membraner laget av blandede ionisk og elektronisk ledende oksider er ansett som en potensiell billig og miljøvennlig måte å utvinne 100 % rent oksygen på. Fluksen gjennom disse membranene kan optimaliseres ved å redusere tykkelsen deres. For å sikre tilstrekkelig mekanisk styrke kan man da bruke en porøs bærer av samme sammensetning. Fremstillingen av såkalte asymmetriske membranene er fokus for dette arbeidet; for at denne teknologien skal kunne bli kommersielt attraktiv er det nødvendig å etablere en pålitelig og kostnadseffektiv fremstillingsprosedyre for membranene.

Ved hjelp av faststoffsyntese ble det fremstilt faserene $\mathrm{La_{0.2}Sr_{0.8}Fe_{0.8}Ta_{0.2}O_{3-\delta}}$ (LSFTa) og $\mathrm{La_{0.2}Sr_{0.8}Fe_{0.8}Al_{0.2}O_{3-\delta}}$ (LSFAl) pulver. Disse pulverne ble brukt i fremstillingen av de porøse bærerne gjennom båndstøping og laminering. Bærerne ble varmebehandlet ved ulike temperaturer og dypp-belagt med en etanol-basert suspensjon som inneholdt spraypyrolysepulver av mikrometerstørrelse. Ulike parametre som antas å påvirke dannelsen av et tett lag gjennom dyppbelegging er diskutert og relatert til de eksperimentelle observasjonene. Det ble vist at en viktig forutsetning for denne metoden er at det porøse og det funksjonelle laget har lignende krympeegenskaper. Den mest lovende asymmetriske membranen ble fremstilt fra LSFTa sammensetningen: dypping i to omganger og en endelig varme-behandling ved 1230°C resulterte i et 6–7 μm tykt funksjonelt lag og en bærer med 38 % åpen porøsitet.

Bruddstyrken til LSFAl-bærere med 64 % porøsitet ble også undersøkt i dette arbeidet. Testing av 11 prøver med "ball-on-ring"-metoden resulterte i en karakteristisk styrke på 10.7$\pm$0.5 MPa og en Weibull modulus lik 5.9$\pm$1.8.

Table of Contents

List of symbols

Symbol	Notation	Unit
a	Radius of specimen support	mm
b	Radius of uniform loading	mm
η	Viscosity	$\mathrm{Pa} \cdot \mathrm{s}$
ϵ	Electric permittivity	F/m
E	Electric field	N/C
$\mathrm{E_a}$	Activation energy	kJ/mol
F	Probability for failure	%
γ	Surface tension	mN/m
$\mathrm{J_{O_2}}$	Oxygen permeability flux	$\mathrm{ml/min \cdot cm^2}$
ν	Poisson 's ratio	–
δp	Capillary pressure	Pa
m	Weibull modulus	–
P	Load	N
$\mathrm{P_{O_2}}$	Oxygen partial pressure	atm
ρ	Density	$\mathrm{m^2/g}$
r	Specimen radius	mm
R	Pore radius	m
σ	Applied stress	MPa
σ_0	Normalizing stress parameter	MPa
σ_{max}	Maximum tensile stress	MPa
σ_U	Stress at zero probability for failure	MPa
θ	Angle	–
t	Specimen thickness	mm
T	Temperature	K or °C
v	Particle velocity	m/s
V	Volume (fraction)	–
ζ	Zeta potential	mV

BET	Brunauer-Emmett-Teller
CB	Carbon Black
CR	Controlled rate
CR	Cooling rate
DIL	Dilatometry
DLVO	Derjaguin, Landau, Verwey and Overbeek
EDS	Energy dispersive X-ray spectroscopy
HR	Heating rate
IEP	Isoelectric point
LSFAl	$La_{0.2}Sr_{0.8}Fe_{0.8}Al_{0.2}O_{3-\delta}$
LSFTa	$La_{0.2}Sr_{0.8}Fe_{0.8}Ta_{0.2}O_{3-\delta}$
MIEC	Mixed ionic and electronic conductive
PE	Polyethylene
PEG	Poly(ethylene glycol)
PMA	Poly(methyl acrylate)
PVA	Poly(vinyl alcohol)
PVP	Poly(vinyl pyrrolidone)
PZC	Point of zero charge
rpm	Rounds Per Minute
SEM	Scanning Electron Microscopy
SP	Spray pyrolysis
SSR	Solid state reaction
ST	Sintering temperature
syngas	Synthesis gas
temp.	Temperature
TGA	Thermogravimetric analysis
XRD	X-ray diffraction
YSZ	Yttrium Stabilized Zirconia

Chapter 1

Introduction

1.1 Background

Dense ceramic membranes based on mixed ionic and electronic conductive (MIEC) materials have received much attention over the last decade due to their ability to separate oxygen from air at elevated temperatures (> 700°C) with 100 % selectivity [1, 2]. One of the most promising applications for this technology is in the production of syngas by partial oxidation of methane. By combining the oxygen permeable membrane and the catalytic reaction reactor in a single unit, the cost of syngas production is expected to be reduced by 25–30 % [3].

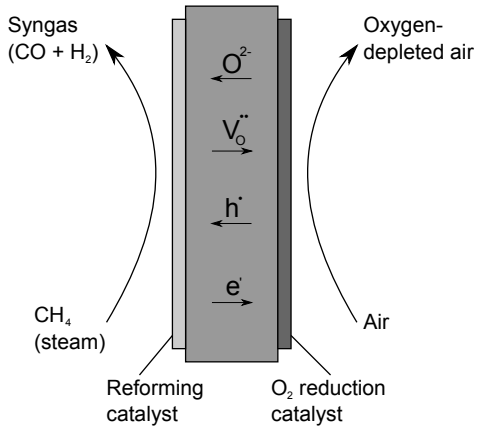

Figure 1.1: Principle of the MIEC oxygen permeable membrane. Redrawn from [4]

The principle of a MIEC-type oxygen permeable membrane utilized for the production of syngas is sketched in Figure 1.1. The driving force for oxygen transport is a chemical potential difference created by the difference in oxygen partial

pressure across the membrane. The oxygen permeation flux is controlled by two factors: (1) the bulk diffusion of oxide ions and (2) the oxygen exchange reactions taking place on the membrane surface [5]. When the rate is under bulk diffusion control the flux will increase linearly with decreasing membrane thickness until the rate becomes completely limited by the surface exchange reaction and there is no further improvement in the flux. This is illustrated in Figure 1.2. At some critical thickness the rate is equally limited by bulk diffusion and the surface exchange reactions [6]. The magnitude of this critical thickness will depend upon the material composition and microstructure, the operating temperature and partial pressure difference, but typical values are found within the range of a few micrometers and a few millimeters [7]. The obvious way to improve the performance of these membranes it thus to reduce their thickness below the critical value. In order to do so, a so-called asymmetric membrane consisting of thin, dense layer deposited on a highly porous support is developed [2, 7]. To ensure thermal and chemical compatibility, the two layers are usually prepared from the same material [8, 9]. In order not to limit the overall oxygen transport across the membrane, the support layer needs to show sufficient air permeability, i.e. the support layer needs to be sufficiently porous.

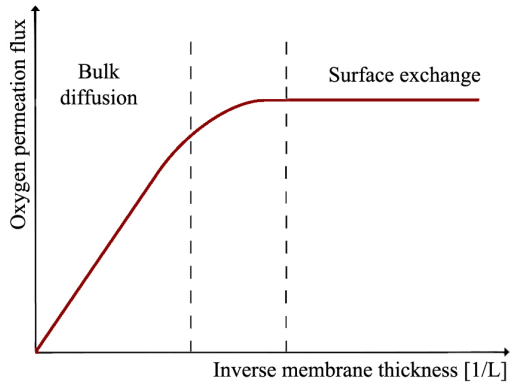

Figure 1.2: The flux of oxygen through a MIEC-membrane as a function of membrane thickness, L. Note that this illustration is of a simplified, ideal case. Redrawn from [2]

Teraoka et al. were the first to report on the high mixed ionic and electronic conductivity of the $La_{1-x}Sr_xCo_{1-y}Fe_yO_{3-\delta}$ perovskites, and since then extensive research has been focused on similar compositions [10]. The oxygen flux

may be increased by increasing the substitution of La with Sr, but this approach has the disadvantage of destabilizing the perovskite structure [11]. Stability is an especially important issue for membranes intended for syn-gas production because of the harsh operating conditions in both reducing (methane) and oxidizing (air) environments[12]. The stability may however be increased by partial substitution of the B-site cation. This is employed in the perovskites of the $La_{0.2}Sr_{0.8}Fe_{0.8}Ta_{0.2}O_{3-\delta}$ (LSFTa) and $La_{0.2}Sr_{0.8}Fe_{0.8}Al_{0.2}O_{3-\delta}$ (LSFAl) compositions, where partial substituting on the B-site with Ta and Al, respectively, has proven to stabilize the high amount of strontium in the composition [11]. Both of these materials have also been reported to have promising oxygen permeation fluxes [13, 14, 15].

1.2 Aim of work

One issue that needs to be solved before the oxygen permeable membrane can be commercialized is cost connected to production. The focus of this work is therefor to develop asymmetric membranes based on the LSFTa and LSFAl compositions using methods that are industrially up-scalable. The porous support will be made by aqueous based tape casting while the functional membrane layer will be realized by dip coating. To ensure gas-tightness the functional layer needs to be sintered to maximum density and in order to achieve this, fine-sized spray pyrolysis powder will be utilized. For the support layer however the main criteria is high porosity in combination with adequate strength and a lower quality powder like that obtained through conventional solid state reaction can be used to minimize the cost.

The thesis is a continuation of the author's previous project work "Permeability of optimized LSFTa porous supports for syn-gas production membranes" [16] and is also related to the works of M.Sc. students Petter Wibe [17], Nils Wagner [15], Julia Meyer [18], Espen Wefring [19] and Dan S. Lagergren [20]. Studies of the LSFTa and LSFAl materials have previously also been reported by Ph.D. candidate Ørjan Fossmark Lohne [11] and by Dr. Jonas Gurauskis [13, 14].

Chapter 2

Theory

2.1 Processing of the asymmetric membrane

2.1.1 Ceramic powder synthesis

Ceramic oxide powder may be synthesized through various processing methods, e.g. citric acid, solid state reaction, copercipitation or spray pyrolysis. The chosen processing method is known to affect the properties of the powder like the morphology and the particle size and distribution, which later on affect the behavior during sintering and thus the resulting microstructure and density of the end product [21]. In order to achieve a a gas-tight functional layer with maximum density, the powder utilized should ideally be of good quality with a small average particle size and a narrow particle size distribution. Spray pyrolysis is a method of producing oxide powders with these qualities. A water-based precursor containing the reactant cations is fed into a high temperature furnace through a nozzle that atomizes the solution. The droplets that are formed undergo evaporation and solute condensation, followed by drying and thermolysis of the precipitates to form microporous particles [22]. These microporous particles are sintered to form dense particles, which are then usually submitted to further post-treatments like calcination and milling before the powder is ready for use. The spray pyrolysis equipment is illustrated in Figure 2.1. Using this processing method a very fine powder with particles in the sub-micrometer range can be obtained, but this comes with the disadvantage of a high cost.

For the support layer of the asymmetric membrane the main criteria is a high degree of porosity and it is thus possible to use a more affordable powder processing method like solid state reaction. This synthesis method involves simply mixing together stoichiometric amounts of the solid reactants and heating them to a temperature below the melting point until the desired product is obtained [23]. The method is simple and a popular way of producing ceramic materials, but it also has some disadvantages. High temperatures, and thus much energy, is needed in order for the cations to become sufficiently mobile and mix by solid state diffusion. The reactant powders should also be of small particle size and well mixed to minimize the diffusion distance and ensure a homogeneous product. Finally, the produced powder will usually have a large average particle size and a wide particle size distribution, making it difficult to achieve maximum density during sintering [24].

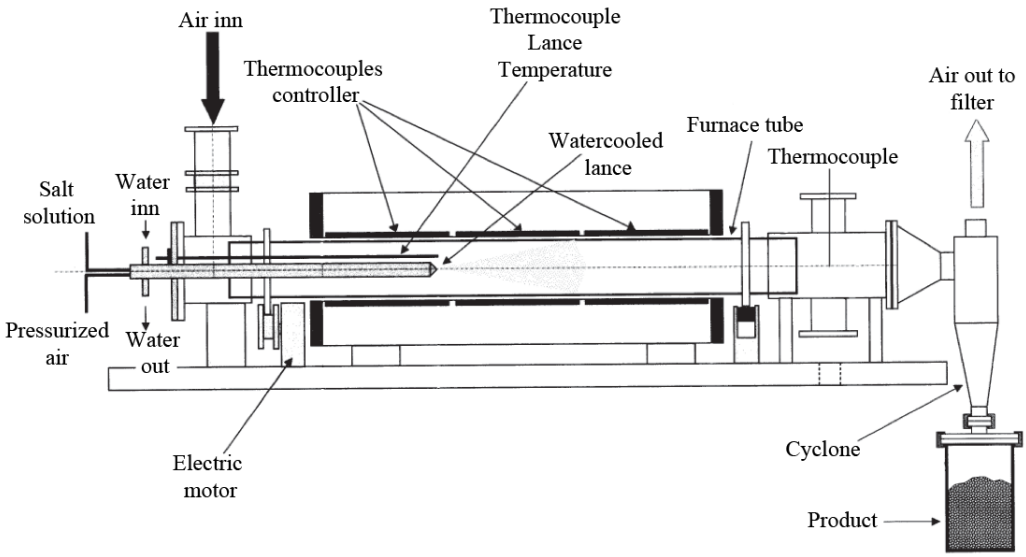

Figure 2.1: Spray pyrolysis process illustrated. Figure from [25]

2.1.2 Tape casting

Tape casting is an efficient way to produce thin sheets of material in large quantities and at low cost. The doctor blade process, illustrated in Figure 2.2, is the most common approach and involves spreading a slip containing the ceramic powder dispersed in a solvent onto a moving carrier film by the blade. In addition to the solvent carrying the particles and a dispersant, the slip is added a binder to provide strength and flexibility to the tape after drying and a plasticizer that softens that binder in the dried state [26]. Wetting agents and de-flocculants may also be added to improve the slip properties. Together with the height of the doctor blade and the speed of the carrier film, the composition and rheology of the slip are important factors for the quality and thickness of the tape [27]. The rheology of a slip can be quantitatively described by the viscosity, η, which for diluted suspension with no particle-particle interactions is given by the Einstein relation [24]:

$$\frac{\eta}{\eta_0} = 1 + 2.5V \tag{1}$$

where η_0 is the viscosity of the suspending liquid and V is the volume fraction of solid particles. In real systems the particle size and distribution, surface chemistry and degree of agglomeration will also affect the viscosity, but the volume fraction will still have a major effect. The viscosity of a tape casting slip should ideally be low enough for the slip to flow onto the carrier film, but also high enough to avoid settling of the particles and additives after casting. A pseudoplastic behavior, in which the viscosity decreases with increasing shear rate, will in this respect be beneficial [27].

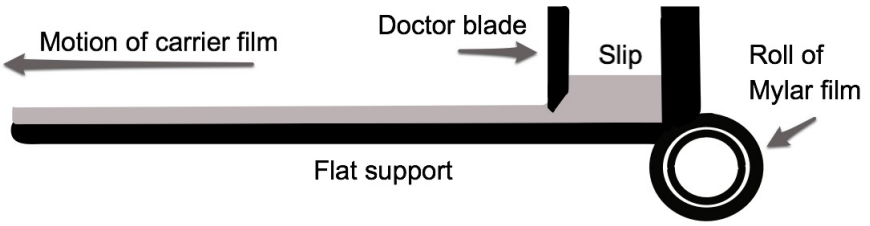

Figure 2.2: The doctor blade tape casting process illustrated. Redrawn from [27]

2.1.3 Dispersants for aqueous based tape casting

Besides the powder characteristics, the choice of dispersant usually has the largest impact on slip rheology. In order to reduce their surface and the system's energy, ceramic particles in a suspension will tend to form flocs [27]. A dispersant is added to avoid this flocculation and is usually introduced in a milling step in order to mechanically break down the agglomerates and ensure complete coverage of the particles [28]. There are essentially two main mechanisms in which the suspensions may be stabilized; electrostatic repulsion and polymeric stabilization. Depending on whether the dispersant attaches to the particle surface or is found free in the suspension, polymeric stabilization can be achieved by steric hinderance or a depletion mechanism. The two situations are illustrated in Figure 2.3, where it is seen that the particles in the suspension in both cases are kept apart by a physical barrier. Poly(vinyl pyrrolidone) (PVP) is an example of a polymeric dispersant and the interactions between PVP and the ceramic powder will determine whether the stabilization is achieved by steric hinderance or the depletion mechanism. An adsorption study of PVP on a range of different surfaces by Esumi et al. suggests that the polymer adsorbs stronger on acidic surfaces like silica and carbon black than basic surfaces like alumina and titania [29, 30, 31]. The heat of adsorption was found to correlate with the IEP of the powder; the higher the IEP, the lower the heat of adsorption. The amount of dispersant needed to stabilize a suspension can be determined by measuring the viscosity; a well dispersed suspension will have a relatively lower viscosity [27].

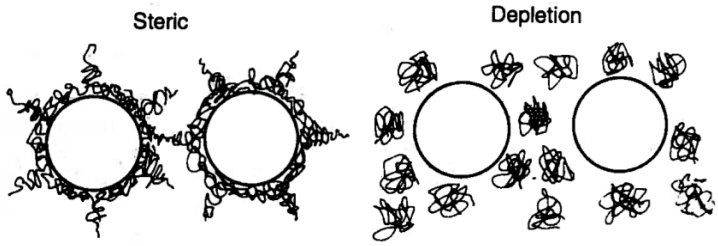

Figure 2.3: Polymeric stabilization mechanisms. Figure from [28]

The basic principle behind electrostatic repulsion is that two particles having the same charge will repel each other. Most ceramic oxides will have a positive or negative surface charge due to adsorbed water hydroxides on the surface that can be ionized [32]:

$$\mathrm{M–O^-} \xleftarrow{\mathrm{OH^-}} \mathrm{MOH} \xrightarrow{\mathrm{H^+}} \mathrm{M\text{-}OH_2^+} \tag{2}$$

where the oxide powder surface is represented by M. An oxide powder particle having a negative surface charge will in water be surrounded by a layer of positively charged hydronium ions (H_3O^+) attempting to neutralize the charge. Outside this, there will be a diffuse layer of negatively charged hydroxyl ions (OH^-). This two-layer structure around the particles is known as the diffuse double layer [24]. Depending on the distance between them, two particles having the same charge will either be repelled electrostatically or attract by van der Waals forces. The net effect of these two forces is combined in the DLVO-theory; the total interaction force will be a function of the distance between two particles as illustrated in Figure 2.4. The charge on the particles, and thus the repulsion between them, is reflected in the height of the primary peak in the DLVO-curve. This is controlled by the pH and ionic concentration of the solvent and by the presence of ions that can be adsorbed on the particle surface [32]. The effective magnitude of the surface charge can be determined indirectly by measuring the particle velocity in an electric field and calculating the zeta potential at the slip plane from [32]:

$$\zeta = \frac{\mathrm{v}\eta}{E\epsilon} \tag{3}$$

where v is the particle velocity [m/s], η is the liquid viscosity [Pas], E it the electric field [N/C] and ϵ is the electric permittivity [F/m]. A large absolute value of the zeta potential indicates a great electrostatic repulsion between the particles and a high degree of dispersion. The zeta potential can therefor be used to determine the effectiveness of a dispersant.

Darvan CN is a polyelectrolyte dispersant that can stabilize a suspension by a combination of electrostatic repulsion and steric hinderance. The dispersant consists of the ammonium salt of poly(methacrylate) (PMA-NH4) with COOH as

the functional group [33]. Like PVP, the effectiveness of Darvan CN as a dispersant depends on the surface chemistry of the oxide powder, i.e. how much Darvan CN that can be adsorbed on the surface. In addition, the effectiveness will depend on the pH of the suspension. When the pH increases, the functional group will dissociate to COO^-:

$$COOH \xrightarrow{OH^-} COO^- + H_2O \tag{4}$$

A study by Cesarano et al. of Na-PMMA dispersant, which is comparable to Darvan CN because of the same functional group, showed that above pH 8.5 the fraction of dissociated functional groups approaches 1 while below pH 3.4 the fraction is close to 0 [34]. As the fraction of dissociated groups on the polymer increases the charge will change from neutral to increasingly negative. Because electrostatic stabilization is achieved by the repulsion of equal charges it follows that the stability also will increase with increasing degree of dissociation.

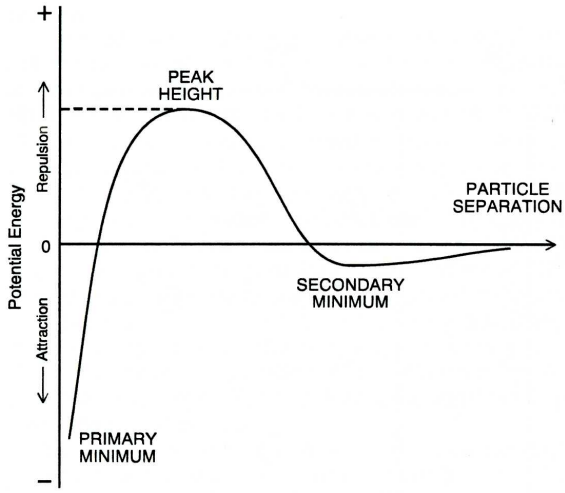

Figure 2.4: The DLVO curve for two charged particles. Figure from [32]

2.1.4 Dip coating

Dip coating is a fast and in-expensive way of depositing thin ceramic films on all kinds of substrates. The method involves simply lowering the substrate in a suspension containing the ceramic particles and withdrawing it at a suitable speed. There are two possible mechanisms in which the substrate may be coated, namely by capillary filtration or film-coating. The two mechanisms and the most important parameters known to affect each of them are summarized in Figure 2.5.

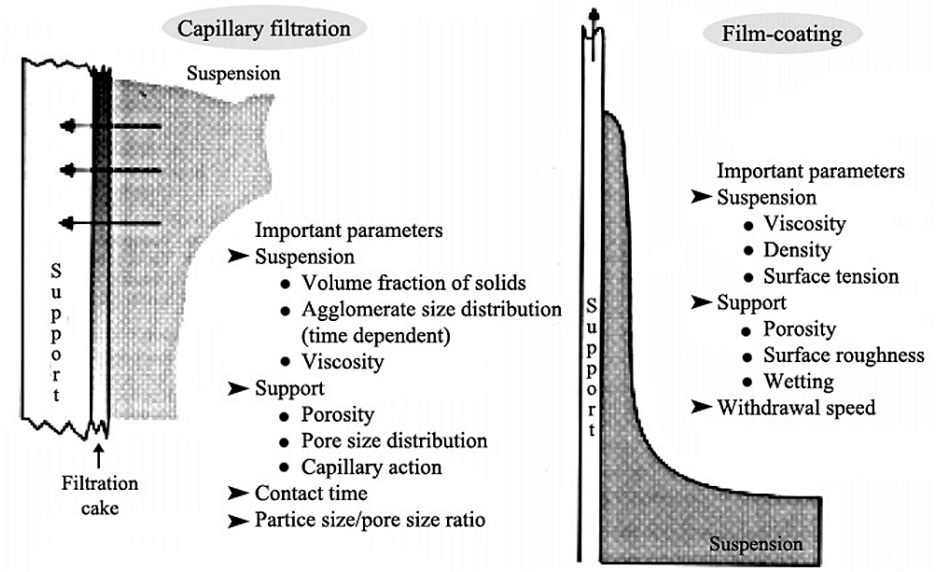

Figure 2.5: Schematic illustration of the two compaction mechanisms that take place during dip coating of porous substrates and the most important parameters affecting them. Figure adapted from [35]

Capillary filtration occurs when the pore surface of a dry substrate is wetted by the liquid of the coating suspension and can be described using the theory of slip casting [36]. The ceramic particles in the dip coating suspension are driven to the interface by capillary suction of the substrate. The radius of the pore channels leading up to the surface will determine the capillary pressure and thus the driving force for the formation of a dense so-called cake layer consisting of

the particles from the dip coating suspension. For a circular pore, the capillary pressure can be estimated from [37]:

$$\Delta p = \frac{2\gamma \times cos\theta}{R} = \frac{2\gamma}{R} \tag{5}$$

where γ is the surface tension of the suspension liquid [N/m], θ is the contact angle between the liquid and the solid interface (set to 0° by assuming complete wetting) and R is the radius of the circular pores [m]. If the surface pores are smaller than the particles, the particles will concentrate at the surface to form the cake layer. The thickness of this layer will depend on the contact time between the substrate and the suspension and will increase with time until the substrate becomes saturated with the dispersing liquid [35]. If however the pore size of the surface is larger than the particles, the pores will need to be clogged before cake formation can take place. This is a disadvantageous situation because the support may become saturated at an early stage, hindering cake formation all together. The thickness of the formed layer is found to be proportional to the square root of the contact time and inversely proportional to the viscosity of the dip coating suspension [38, 39]. In the film-coating mechanism it is the drag force exerted by the substrate during withdrawal from the suspension that leads to the formation of a layer; the thickness of the layer is therefor dependent on the speed of withdrawal. The layer thickness is found to increase with increasing withdrawal speed and increasing viscosity of the dip coating suspension [35]. In practice, both capillary filtration and film-coating will take place during the dip coating process, but capillary filtration will dominate at low solid loadings and slow withdrawal speeds while film coating will dominate at higher solid loadings and faster withdrawal speeds.

2.1.5 Sintering of ceramic materials

Sintering is a thermal treatment process in which ceramic powders are densified by the elimination of porosity. If done properly sintering can provide control of the product's microstructure in terms of grain size, density and distribution of phases and pores [24]. However, because the conditions of sintering depend on the previous processing steps complete control is often difficult to achieve. The results of the final product are dependent on the properties of the powder

like particle shape and size distribution and of the uniformity and efficiency of packing. A reduction of the particle size will increase the sintering rate and allow for a lower temperature to be used, which can be beneficial in preventing decomposition and in reducing the rate of grain growth [40]. The particle size distribution should ideally be narrow to ensure uniform distribution in the green body. Otherwise there is a risk of the particles moving during the densification process, resulting in even larger pores than originally present in the green body [41]. Agglomerates in the powder should be avoided as they will cause non-uniformity and difficulties with obtaining full densification [24]. In cases where a high degree of porosity is desired, pore formers that are burned out during the heat-treatment may be introduced in the green body to give better control of the porosity [42].

2.2 Strength of ceramic materials

The strength of a material is a measure of how well the material withstands stress. The measured strength will depend on the mode of loading, the specimen geometry and the presence of cracks, flaws and pores in the specimen tested [24]. This is especially an important consideration for ceramic materials, which in general are difficult to fabricate completely dense and flaw-free. Under an applied stress, the material failure will take place at the weakest points, which means that the measured strength of a specimen containing a flaw in general will be lower than for a flaw-free specimen. Because of this, strength data for ceramic materials should be reported as a statistical probability for failure instead of single strength values. One of the most common ways to accommodate this is by reporting strength data for ceramic materials together with a Weibull distribution for the probability of failure, F [43]:

$$F = 1 - exp\Big[- V\Big(\frac{\sigma - \sigma_U}{\sigma_0}\Big)^m\Big] \tag{6}$$

where V is the volume of material under tension, σ is the applied stress [MPa], σ_U is the minimum stress below which the probability of failure is zero (often set to 0), σ_0 is a normalizing parameter (taken as the stress at which the probability

for failure is 63.2 %) [MPa] and m is the Weibull modulus (dimensionless). The Weibull modulus describes how uniformly the defects in the material are distributed and is a measure of material reliability. Usually, 20–30 test samples are required to determine an accurate value for the Weibull modulus [24]. Some recently reported fracture strength values of porous ceramic materials intended for the application as supports for oxygen permeable membranes are presented in Table 2.1. An extensive review of the fracture strength for dense perovskite materials may be found in Ref. [44].

Table 2.1: Characteristic fracture strength for porous ceramic materials intended for the application as supports for oxygen permeable membranes. Measured at room temperature.

Material	Strength [MPa]	Weibull modulus	Porosity %	Loading	Ref
$La_{0.8}Sr_{0.2}CoO_3$	76	–	10-13	4-point	[45]
$Ba_{0.5}Sr_{0.5}Co_{0.8}Fe_{0.2}O_{3-\delta}$	38	4	38	biaxial	[46]
$Ba_{0.5}Sr_{0.5}Co_{0.8}Fe_{0.2}O_{3-\delta}$	31±1	8.4	34	biaxial	[47]
$La_{0.6}Sr_{0.4}Co_{0.2}Fe_{0.8}O_{3-\delta}$	18±2	3.8	46	biaxial	[47]
$Ce_{0.9}Gd_{0.1}O_{1.95-\delta}$	55±3	4.0	43	biaxial	[47]

2.2.1 Strength characterization by the ball-on-ring method

Common testing methods for measuring strength include tensile, compressive and bend testing, all of which involve loading in a single direction and thus producing uniaxial stress fields [24]. In the case of ceramic membranes however, biaxial stress loading is considered to better reflect the service conditions, like thermal cycling [48]. Furthermore, biaxial stress testing has the advantage of not failing due to edge cracks introduced during specimen preparation, as may be a problem with the 3- and 4-point bending tests. The ball-on-ring test, illustrated in Figure 2.6 can be used to find the biaxial strength of thin disc specimens like the asymmetric membrane. A ball is used to exert a pressure force on a disc until it fractures and the load at fracture is used to calculate the maximum tensile stress from [49]:

$$\sigma_{max} = \frac{3P(1+\nu)}{4\pi t^2}\left[1 + 2ln\left(\frac{a}{b}\right) + \frac{1-\nu}{1+\nu}\left(1 - \frac{b^2}{2a^2}\right)\frac{a^2}{r^2}\right] \quad (7)$$

where P is the load[N]; ν is Poisson's ratio; t is the specimen thickness[mm]; a is the radius of the specimen support[mm]; b is the radius of uniform loading, approximated to t/3 [mm] and r is the specimen radius[mm].

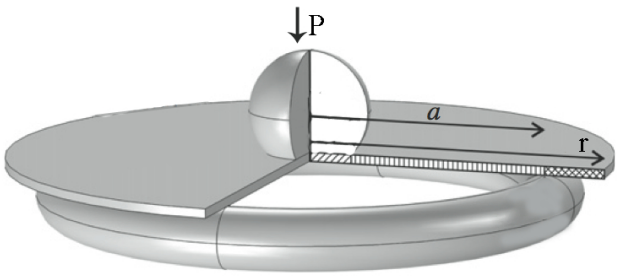

Figure 2.6: Loading configuration of the ball-on-ring strength test. Note that the ball is really spherical. Figure from [50]

2.3 Overview of relevant previous work

Asymmetric membranes of the LSFTa and LSFAl compositions have previously been prepared by uniaxial pressing of the porous supports and dip coating the dense functional layers on top [15, 13]. In both cases, fine-sized spray pyrolysis powder was used for both the support and membrane layers. The processing route followed was approximately the same and is summarized in Figure 2.7. This resulted in supports with 30–45 % open porosity and a 15–20 μm dense, functional layer. The measured oxygen permeation fluxes of the prepared asymmetric membranes are presented in Table 2.2.

Tape casting of LSFTa porous support using coarser solid state reaction powder has previously been reported by Wibe [17]. However, the slip additives used in that work were mainly based on commercial formulations of which the exact

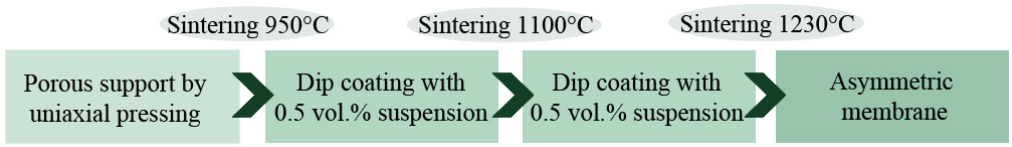

Figure 2.7: Previous processing of LSFTa and LSFAl asymmetric membranes.

Table 2.2: Oxygen flux of LSFTa/LSFAl oxygen permeable membranes reported in literature. S = membrane with surface modifications.Thickness refers to the thickness of the dense, functional layer.

Material	Flux, J_{O_2} $[ml/(min * cm^2)]$	Ea [kJ/mol]	T [°C]	Thickness [μm]	P_{O_2} [atm]	Ref.
LSFTa2882	5.8	52	1000	20	0.006	[14]
	8.7 (S)	–	1000	20	0.01	[14]
LSFAl2882	15.3	94.4	1000	15-20	0.020	[15]

compositions are unknown. In previous work by the author, tape casting of LSFTa porous supports using more common slip additives like PVA/PEG was investigated [16]. The work was unsuccessful in producing a tape which was flexible and defect-free and because of this it was suggested that PVP is an unsuited dispersant for the powder. LSFAl porous supports have been made by Lagergren by tape casting and using solid state reaction powder without any reported difficulties [20] . However the attempt to dip coat these supports did not result in an airtight membrane layer. Lagergren also reported about difficulties with obtaining phase pure LSFAl powder through solid state synthesis.

Chapter 3

Experimental

3.1 Chemicals and equipment

The list of chemicals used for powder synthesis is given in Table 3.1 and the list of chemicals used for green forming, together with their function, is given in Table 3.2. The list of equipment used, with the model and application specified, is given in Table 3.3.

Table 3.1: List of chemicals used for powder synthesis

Chemical compound	Molecular Formula	Purity/conc.	Supplier
Strontium Carbonate	$SrCO_3$	> 98 %	Fluka Chemika
Lanthanum Oxide	La_2O_3	99%	Aldrich
Tantalum Oxide	Ta_2O_5	99%	Alfa Aesar GmbH
Iron Oxide	Fe_2O_3	99%	Alfa Aesar GmbH
Ethanol	CH_3CH_2OH	96 vol.%	Sigma Aldrich
Aluminum oxide	Al_2O_3	99.98 %	Alfa Aesar GmbH
Tantalum oxalate	$Ta_2C_{10}O_{20}$	> 99 %	H.C. Starck, Goslar
Citric acid	$C_6H_8O_7 \times H_2O$	> 99.5 %	Sigma Aldrich
Hydrogen peroxide	H_2O_2	30 wt.%	Merck
Lanthanum nitrate	$La(NO_3)_3)$	> 99 %	Fluka Chemika
Ethylenediaminetetraacetic acid	$H_4 \times EDTA$	99 %	Acros Organics
Iron nitrate	$Fe(NO_3)_3$	> 99 %	Fluka Chemika
Ammonium Hydroxide	NH_4OH	25 %	Merck
Nitric acid	HNO_3	65 %	Merck
Strontium Nitrate	$Sr(NO_3)_2$	99 %	Merck

Table 3.2: List of chemicals used for green forming and their function

Chemical compund	Abbreviation	Molecular weight	Function	Supplier
Poly(vinylpyrrolidone)	PVP	40000	Dispersant	Alfa Aesar
Darvan CN[1]	Darvan CN	10-16000	Dispersant	R.T Vanderbilt
Carbon Black	CB	12.01	Pore former	Merck
Poly(ethylene glycol)	PEG	400	Plasticizer	Merck
Poly(vinyl alcohol)	PVA	n=2000	Binder	Tokyo Chemical Industry
BYK3455	–	–	Wetting agent	BYK-chemie GmbH
Distilled water	H_2O	18	Solvent	–
Dodacol-D1003	Dodacol D	–	Dispersant	Zschimmer & Schwarz

1: Darvan CN is provided by the manufacturer as a 25 wt.% solution in water

Table 3.3: List of equipment used

Type	Manufacturer and model	Application
Furnace	Labstar 1200, Entech	Calcination of powders
Furnace	Entech	Sintering
XRD	Bruker AXS D8 Focus	Phase composition
SEM	Hitachi S-34000N LVSEM	Powder morphology and membrane structure
SEM	Zeiss Ultra55 FESEM	Powder morphology and membrane structure
EDS	Oxford Instruments X-max	Energy dispersive X-ray spectroscopy
BET	Micromeritics Tristar 3000	Surface area
DIL	NETSCH DIL 402C	Dilatometry analysis
Mastersizer	Malvern Mastersizer 2000	Particle size and distribution
Zetasizer	Malvern Zetasizer Nano ZS	Zeta potential and isoelectric point
Rheometer	Haake MARS III	Viscosity measurements
Rotary Evaporator	Buchi Rotavapour	Solvent evaporation
Ball-on-ring	Instron 5543	Fracture strength
Permeability	In-house constructed	Permeability measurements
Ultrasonic probe	Branson Digital Sonifier	Dispersing suspensions
Gas chromatography	Varian Micro-GC CP4900	Gas composition

3.2 Procedure

3.2.1 Powder synthesis

Solid state reaction

The same procedure was followed in making both $La_{0.2}Sr_{0.8}Fe_{0.8}Ta_{0.2}O_{3-\delta}$ (LSFTa) and $La_{0.2}Sr_{0.8}Fe_{0.8}Al_{0.2}O_{3-\delta}$ (LSFAl) powder. The starting oxides, La_2O_3, Fe_2O_3 and Ta_2O_5/Al_2O_3, were calcined in alumina crucibles for 12 hours at 800°C to remove any adsorbed volatile species (heating/cooling rate: 200°C/hour). The oxides were taken out of the furnace at 250°C and mixed with $SrCO_3$. The amount of $SrCO_3$ and each oxide used for the synthesis of LSFTa and LSFAl is given in Table 3.4. The precursor powders were mixed by ball milling together with ethanol for 24 hours at 120 rpm. Polyethylene (PE) bottles (500 ml) and Yttrium Stabilized Zirconia (YSZ, ϕ=5 mm) milling media were used. After milling, the ethanol was removed by evaporation in a rotavapor. The powder mixture was calcined at 1300°C for 12 hours in alumina crucibles with a heating and cooling rate of 200°C/hour. The resulting powder was crushed with a mortar and pestle and ball milled in ethanol at 130 rpm for 24 hours (PE-bottle, 250 ml; YSZ-balls, ϕ=5 mm).

Table 3.4: Amounts of chemicals used for solid state synthesis of LSFTa and LSFAl

Chemical	Amount [g]	Amount of cation [mol]	Cation fraction
Starting powders for LSFTa-SSR			
La_2O_3	16.7491	0.0514	0.1
Fe_2O_3	32.8340	0.2056	0.4
Ta_2O_5	22.7163	0.0514	0.1
$SrCO_3$	60.7125	0.4112	0.4
Starting powders for LSFAl-SSR			
La_2O_3	13.3027	0.0408	0.1
Fe_2O_3	26.0805	0.1633	0.4
Al_2O_3	4.1631	0.0408	0.1
$SrCO_3$	48.2196	0.3266	0.4

Spray pyrolysis
The LSFAl spray pyrolysis powder (LSFAl-SP) was supplied by Cerpotech AS [25] and had been calcined at 1000°C for 12 hours. The received powder was sieved (250 μm sieve) and ball milled in ethanol for 24 hours (250 ml PE-bottle, 5mm YSZ-milling media). To investigate the purity of the as-received powder a pellet (ϕ=15 mm) was made by uniaxial pressing at 40 MPa for 2 minutes. The pellet was sintered at 1300°C for 2 hours with a heating and cooling rate of 60°C/hour.

The LSFTa spray pyrolysis powder (LSFTa-SP) was made based on the procedure described by Mokkelbost et al. [51]. The preparation of the cation precursor solutions is described in the following and the amounts of the different chemicals used are given in Table 3.5. Flowcharts showing the procedure step-by-step may be found in Appendix A.

- La-EDTA and Fe-EDTA complexes were prepared by dissolving lanthanum nitrate, $La(NO_3)_3$ or iron nitrate, $Fe(NO_3)_3$, in distilled water and adding ethylenediaminetetraacetic acid, $H_4 \times EDTA$. Ammonia, NH_3 (25 %), was added until pH reached 11 and the solution was mixed for 12 hours to form the water soluble La-EDTA/Fe-EDTA complex. The pH was adjusted to slightly above 7 by adding HNO_3 (65 %) before it was filtered. Finally, it was diluted to 5 l by adding distilled water.
- Ta-oxalcitrate solution was prepared by dissolving citric acid monohydrate, $C_6H_8O_7 \times H_2O$, in hydrogen peroxide, H_2O_2, and then slowly adding Ta-oxalate solution while stirring. The solution was heated to 60°C with a heating rate of approximately 0.5°C/min in order to start the exothermic decomposition of oxalate ions. The temperature was kept between 60°C and 70°C by alternately heating the solution and cooling it on ice. This was done for 8 hours, until the gas development stopped, indicating that all of the excess oxalate had reacted. The pH was adjusted to slightly above 7 by adding NH_3. The solution was again heated to 60°C, this time to remove excess H_2O_2. Finally, the solution was filtered and diluted to 5 l by adding distilled water.

The precursor solutions were standardized thermogravimetrically before mixing with dried $Sr(NO_3)_2$ (200°C, 12 h) in stoichiometric amounts to make

$La_{0.2}Sr_{0.8}Fe_{0.8}Ta_{0.2}O_{3-\delta}$. Details about the standardization may be found in Appendix B. The molar amounts together with the concentrations of the solutions calculated from the standardization are given in Table 3.6. This solution was spray pyrolysed using pilot scale equipment by atomizing the solution through a two-phase nozzle at a rate of 10 L/h and into a rotating furnace at a temperature of 1000°C. An illustration of the spray pyrolysis equipment used was shown in Figure 2.1. The as-prepared powder was ball milled dry with YSZ-balls in order to reduce the tap density. The milled powder was calcined at 900°C for 12 hours in air with a heating and cooling rate of 200°/hour to burn away the remaining nitrates. This calcination temperature was selected based on TGA analysis of the raw-powder (given in Appendix C). Finally, the calcined powder was ball-milled for 24 hours in ethanol (250 ml PE-bottles, 5 mm YSZ-milling media).

Table 3.5: Amount of different chemicals used making spray pyrolysis precursors

Precursor	Chemical	Amount added	Amount [mol]
Tantalum oxalcitrate complex solution	Tantalum oxalate	0.517 l	0.454
	Citric acid	286.3 g	1.362
	H_2O_2 (35 wt.%)	1.63 l	–
La-EDTA complex solution	$La(NO_3)_3 \times 6H_2O$	346.4 g	0.8
	$H_4 \times EDTA$	233.8 g	0.8
Fe-EDTA complex solution	$Fe(NO_3)_3$	646.4 g	1.6
	$H_4 \times EDTA$	467.6 g	1.6

Table 3.6: Amounts of precursor solutions used making the solution for spray pyrolysis

Chemical	Amount [mol]	Solution concentration [g/mol]	Cation fraction
Fe-EDTA	1.4826	2.8511×10^{-4}	0.4
La-EDTA	0.3706	1.5015×10^{-4}	0.1
Ta-oxalate	0.3706	1.3405×10^{-4}	0.1
Strontium Nitrate	1.4826	–	0.4

3.2.2 Asymmetric membrane production

LSFTa porous supports by tape casting

Zeta potential measurement

To find the amount of Darvan CN needed to make a stable LSFTa dispersion, a measurement of the zeta potential as a function of pH and Darvan CN content was performed. The stability of LSFTa at different pH values was first examined by dispersing a small amount of LSFTa solid state reaction powder ($\sim$ 0.4 g) in two containers of distilled water ($\sim$ 5g) and adjusting the pH to 4.5 and 7.8 by adding HCl. A third sample of pure LSFTa powder in water was also prepared. The three mixtures were left slow rolling at approximately 30 rpm for 48 hours before the pH was measured again. The liquid was decanted and the powders were examined by XRD.

The test mixtures for the zeta potential measurement were made by mixing LSFTa-SS powder with distilled water ($\sim$ 0.05 vol.% solid loading) and adding various quantities of Darvan CN; the compositions of the 5 different test mixtures are given in Table 3.7. Darvan CN was diluted 1/100 in distilled water to have better control of the addition. The mixtures were dispersed using an ultrasonic probe 2 times for 3 minutes at 20 % amplitude before they were left slow rolling for 48 hours for further stabilization. Right before performing the measurements, the mixtures were dispersed again in an ultrasonic bath for 10 minutes. The zeta potential measurements were preformed using dynamic light scattering technique (Malvern Zetasizer Nano ZS). Standard disposable cells were filled with the test solutions and 3 runs were performed for each composition and pH. The pH was adjusted from 5–10 in steps of 1 by an automatic titrator using HCl (0.25 M) and NaOH (0.25 M).

Table 3.7: Composition of test suspensions for zeta potential measurements

LSFTa-SS [g]	H_2O (milliQ) [g]	Darvan CN [g] (1/100 dilution)	Darvan CN [wt.% of LSFTa]
0.1147	40.4260	–	0
0.1274	40.6343	0.0261	0.205
0.1257	40.0932	0.0569	0.474
0.1249	40.3003	0.0848	0.679
0.1353	40.3235	0.1126	0.832

Viscosity measurements

Rheological characterization of concentrated suspensions was preformed in order to further investigate the optimum amount of Darvan CN needed to disperse LSFTa. Suspensions containing 15 vol.% LSFTa-SS powder in distilled water and various amounts of Darvan CN were prepared, the compositions are given in Table 3.8. Each of the suspensions were ball milled for 24 hours at 150 rpm (PE-bottles, 100 ml; YSZ-balls, ϕ = 10 mm). Rheological measurements were performed with a rotational rheometer equipped with a double gap cup test geometry. The flow curves were recorded using controlled shear rate mode up to 500 s^{-1} and a dwell time of 30 seconds at maximum shear before the reverse sweep. The temperature was held constant at 23°C. The particle size and distribution of the suspensions was measured by laser diffraction.

Table 3.8: Composition of test suspensions for rheological measurements

LSFTa-SS [g]	H_2O (dist.) [g]	Darvan CN [g] (1/10 dilution)	Darvan CN [vol.% of LSFTa]
4.9984	4.501	–	0
5.0016	4.312	0.2007	0.4
5.0188	4.257	0.2715	0.5
4.9962	4.196	0.3028	0.6
5.0049	4.140	0.3598	0.7

Tape casting and lamination

Based on the zeta potential and rheology measurements two tape casting slips were made with the compositions given in Table 3.9. The procedure for mixing the slips and casting the tapes is shown in Figure 3.1. The PVA used was first dissolved in water to a 15 wt.% dilution. This was done by gradually adding PVA-powder to distilled water heated to 70°C while stirring. The mixture was stirred for an additional 2 hours for homogenization before it was left for two days in room temperature in order for the formed bubbles to settle. The rheology of the prepared slips was characterized using a double cone and plate geometry with an angle of 1°on a rotational rheometer. Flow curves were recorded using controlled shear rate mode up to 500 s^{-1} and a dwell time of 30 seconds at maximum shear before the reverse sweep. The temperature was held constant at 23°C.

The produced tapes were punched out with a 30 mm steel cylinder and laminated in order to achieve the desired thickness (15 layers of tape to give $\sim$1.0 mm laminate) for the porous support. A small amount of water was dispersed in-between the layers of the green tape discs with an air brusher and the discs were stacked top surface to bottom surface in case there was some segregation of powder or binder in the green tape. Mylar film was used on top and bottom of the stack to avoid sticking and the stack was pressed at 70°C for 5 minutes using a pressure of 0.2 MPa. The laminated stack was punched out with a 28 mm steel cylinder to remove uneven edges and heat-treated according to the temperature program shown in Figure 3.2. The intermediate hold-temperatures of 200°C, 320°C, and 480°C were used to give controlled burn-off of the organic additives and pore former added to the slip and are based on thermogravimetric analysis of the green tape in previous work [16]. The sintering temperatures, $\mathrm{T_C}$, tried out were 1150°C and 1190°C (holding time of 2 hours at maximum temperature in both cases).

Table 3.9: Composition of LSFTa tape casting slips prepared together with the relative amount of the components. The Darvan CN and PVP were added as 10 wt.% water dilutions, PVA was added as a 15 wt.% water dilution. The relative amounts stated below are the pure amounts of the chemicals.

Component	Amount [g]	Relative amount	Function
Tape 1 – 16.7 vol.% powder loading			
LSFTa-SS-powder	11.587	–	Oxide powder
Darvan CN	0.708	0.6 wt.% of LSFTa	Dispersant for LSFTa
Distilled water	9.149	83.3 vol. % of LSFTa	Solvent
Carbon Black (CB)	2.680	40 vol.% of LSFTa	Pore former
PVP	0.546	2 wt.% of CB	Dispersant for CB
PVA	17,158	18 wt.% of LSFAl+CB	Binder
PEG	2,368	92 wt.% of PVA	Plasticizer
BYK3455	0,304	0.5 wt.% of total slip	Wetting agent
Tape 2 – 15.8 vol.% powder loading			
LSFTa-SS-powder	28.522	–	Oxide powder
Darvan CN	1.730	0.6 wt.% of LSFTa	Dispersant for LSFTa
Distilled water	24.148	84.2 vol. % of LSFTa	Solvent
Carbon Black (CB)	6.642	40 vol.% of LSFTa	Pore former
PVP	1.328	2 wt.% of CB	Dispersant for CB
PVA	42.405	18 wt.% of LSFAl+CB	Binder
PEG	5.808	91 wt.% of PVA	Plasticizer
BYK3455	1.010	0.9 wt.% of total slip	Wetting agent

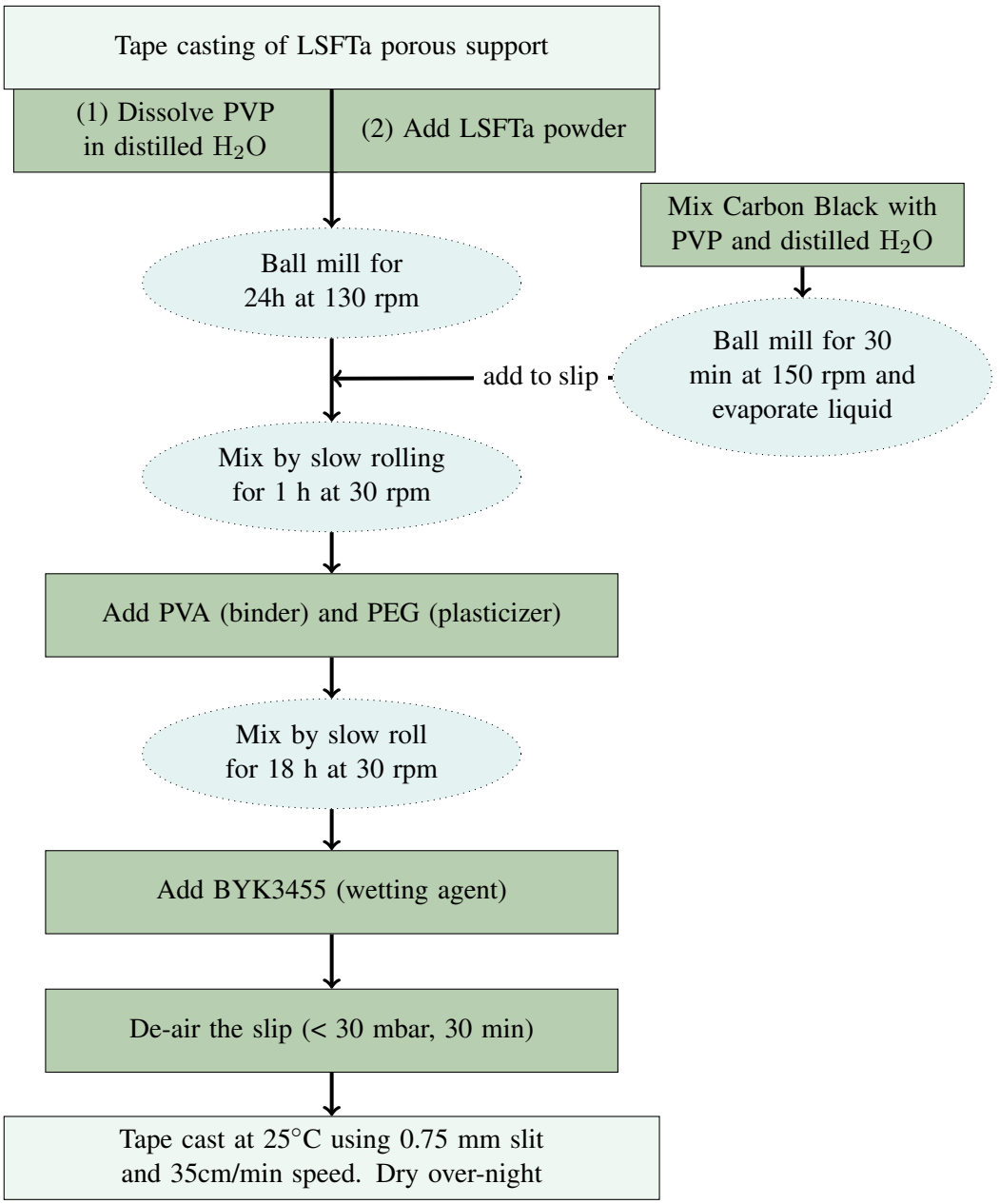

Figure 3.1: Flowchart for tape casting of the LSFTa porous support

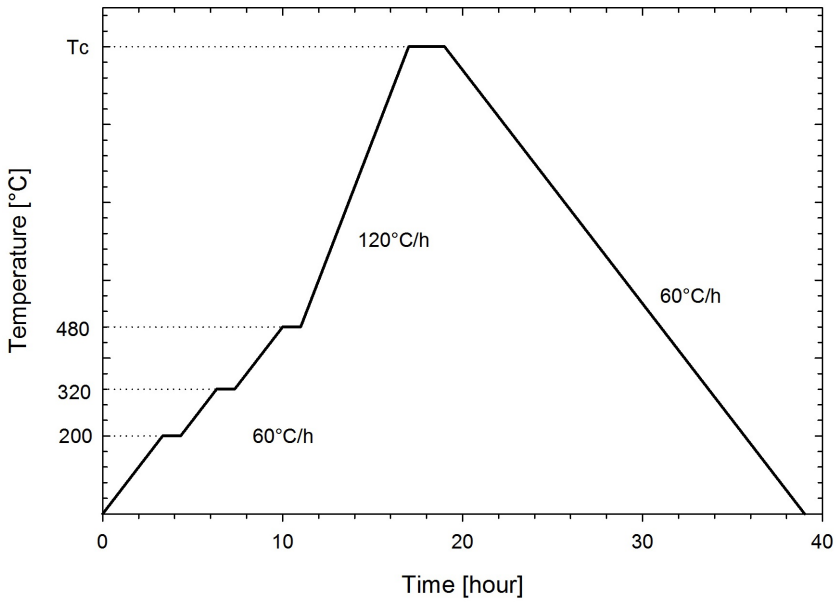

Figure 3.2: Heat treatment program for binder burn out and pre-sintering of LSFTa and LSFAl green tapes. The holding time at the intermediate temperatures 200°C, 320°C and 480°C is 1 hour, the holding time at the maximum temperature, T_C, is 2 hours.

LSFAl porous supports by tape casting

The step–by–step procedure for making the LSFAl porous support by tape casting is shown in Figure 3.3 and is based on the work by Lagergren [20]. A tape using the same procedure as for making the LSFTa tape casting slip was also tried out. The amounts of the different chemicals used are given in Table 3.10. The amount of PVP for dispersing LSFAl-SS in the slip was adjusted according to the measured particle surface area of the solid state synthesized powder. After tape casting the tapes were punched out and laminated as described previously for LSFTa tapes. The laminated stacks were heat treated according to Figure 3.2 with the sintering temperatures, T_C, being 1150°C, 1200°C, 1250°C and 1300°C.

Table 3.10: Composition of the prepared LSFAl tape casting slip. PVP was added as a 10 wt.% water dilution, PVA was added as a 15 wt.% water dilution.

Component	Amount [g]	Relative amount	Function
Tape 1 - following procedure in Figure 3.3			
Carbon Black (CB)	5.675	39 vol.% of LSFAl	Pore former
PVP	1.177	2 wt.% of CB	Dispersant for CB
Distilled water	22.514	85 vol. % of LSFAl	Solvent
LSFAl-SS-powder	22.109	–	Powder
PVP	2.437	1,1 wt.% of LSFAl	Dispersant for LSFAl
PVA	27.842	15 wt.% of LSFAl+CB	Binder
PEG	3.771	90 wt.% of PVA	Plasticizer
BYK3455	0.703	0.8 wt.% of total slip	Wetting agent
Tape 2 - following procedure in Figure 3.1			
LSFAl-SS-powder	28.200	–	Powder
PVP	2.999	1,1 wt.% of LSFAl	Dispersant for LSFAl
Distilled water	28.735	85 vol. % of LSFAl	Solvent
Carbon Black (CB)	7.475	40 vol.% of LSFAl	Pore former
PVP	1.594	2 wt.% of CB	Dispersant for CB
PVA	35.670	15 wt.% of LSFAl+CB	Binder
PEG	4.815	90 wt.% of PVA	Plasticizer
BYK3455	0.851	0.8 wt.% of total slip	Wetting agent

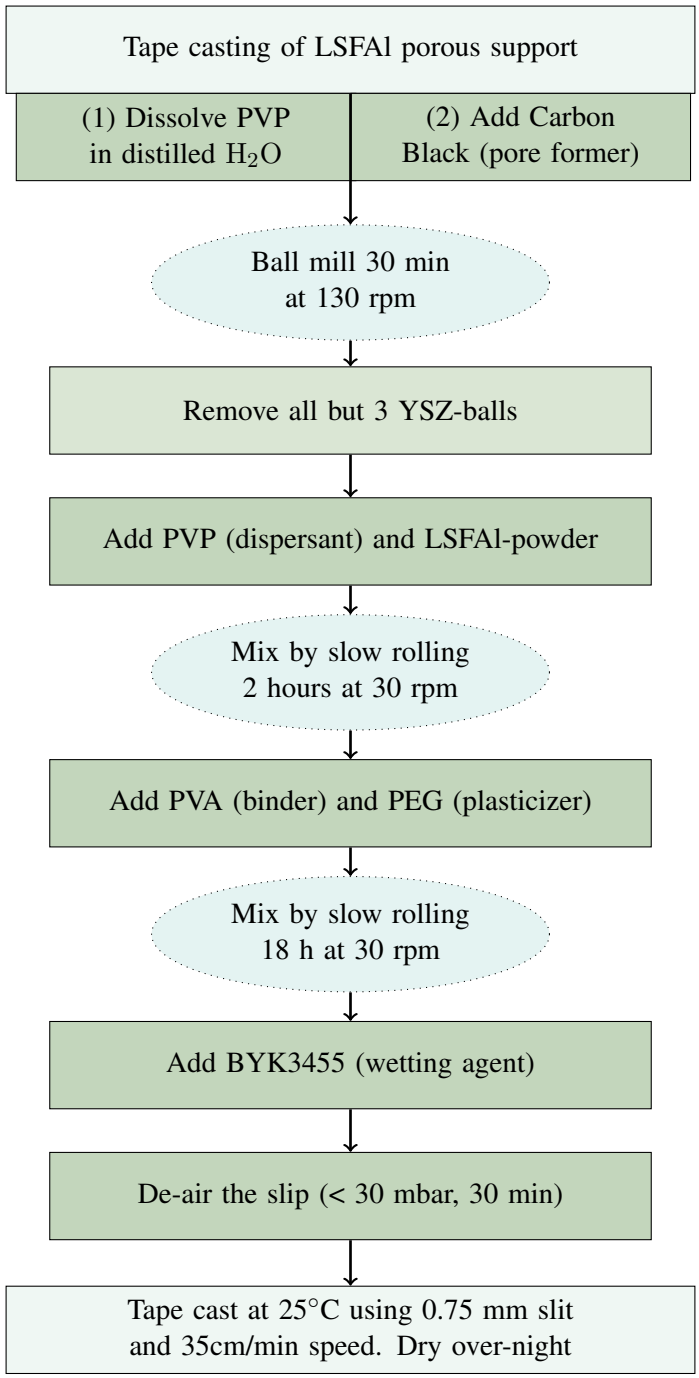

Figure 3.3: Flowchart for tape casting the LSFAl porous support

Dip coating of dense functional layer

LSFTa and LSFAl dip coating suspensions were prepared based on the compositions given by Gurauskis et al. [13] and Wagner [15]. Both suspensions were made by ball milling a 2 vol. % mixture of the oxide powder with ethanol and Dodacol-D (dispersant) for 24 hours (250 ml PE-bottle, 5 mm YSZ-balls) and subsequently diluting the suspension to 0.5 vol.% or 0.75 vol.%. The composition of the suspensions is given in Table 3.11. An ultrasonic probe was used to disperse the suspensions 2 times 3 minutes at 20% amplitude prior to coating and the suspensions were left slow rolling at 30 rpm in between use. The particle size of the suspensions was measured both right after preparation and prior to dip coating. Pre-sintered supports were attached to a glass plate using liquid latex in order to ensure deposition on only one side. The supports were dipped several times and sintered in-between the dips at various temperatures, Table 3.12 gives an overview of all the procedures that were tried out. In all of the heat-treatments a heating rate of 120°C/hour and a cooling rate of 60°C/hour was used. The dip coating was performed manually, so the withdrawal speeds from the suspension are only approximate. One of the supports pre-sintered at 1300°C was polished with Si-C paper (# 800) prior to dip coating. This specimen is specified as 1300-P in Table 3.12.

Table 3.11: Composition of LSFAl and LSFTa suspensions for dip coating of dense, functional layer

Component	Amount [g]	Comment
For the LSFTa dip coating suspension		
LSFTa-SP	2.500	Spray pyrolysis powder
Ethanol	14.849	Solvent, to make 2 vol.% suspension
Dodacol-D	0.741	Dispersant, 2.50 wt.% of LSFTa
Ethanol	47.40	To dilute suspension to 0.5 vol.%
For the LSFAl dip coating suspension		
LSFAl-SP	2.5 00	Spray pyrolysis powder
Ethanol	17.003	Solvent, to make 2 vol.% suspension
Dodacol-D	0.5 0	Dispersant, 2.25 wt.% of LSFAl
Ethanol	53.90	To dilute suspension to 0.5 vol.%
Ethanol	30.00	To dilute suspension to 0.75 vol.%

Table 3.12: Specifications for dip coating of the porous supports. Drying time in between multiple dips was 15 minutes. CT = pre-sintering temperature of support, ST = sintering temperature after dip coating. The holding time at maximum temperature was 2 hours in all cases. f = fast withdrawal from the suspension, s = slow withdrawal from the suspension.

Sample ID	CT	1st dip	ST	2nd dip	ST	3rd and 4th dip	ST
LSFAl dip coated with 0.5vol.% suspension							
LSFAl - 1	1200	2x5s (s)	1230	1x5s (s), 1x5s (f)	1300		
LSFAl - 2	1250	2x5s (s)	1250	1x5s (s), 1x5s (f)	1300	1x5s (s), 1x5s (f)	1300
LSFAl - 3	1300	2x5s (s)	1300	1x5s (s), 1x5s (f)	1300		
LSFAl - 4	1300-P	2x5s (s)	1300	1x5s (s), 1x5s (f)	1300		
LSFAl dip coated with 0.75vol.% suspension							
LSFAl - 5	1250	2x5s (s)	1250	1x5s (s), 1x5s (f)	1300		
LSFTa dip coated with 0.5vol.% suspension							
LSFTa - 1	1190	2x5s (s)	1230	1x5s (s), 1x5s (f)	1230		

3.2.3 Powder characterization

The phase purity of the powders was checked with X-ray diffraction (XRD) using $\mathrm{Cu} - \mathrm{K}_\alpha$-radiation (Bruker AXS D8 Focus). The patterns were recorded in the range of $10° \leq \theta \leq 60°$ using step size $0.01°$ and a collection time of 2.0 s. Scanning electron microscopy (Hiatchi S3400N LVSEM and Zeiss Ultra55 FE-SEM) was used to investigate the powder morphology. A small amount of powder was attached to carbon tape and an acceleration voltage of 10 kV was used. The particle size and distribution was measured by laser diffraction (Malvern Mastersizer 2000). A refractive index of 2.42 was chosen and the powder was dispersed in distilled water. Ultrasonic displacement was turned on 20 seconds prior to making the measurements in order to break down the soft agglomerates. Three measurement rounds were performed for each sample and the average of these was calculated by the software. The average surface area of the powder was found by BET-analysis of nitrogen adsorption (Micromeritics Tristar 2000). Small amounts ($\sim$ 0.5 – 2 g) of the powder were dried for 24 hours (250°C, 40 mbar) before the analysis was carried out. For the dilatometry analysis a small amount of powder was fed into a ϕ= 5 mm double sided pressing dye and pressed at $\sim$ 0.1 MPa for 2 minutes. The length of the resulting pellets varied between 5–8 mm. The DIL analysis was carried out in synthetic air with a flow rate of 1 ml/min (NETSCH DIL 402C). The heating and cooling rate used was 2K/min and the samples were all heated up to 1500°C.

3.2.4 Asymmetric membrane characterization

Porosity

The porosity of the membrane supports was quantified using Archimedes method. The test was performed in accordance with ISO 5017:1998. Dry test pieces of the membrane support were weight and placed in a vacuum chamber. The chamber was evacuated until a pressure of < 20 mbar was attained and this pressure was maintained for 20 minutes. Isopropanol was introduced slowly into the chamber to cover the test pieces. The reduced pressure was maintained for another 20 minutes to allow the liquid to penetrate the pores before the the chamber was aerated. The test pieces were left in isopropanol for 30 minutes in order for the temperature to stabilize. The temperature of isopropanol was measured and

the test pieces were weight while still immersed by the liquid. Finally, the test pieces were removed from the liquid and sponged with damp paper to remove the surface film of liquid before they were weight one final time.

Strength testing of LSFAl porous support
The fracture strength of LSFAl porous supports was investigated by the ball-on-ring test using the Instron 5543 apparatus. All of the tested supports were sintered at 1300°C for 2 hours following the heat-treatment program given in Figure 3.2. The fracture surfaces were examined after the experiment using SEM.

Phase purity
The top surface of the LSFAl asymmetric membrane was characterized by X-ray diffraction. The patterns were recorded in the range of $10^\circ \leq \theta \leq 60^\circ$ using a step size of 0.01° and a collection time of 2.0 s. The chemical composition of the top surface was analyzed using EDS.

Oxygen flux measurements
The LSFAl asymmetric membrane made from the support calcined at 1250°C (LSFAl-2 in Table 3.12) was chosen for oxygen flux investigations.The experimental set-up for measurements has been established by Gurauskis et al. [13]. The asymmetric membrane was placed between two gold rings and mounted inside an alumina housing (Ø16.2 mm). This arrangement was placed inside the furnace with the dense functional side of the asymmetric membrane facing up towards the secondary (He) side. The furnace was heated up in a rate of 30°C/h to the softening temperature of gold, 1055°C, and a load was put on top of the furnace to press the gold rings tightly around the membrane. The system was checked for leakages by applying helium on the secondary side (200 ml/min) and air on the primary side (100 ml/min) and detecting any traces of helium on the primary side with gas chromatography. Due to improper sealing the flux measurements were not carrier out.

Chapter 4

Results

4.1 Powder characterization

4.1.1 LSFTa powder by solid state synthesis

The XRD-pattern of the solid state synthesized LSFTa powder is shown in Figure 4.1 and confirms that a single phase compound was produced. The best match for the pattern was obtained with the cubic perovskite $\mathrm{La_{0.2}Sr_{0.8}FeO_{2.97}}$ (LSF) using the ICDD PDF4+ database [52]; the missing peaks compared to the reference pattern is a cancellation due to the structure factor. Peak asymmetry in this and all the following XRD-patterns is due to K_{α_2}–radiation. The particle size distribution of the as-synthesized powder ball milled for 24 hours in ethanol is given in Figure 4.2 and shows that most of the particles are in the range of 2–40 μm. The average surface area of the same powder as measured by BET adsorption was found to be 0.9484 $\mathrm{m^2/g}$ (average of three samples, result graphs from the software are given in Appendix D). Assuming equally sized, spherical particles and using the theoretical density of $\rho_{\mathrm{LSFTa}} = 6.3\mathrm{g/cm^3}$ [53], this gives an average particle size of 1.0 μm for the primary particles. A SEM image showing the powder morphology is given in Figure 4.3. The particle size distribution is seen to be very wide and the shape of the particles is irregular. The result of the dilatometry analysis is given in Figure 4.4 where the dimensional change as a function of temperature is plotted. The onset of sample shrinkage is found at 1200°C and the derivative curve show that the maximum shrinkage is around 1350°C.

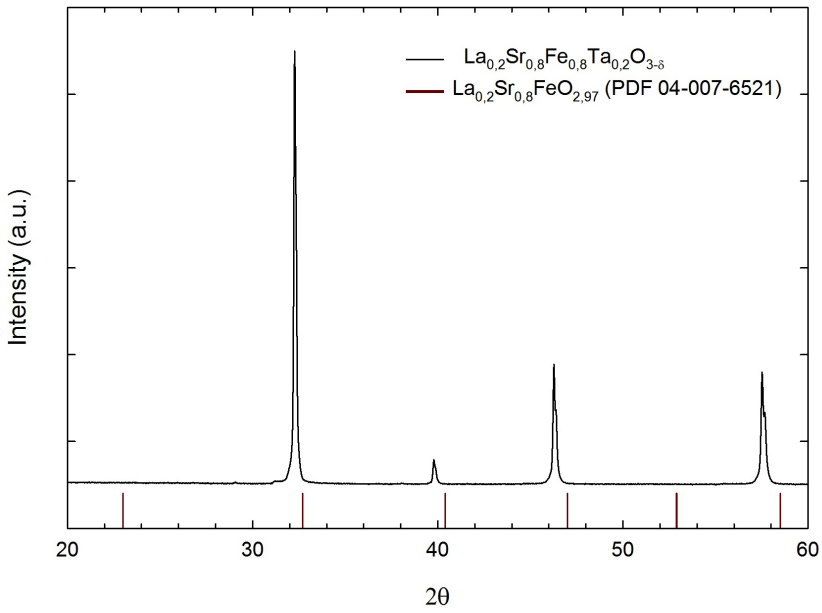

Figure 4.1: XRD pattern of solid state synthesized LSFTa, matched to the cubic perovskite $La_{0.2}Sr_{0.8}FeO_{2.97}$ in the ICDD PDF4+ database [52].

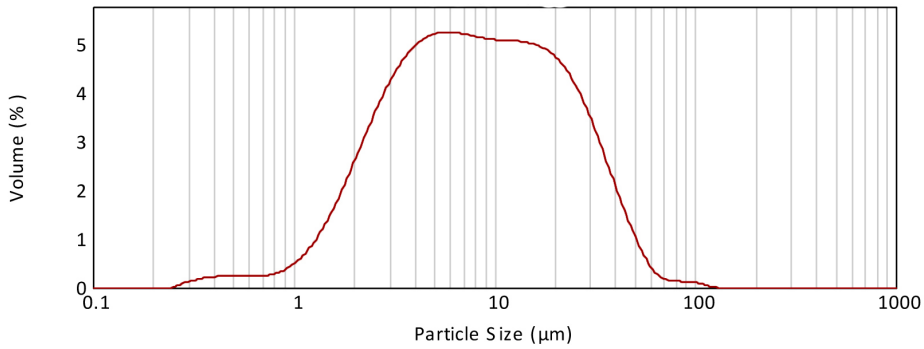

Figure 4.2: Particle size distribution of solid state synthesized LSFTa powder after milling for 24 hours in ethanol. Measured by laser diffraction.

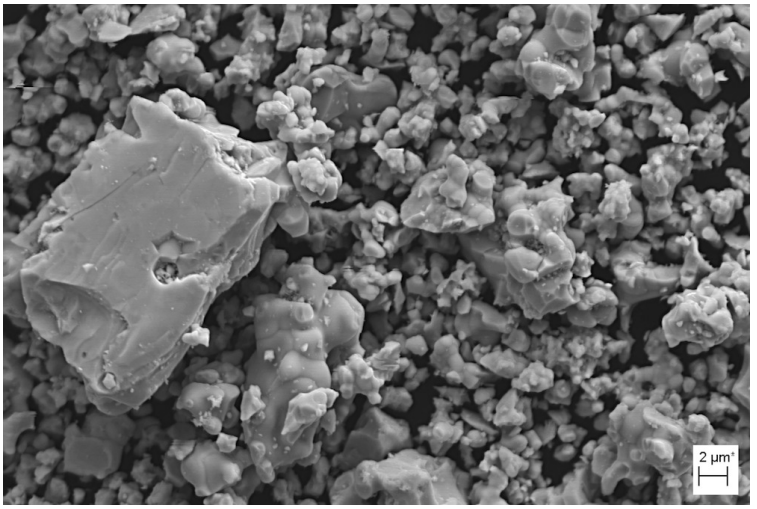

Figure 4.3: SEM image of the solid state synthesized LSFTa powder after milling for 24 hours in ethanol.

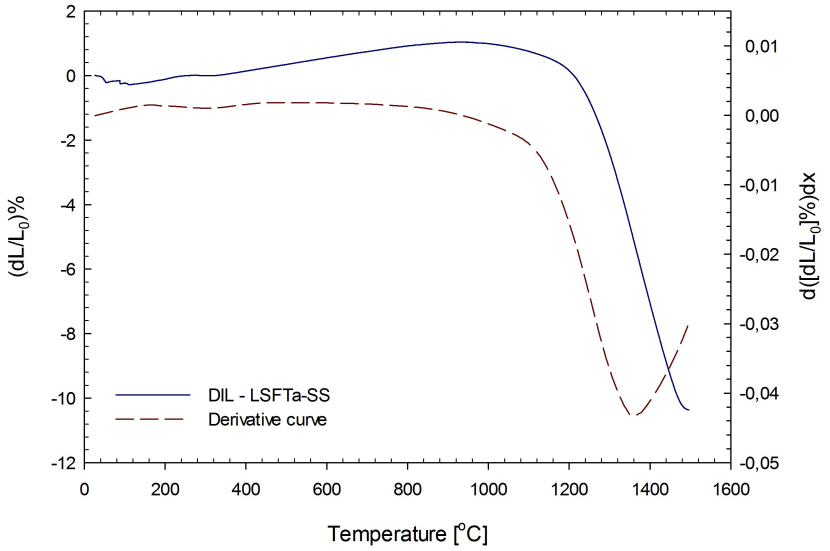

Figure 4.4: Dilatometry analysis of the solid state synthesized LSFTa powder. The derivative curve has been smoothed.

4.1.2 LSFTa powder by spray pyrolysis

The XRD pattern of the LSFTa powder synthesized by spray pyrolysis is given in Figure 4.5 and confirms a phase pure compound was produced. The average BET surface area of the calcined powder after milling for 24 hours in ethanol was measured to be 18.0355 m^2/g (average of two measurements, result graphs from the software are given in Appendix D) and the particle size distribution both before and after milling is shown in Figure 4.6. The second peak in the particle size distribution curve for LSFTa-SP after milling is ascribed to re-agglomeration of the powder during execution of the measurement. The particle size calculated from the BET surface area assuming spherical particles is approx. 53 nm. SEM images of the as-synthesized powder and after milling are given in Figure 4.7. Before milling (4.7a) the powder is seen to consist of large, egg-shell like agglomerates, which are broken down to sub-micrometer particles after milling (4.7b).

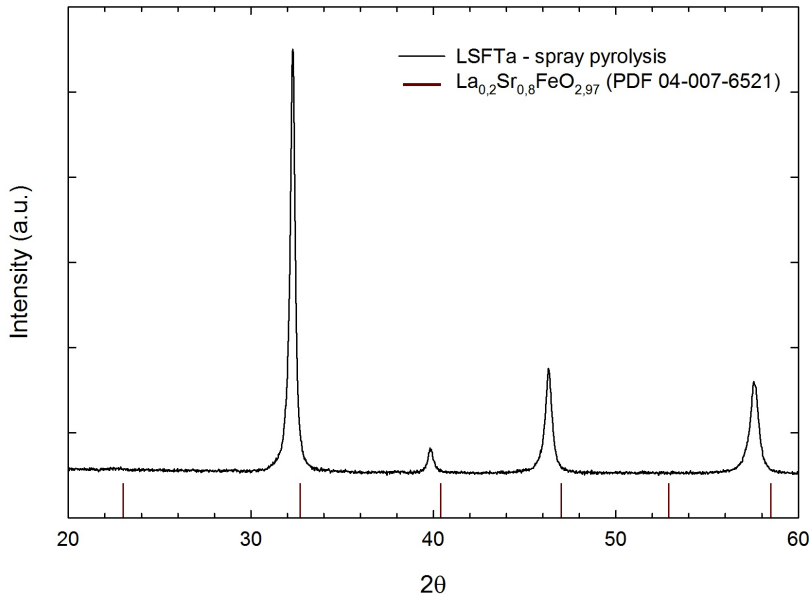

Figure 4.5: XRD pattern of LSFTa powder synthesized by spray pyrolysis, matched to the cubic perovskite $\mathrm{La_{0.2}Sr_{0.8}FeO_{2.97}}$ in the ICDD PDF4+ database [52]

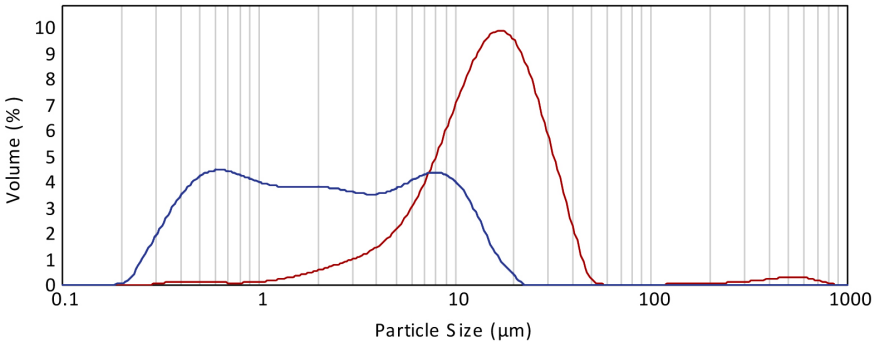

Figure 4.6: Particle size distribution of LSFTa powder synthesized by spray pyrolysis. "As-synthesized", after calcining at 900°C for 12 hours, (red curve) and after milling in ethanol for 24 hours (blue curve).

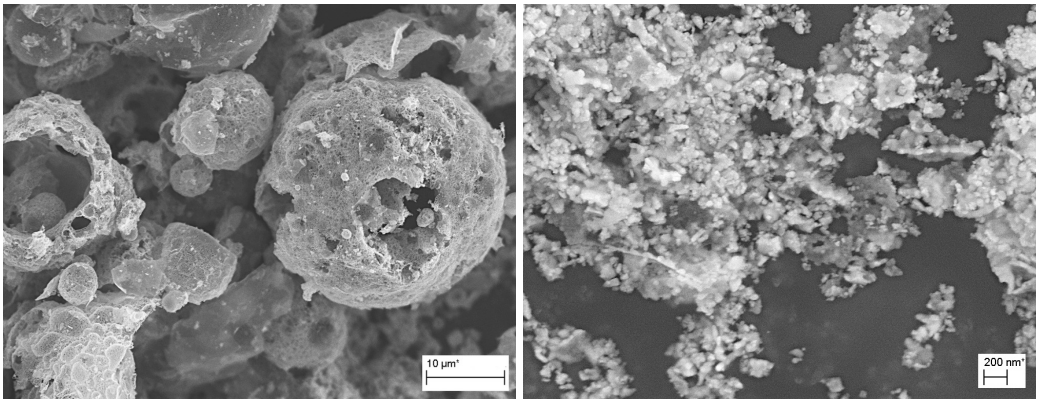

(a) Before milling (b) After milling

Figure 4.7: SEM of LSFTa powder synthesized by spray pyrolysis before (a) and after (b) milling in ethanol for 24 hours. Notice the difference in scale.

4.1.3 LSFAl powder by solid state synthesis

A SEM image of the solid state synthesized LSFAl powder after milling in ethanol for 24 hours is given in Figure 4.8. The XRD-pattern of the powder is given in Figure 4.9 with the area between $24 \leq 2\theta \leq 32$ highlighted in a logarithmic plot of the intensity. The results show that a single phase perovskite matched to LSF was successfully synthesized. The particle size distribution of the powder after milling for 24 hours is given in Figure 4.10 and the surface area as measured by BET adsorption was found to be $1.8852\ \mathrm{m}^2/\mathrm{g}$ (result graph from the software is given in Appendix D). Assuming equally sized, spherical particles and using the theoretical density of $\rho_{\mathrm{LSFAl}} = 5.54\mathrm{g}/\mathrm{cm}^3$ [54], this gives an average particle size of 0.57 μm for the primary particles. The dilatometry analysis of the powder is given in Figure 4.11 and shows that the onset of sintering is located around 1150°C. The derivative curve of the DIL-analysis shows that the maximum shrinkage is at 1450 °C.

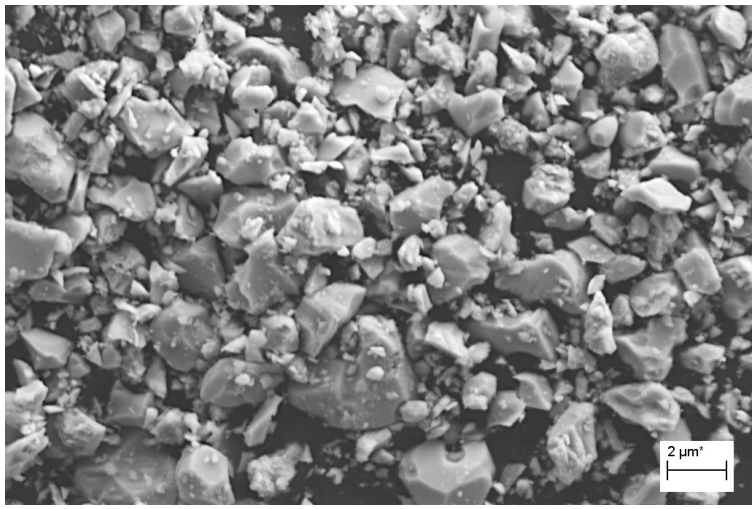

Figure 4.8: SEM image of the solid state synthesized LSFAl powder after milling for 24 hours in ethanol.

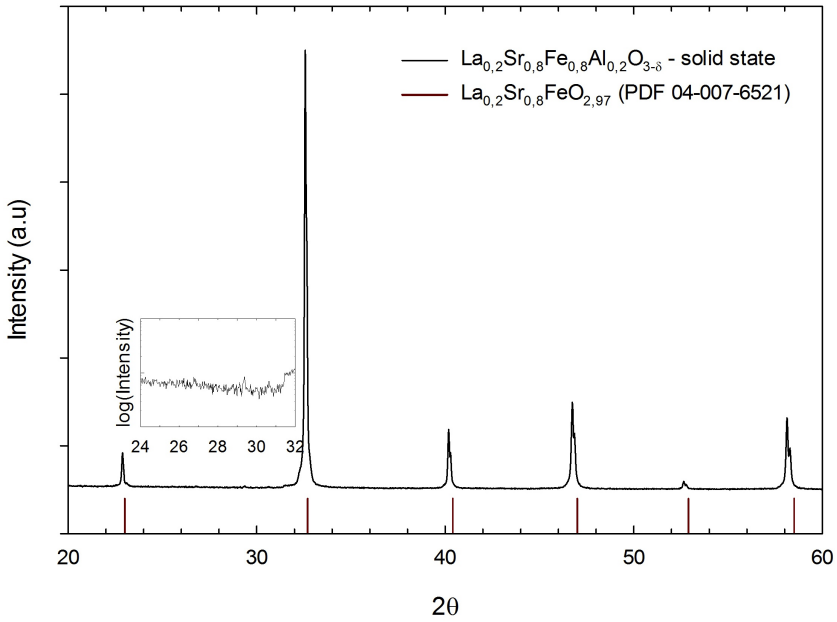

Figure 4.9: XRD pattern of solid state synthesized LSFAl, matched to the cubic perovskite $La_{0.2}Sr_{0.8}FeO_{2.97}$ in the ICDD PDF4+ database [52]. Inserted graph has the intensity plotted on a logarithmic scale and highlights the area between $24 \leq 2\theta \leq 32$.

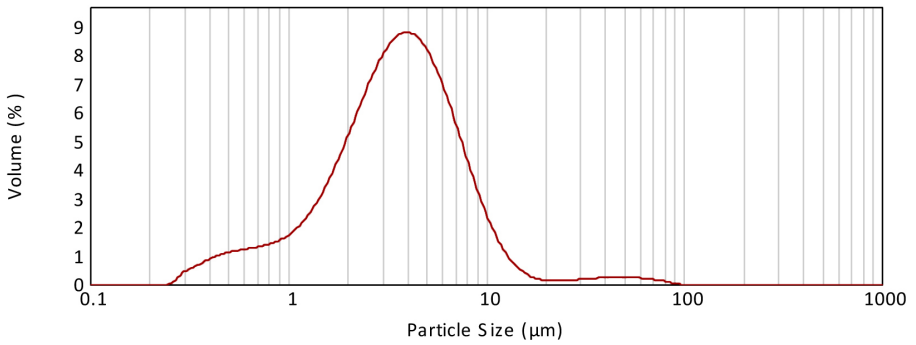

Figure 4.10: Particle size distribution of solid state synthesized LSFAl powder after milling in ethanol for 24 hours.

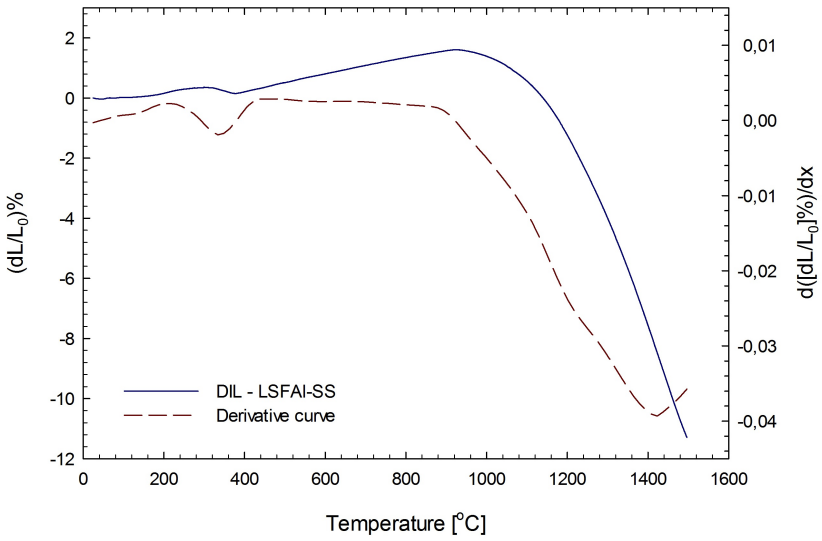

Figure 4.11: Dilatometry analysis of the solid state synthesized LSFAl powder. The derivative curve has been smoothed.

4.1.4 LSFAl powder by spray pyrolysis

The XRD-pattern of the as-received LSFAl spray pyrolysis powder is given in Figure 4.12 with the area between $24 \leq 2\theta \leq 32$ highlighted in a logarithmic plot. The main part of the pattern is matched to $La_{0.2}Sr_{0.8}FeO_{2.97}$, but the logarithmic plot shows traced of a secondary phase around 2θ=25. There was not found any good matches for this secondary peak in the ICDD PDF4+ database. The particle size distribution of the as-received powder and after milling in ethanol for 24 hours is shown in Figure 4.13. The BET surface area of the powder after milling was measured to be 13.38 m^2/g (result graph from the software is given in Appendix D) corresponding to an average particle size around 81 nm. The SEM-images of the as-received powder and after milling in ethanol for 24 hours is given in Figure 4.14. Before milling the powder is seen to consist of large agglomerates, which are successfully broken down during milling in ethanol. The results of the DIL analysis are given in Figure 4.15. The onset of sintering is found at 1000°C, while the derivative curve reveals a maximum shrinkage at 1130°C.

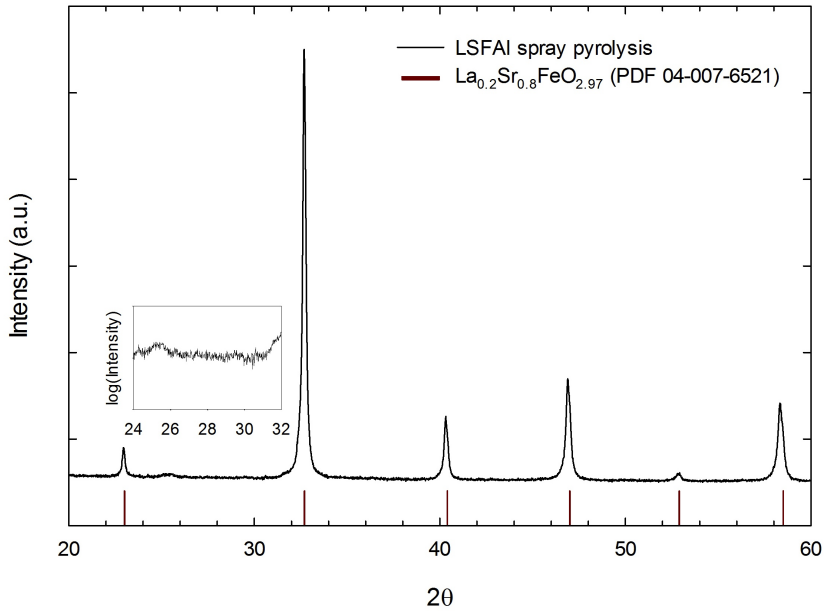

Figure 4.12: XRD pattern of LSFAl powder synthesized by spray pyrolysis, matched to the cubic perovskite $La_{0.2}Sr_{0.8}FeO_{2.97}$ in the ICDD PDF4+ database [52]. Inserted graph has the intensity plotted on a logarithmic scale and highlights the area between $24 \leq 2\theta \leq 32$.

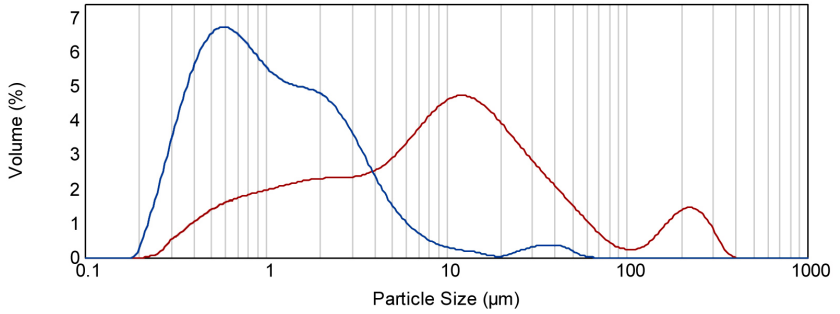

Figure 4.13: Particle size distribution of LSFAl powder synthesized by spray pyrolysis, as-received (red curve) and after milling in ethanol for 24 hours (blue curve).

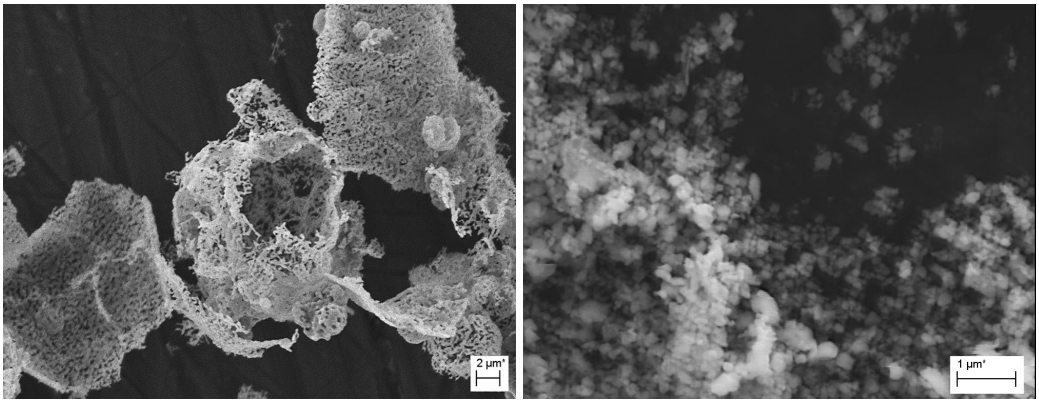

(a) As-received (b) After milling

Figure 4.14: SEM of LSFAl powder synthesized by spray pyrolysis as-received and after milling in ethanol for 24 hours. Notice the difference in scale.

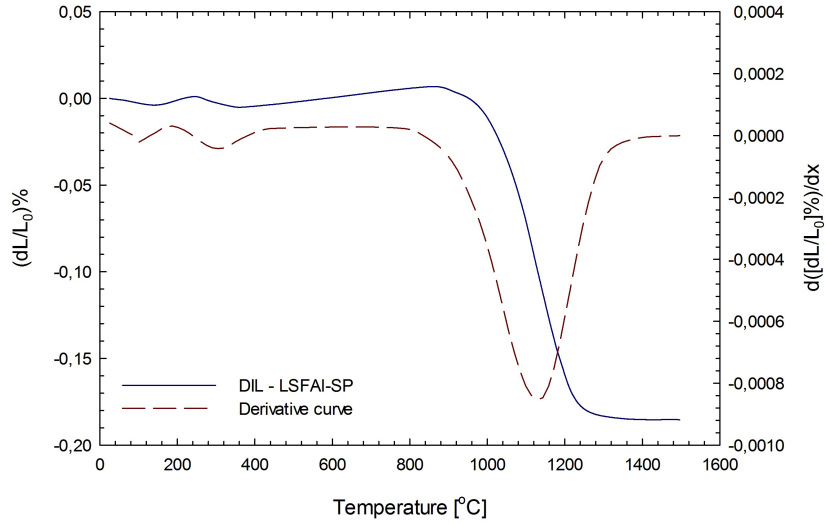

Figure 4.15: Dilatometry analysis of the LSFAl spray pyrolysis powder. The derivative curve has been smoothed.

4.2 LSFTa asymmetric membrane

4.2.1 Zeta potential and rheology of suspensions

The XRD-patterns of LSFTa powder exposed to solutions of three different pH-values is shown in Figure 4.16 together with the reference peaks of LSF. The XRD scan shows no evidence of change in powder composition over the pH range of 4.5–10.7. The results of the zeta potential measurements are given in Figure 4.17 and 4.18. The raw data may be found in Appendix E. The zeta potential of pure LSFTa powder in distilled water shows a shift from positive to negative values at around pH 6.7. A negative zeta potential over the entire pH range was measured for the samples containing Darvan-CN dispersant. In most cases the trend was a more negative zeta potential as the pH was increased. Inspection of the capillary cell after performing the measurements for the sample with 0.47 wt.% of Darvan CN revealed that the particles had settled to the bottom of the cell. This was not observed for the other samples.

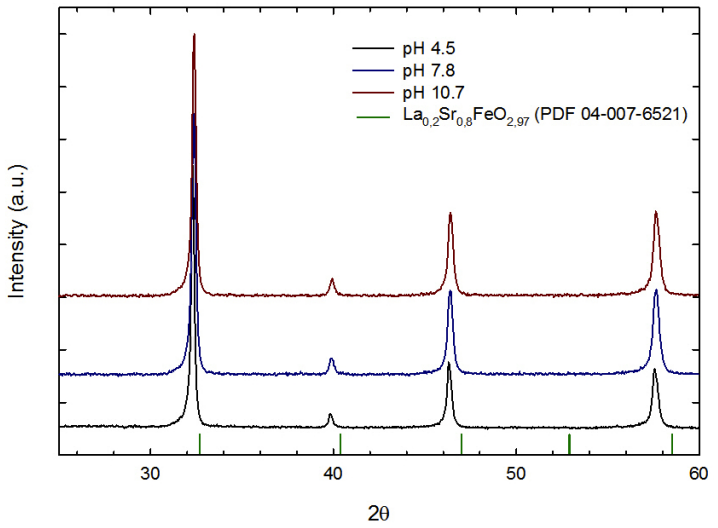

Figure 4.16: XRD-patterns of LSFTa powder exposed to solutions of three different pH values.

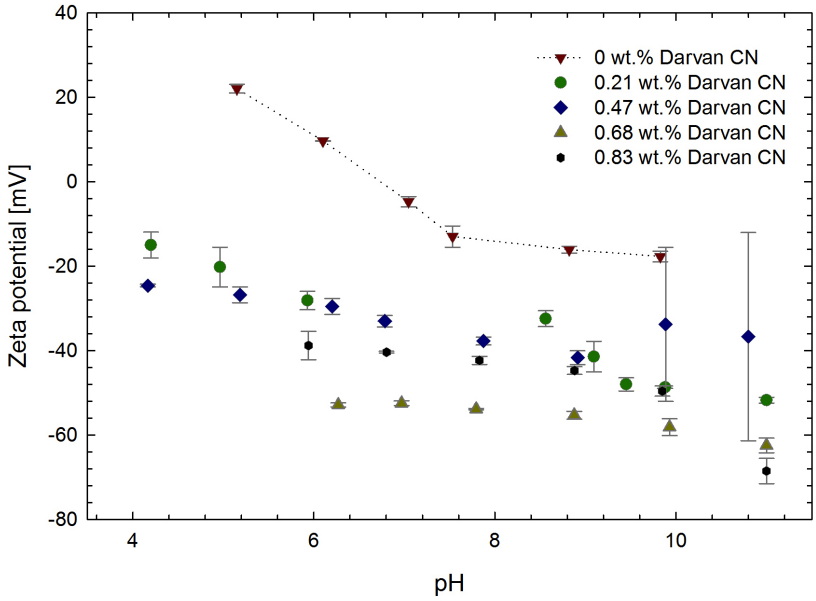

Figure 4.17: Zeta potential of LSFTa in distilled water as a function of pH and amount of Darvan C-N relative to powder. The points show the average of three measurements and the error bars show the standard deviation. The line for 0 wt.% of Darvan CN is added as a guide for the eye.

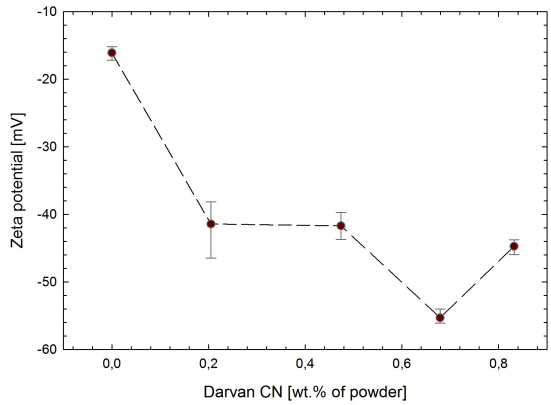

Figure 4.18: Zeta potential of LSFTa in distilled water as a function of amount of Darvan C-N relative to powder. Measured at pH $\sim$ 9. The line is added as a guide for the eye.

The shear stress as a function of shear rate for the high solid loading LSFTa suspensions are given in Figure 4.20 and show that a hystereses is formed between the upward and downward curve segments. The smallest hysteresis is found for the suspension containing 0.4 wt.% Darvan C-N. The viscosity of the same suspensions as a function of shear rate is given in Figure 4.21. Only the downward segment of the curve (recorded from 500 s^{-1} to 0 s^{-1}) is plotted to avoid the effect of difference in pre-shear history. The insert graph shows the viscosity at a shear equal to 100 s^{-1} plotted as a function of dispersant content. The first possible minima is found at 0.4 wt.% of Darvan CN, but an even lower viscosity is measured for 0.6 wt.% of Darvan CN. Considering the measured surface area, 0.6 wt.% of dispersant corresponds to 1.58 mg/m^2 Darvan CN per surface area of LSFTa powder[2].

The particle size distributions of the four suspensions with different amounts of Darvan CN added are given in Figure 4.19. The particle size is seen to be considerably reduced compared to the as-synthesized LSFTa powder shown in Figure 4.2. The difference between the curves with different amounts of Darvan CN added is within the error of what can be expected from different sample selections.

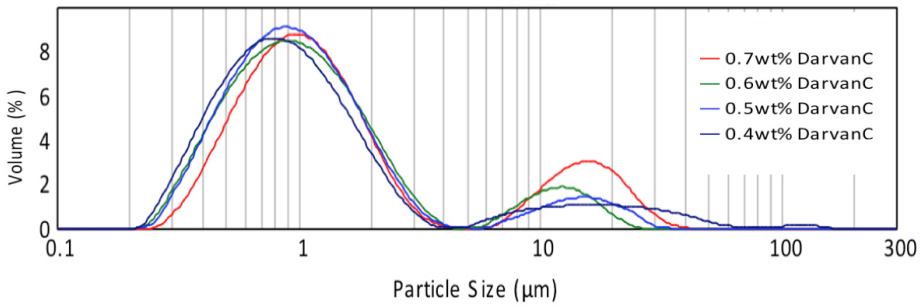

Figure 4.19: Particle size distibutions of LSFTa suspensions (15 vol.% solid loading) with different amounts of Darvan C-N added.

[2]Calculated based on the fact Darvan CN was supplied in a 25 wt.% water dilution.

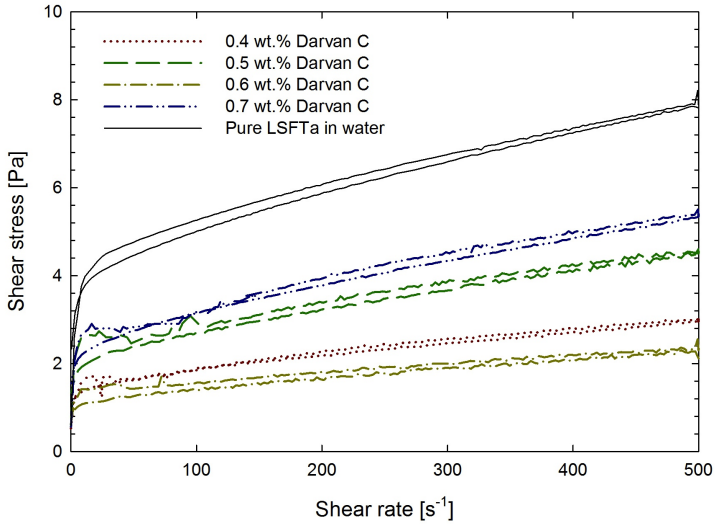

Figure 4.20: Shear stress vs. shear rate of LSFTa suspensions (15 vol.% solid loading) with different amounts of Darvan C-N added.

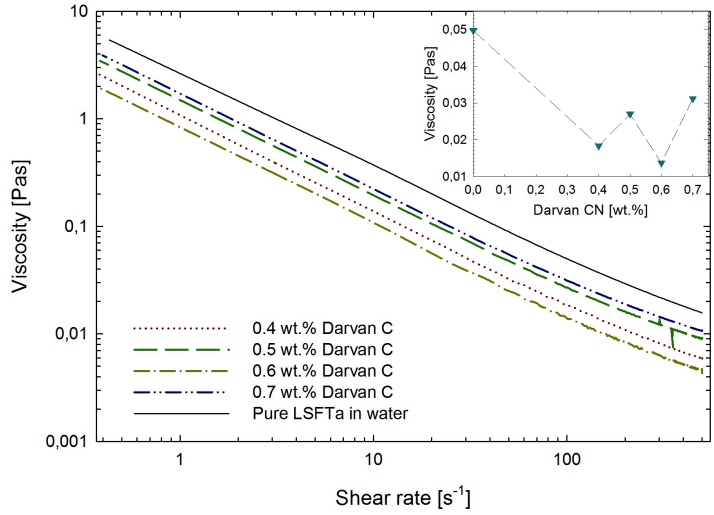

Figure 4.21: Viscosity as a function of shear rate for concentrated LSFTa suspensions (15 vol.% solid loading) with different amounts of Darvan C-N added. The insert graph shows the viscosity at a shear equal to 100 s^{-1} plotted as a function of dispersant content.

4.2.2 Tape casting of LSFTa porous supports

The rheology of the two tape casting slips specified in Table 3.9 was characterized and the results in the form of shear stress and viscosity vs. shear rate are given in Figures 4.23 and 4.24, respectively. For both of the tapes a positive hysteresis is seen to form between the upward and downward segments of the shear stress vs. shear rate curves. The viscosity of *Tape 1* was found to be overall higher compared to the viscosity of *Tape 2*. Pictures of the tapes casted from the two slips are shown in Figure 4.22. *Tape 1* curled up along the edges and cracked during drying (Figure 4.22a). *Tape 2* was however found to be defect-free, flexible and almost flat. The thickness of this tape varied between 0.08 and 0.13 mm.

(a) Green tape of LSFTa porous support casted with the slip specified as *Tape 1* in Table 3.9. 16.7 vol.% solid loading. The tape curled up and cracked during drying.

(b) Green tape of LSFTa porous support casted with the slip specified as *Tape 2* in Table 3.9. 15.8 vol.% solid loading. The tape was homogeneous, nearly flat and very flexible.

Figure 4.22: Green tapes of LSFTa porous support.

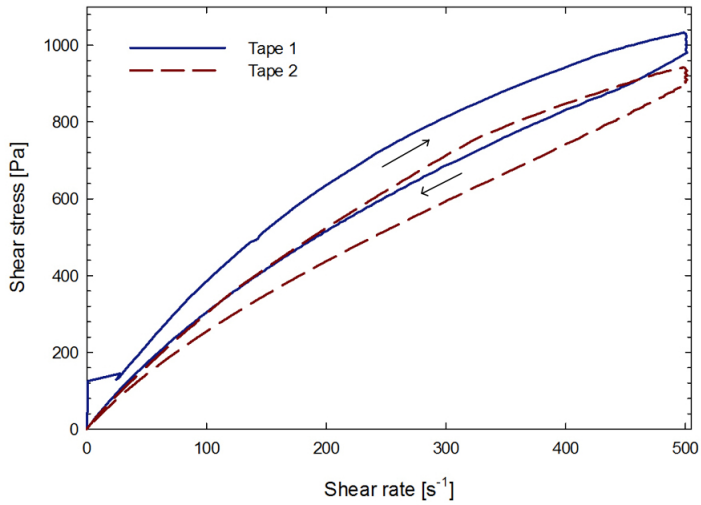

Figure 4.23: Shear stress vs. shear rate of LSFTa tape casting slips

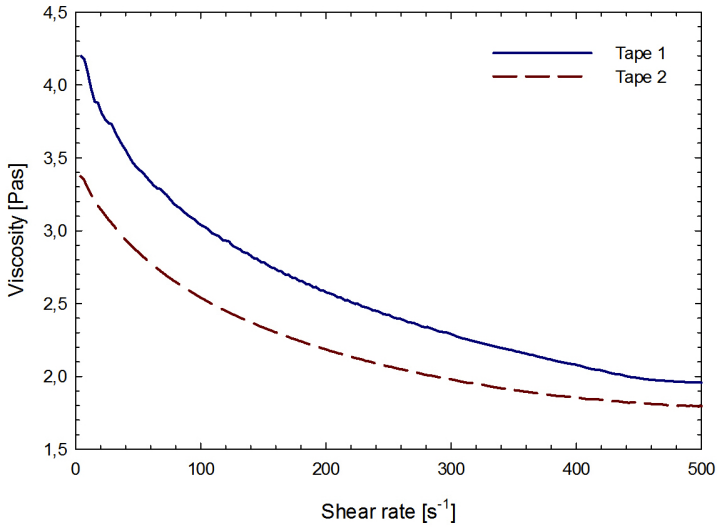

Figure 4.24: Viscosity as a function of shear rate for LSFTa tape casting slips

4.2.3 Dip coating and sintering of LSFTa porous supports

SEM images of the LSFTa porous support top surface after sintering at 1150°C and 1190°C are shown in Figure 4.26. It can be seen from these images that the contact between the particles in the support sintered at 1150°C is less compared to the support sintered at 1190°C. The particle size distribution of the as-prepared 0.5 vol.% dip coating suspension is given in Figure 4.25. Since the suspension was stored before use, a re-measurement of the particle size distribution was done right before performing the dip coating. No indications of the suspension having agglomerated were found as the distribution was similar to that given in Figure 4.25.

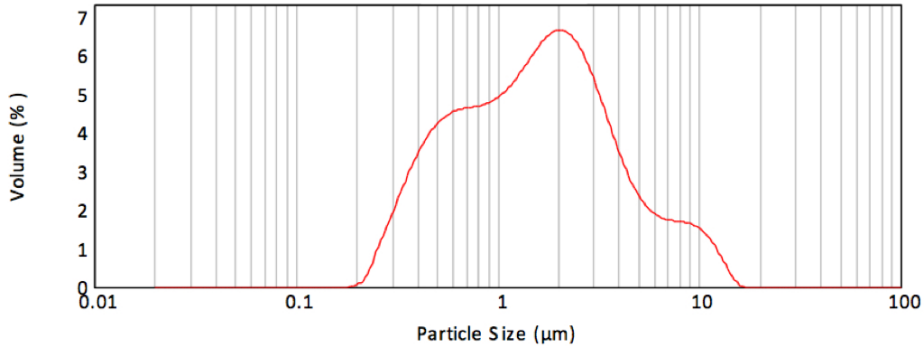

Figure 4.25: Particle size distribution of 0.5 vol.% LSFTa dip coating suspensions.

The support pre-sintered at 1150°C cracked when it was lowered in the dip coating suspension and was therefor excluded from further investigation. The results after dip coating the support pre-sintered at 1190°C can be seen in Figure 4.27. After the second round of dip coating and final sintering at 1230°C, the surface of the porous support was seen to be for the most part completely covered by the dense layer. Around 15–20 smaller holes as those visible in Figure 4.27b were observed in the whole sample surface (total area: $\sim$ 300 cm^2) . The inserted picture of Figure 4.27b shows that most of the grains in the top surface are in the sub-micrometer range. The cross section is shown in Figure 4.28; the thickness of the dense layer was measured to be 6-7 μm. After the final sintering, the open porosity of the asymmetric membrane was determined by Archimedes' method to be 38 %. Details of the measurement are given in Appendix F.

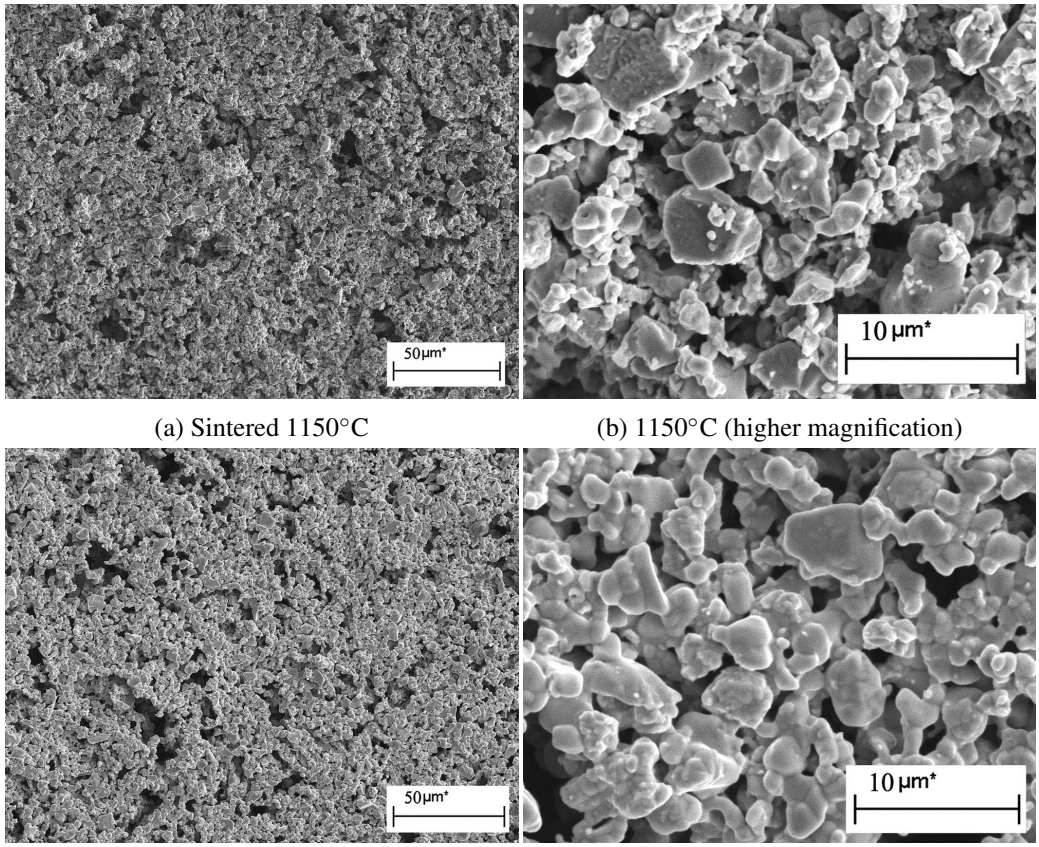

(a) Sintered 1150°C

(b) 1150°C (higher magnification)

(c) Sintered 1190°C

(d) 1190°C (higher magnification)

Figure 4.26: SEM of LSFTa porous supports sintered at two different temperatures. All images show the top surface of the porous support.

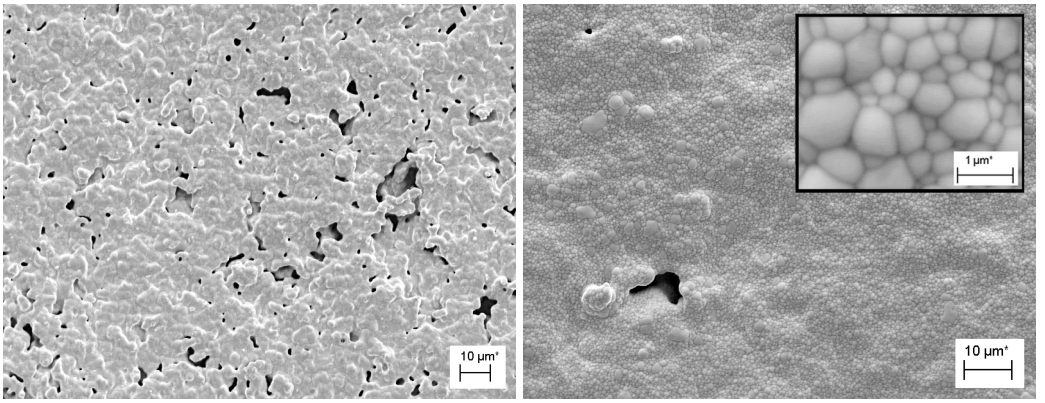

(a) Dip coated 1x (b) Dip coated 2x

Figure 4.27: SEM image of the LSFTa asymmetric membrane top surface after dip coating one and two times. Final sintering was performed at 1230°C.

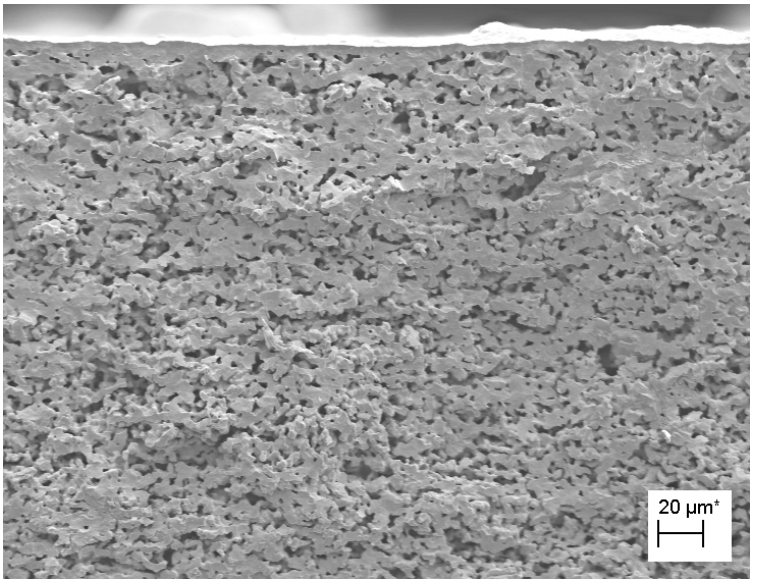

Figure 4.28: SEM of the LSFTa asymmetric membrane cross section. Prepared from porous support pre-sintered at 1190°C, dip coated twice and finally sintered at 1230°C.

4.3 LSFAl asymmetric membrane

4.3.1 Tape casting of LSFAl porous supports

LSFAl slips prepared following the procedure described by Lagergren [20] resulted in tapes of generally good quality. The thickness varied between 0.25 and 0.30 mm and the tapes were flexible and uniform. The tape after drying is shown in Figure 4.29, where some pinholes are highlighted. The LSFAl slip prepared following the procedure described for tape casting LSFTa resulted in a slip that coagulated and attained a foam-like structure. The casted tape was found to be very stiff and brittle after drying. An image of the tape is shown in Figure 4.30, where a large crack can be observed.

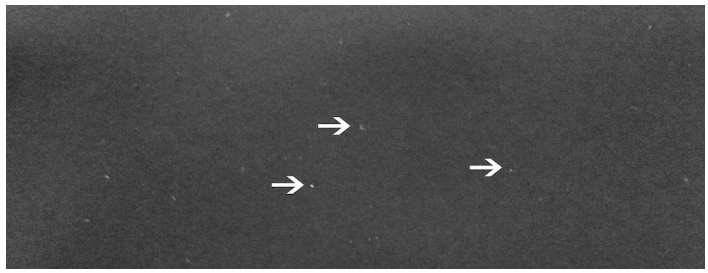

Figure 4.29: Green tape of LSFAl porous support made by following the procedure specified in Figure 3.3. The arrows show some of the pinholes in the dried tape.

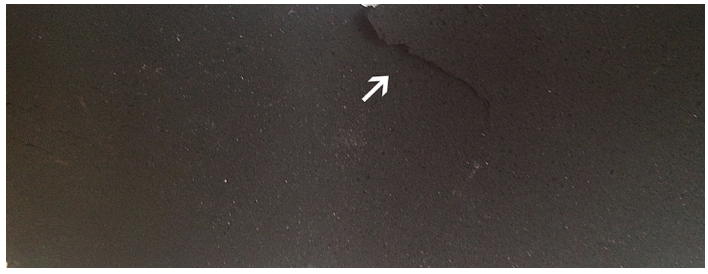

Figure 4.30: Dried tape casted from the LSFAl slip prepared following the same procedure as for making LSFTa tape casting slip, specified in Figure 3.1. The slip was heavily coagulated and the casted tape was very weak. The arrow highlights a crack.

4.3.2 Sintering of LSFAl porous supports

SEM images of the LSFAl porous support sintered at 1200°C, 1250°C and 1300°C are shown in Figure 4.31. The porous support sintered at 1150°C was too weak to handle and was therefore excluded from further investigations.

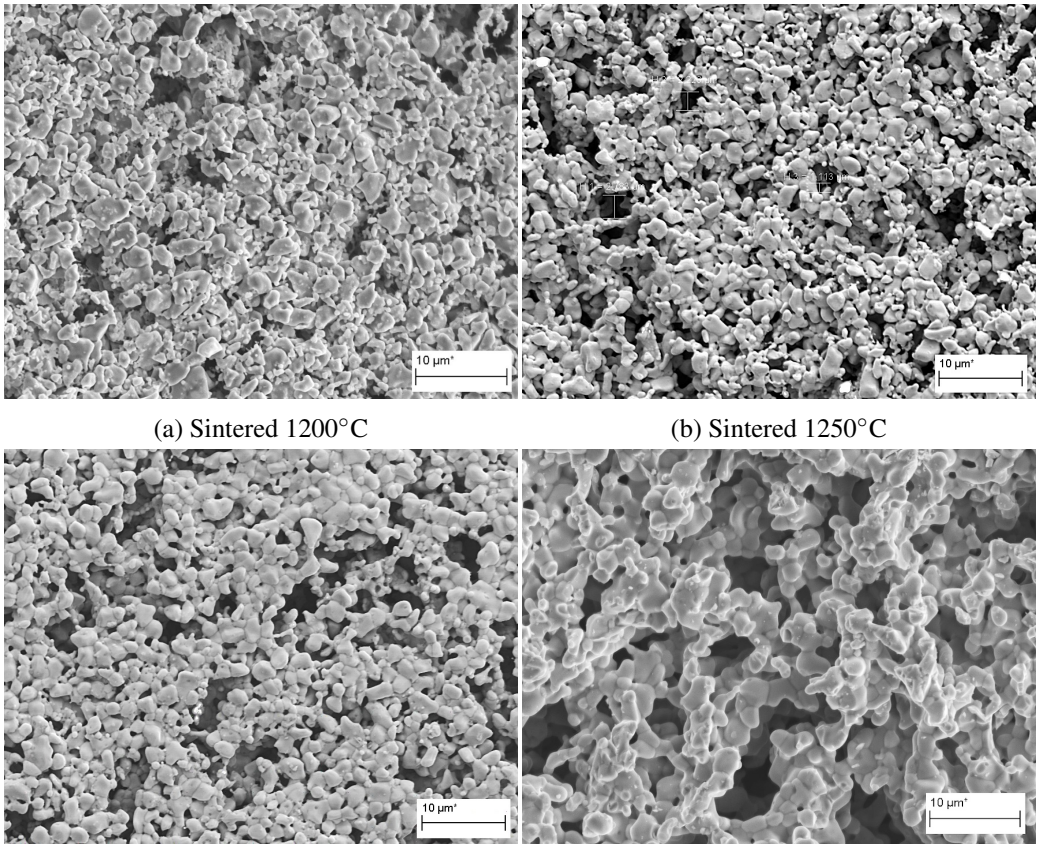

(a) Sintered 1200°C (b) Sintered 1250°C

(c) Sintered 1300°C (d) Sintered 1300°C, polished

Figure 4.31: SEM of LSFAl porous supports sintered at various temperatures.
All images show the top surface of the porous support.

4.3.3 Dip coating and sintering of LSFAl asymmetric membrane

The particle size distributions of the dip coating suspension with 0.5 vol.% solid loading prepared from pre-milled spray pyrolysis powder is shown in Figure 4.32. The particle size for the 0.75 vol.% suspension prepared from pre-milled powder is comparable.

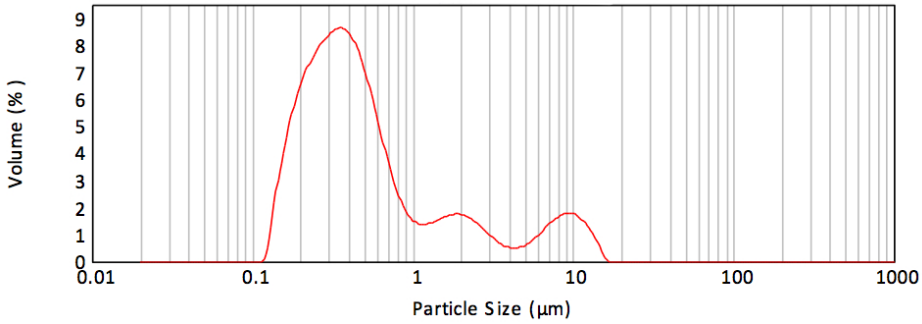

Figure 4.32: Particle size distribution of 0.5 vol.% LSFAl dip coating suspension.

The porous supports were dip coated with the 0.5 vol.% suspension up to four times with heat-treatments in-between. The support pre-sintered at 1200°C cracked repeatedly during the first dip coating cycle (three of three supports that were attempted to dip coat failed), this is shown in Figure 4.33. A part of the cracked membrane was sintered and used further. SEM images showing the development of the top surface after each dip coating and heat-treatment cycle is given in Figure 4.34 for the support pre-sintered at 1200°C, Figure 4.35 for the support pre-sintered at 1250°C and Figure 4.36 for the support pre-sintered at 1300°C. The support that was pre-sintered at 1300°C and polished before dip coating is shown in Figure 4.37. The SEM of the cross sections of each of the samples after the final dip coating cycle is presented in Figure 4.38. Note that all of the specimens were sintered at 1300°C after the final dip coating.

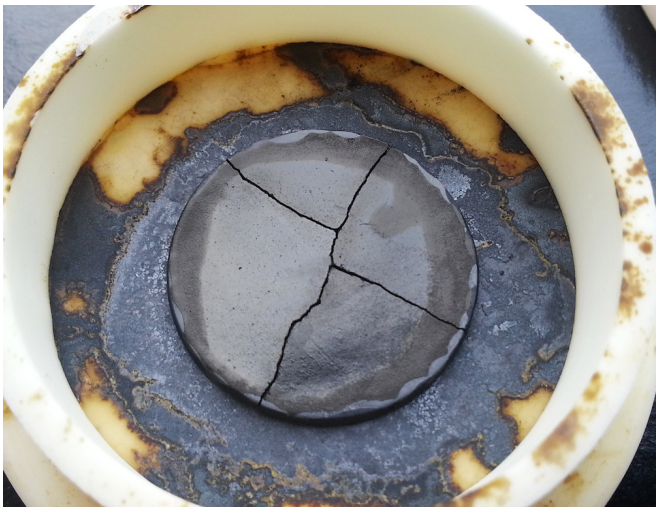

Figure 4.33: Picture of the LSFAl porous support pre-sintered at 1200°C. The support cracked while being immersed in the dip coating suspension.

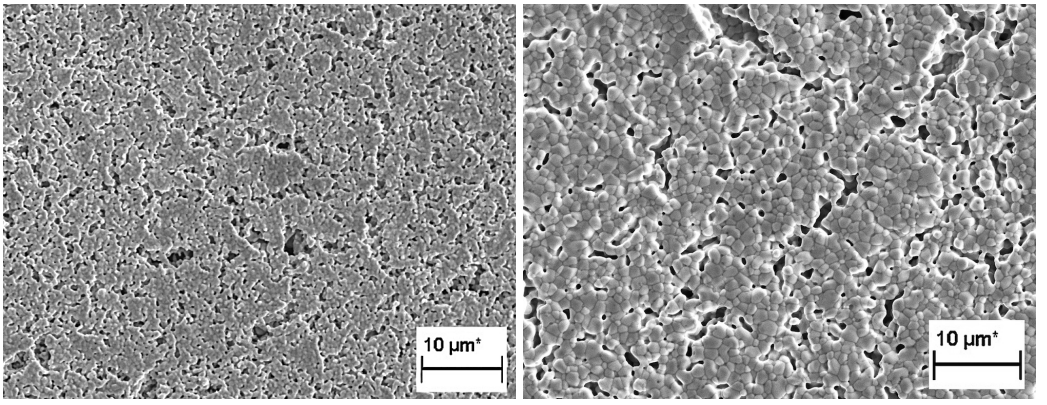

(a) Dip coated 1x (b) Dip coated 2x

Figure 4.34: SEM images of LSFAl porous support pre-sintered 1200°C after dip coating one and two times.

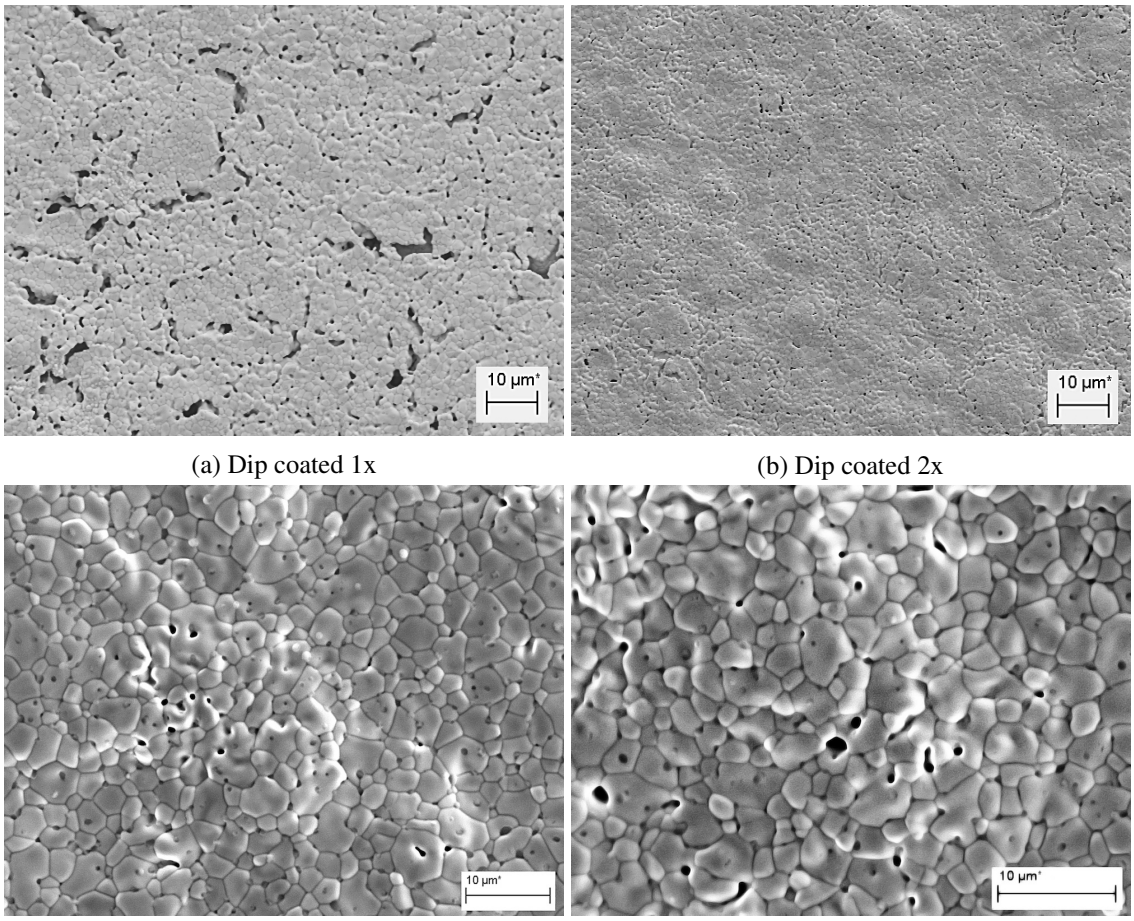

(a) Dip coated 1x

(b) Dip coated 2x

(c) Dip coated 3x

(d) Dip coated 4x

Figure 4.35: SEM images of the LSFAl porous support pre-sintered at 1250°C after dip coating 1, 2, 3 and 4 times and final sintering at 1300°C. Note the increased magnification for the two lower images.

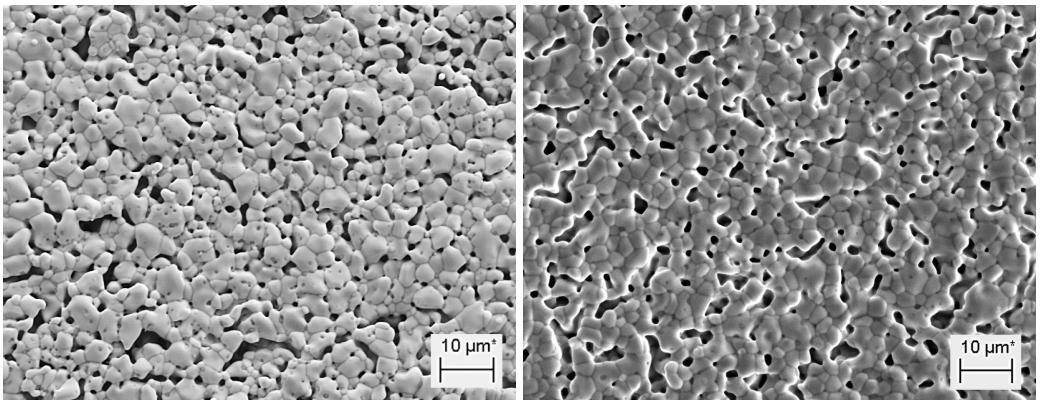

(a) Dip coated 1x (b) Dip coated 2x

Figure 4.36: SEM images of LSFAl porous support pre-sintered at 1300°C after dip coating 1 and 2 times and sintering at 1300°C between each dip.

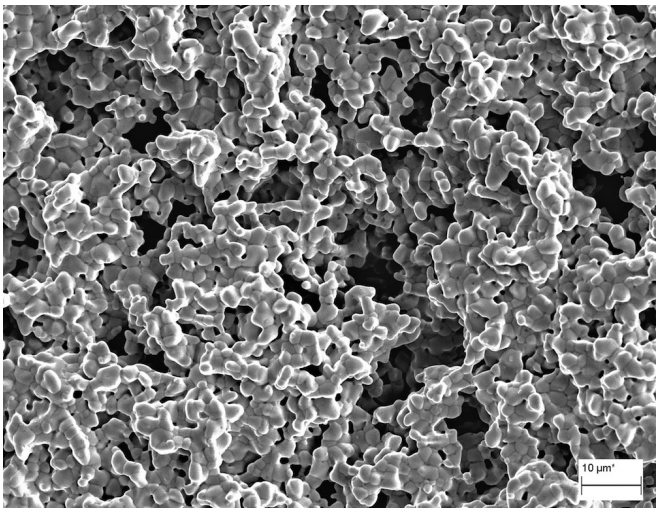

Figure 4.37: SEM image of the LSFAl porous support pre-sintered at 1300°C and polished with SiC-paper before dip coating 1x.

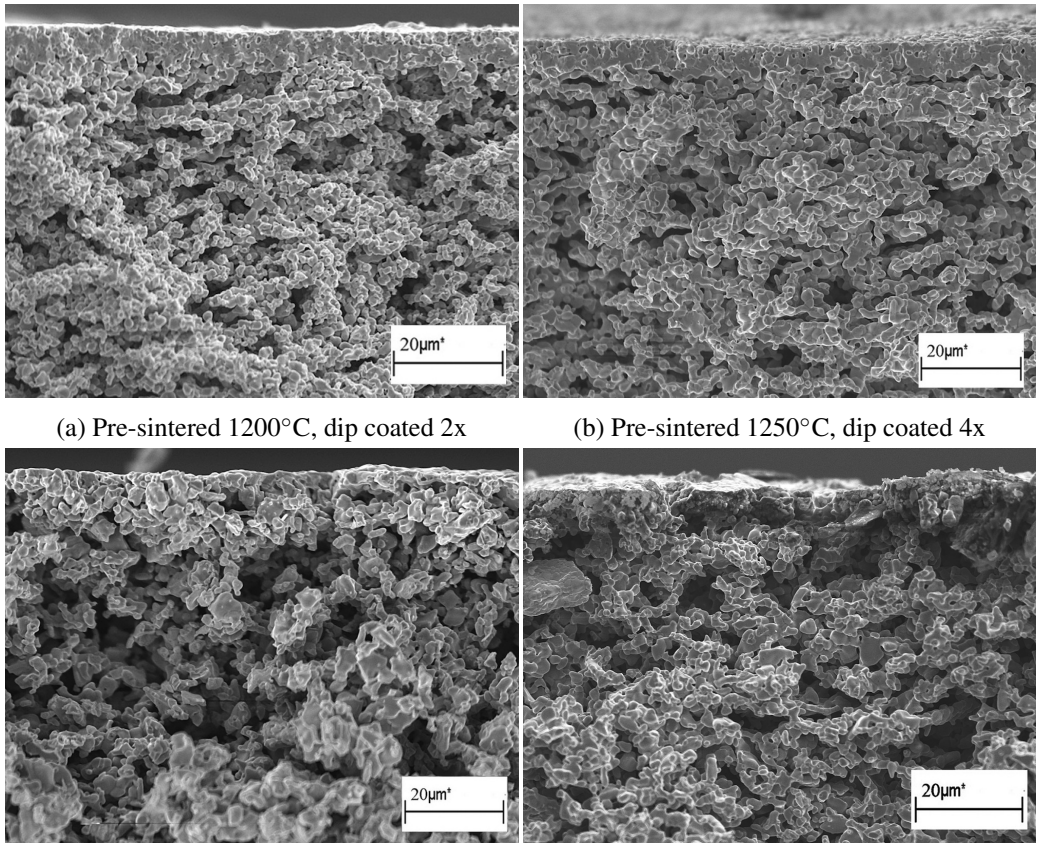

(a) Pre-sintered 1200°C, dip coated 2x

(b) Pre-sintered 1250°C, dip coated 4x

(c) Pre-sintered 1300°C, dip coated 2x

(d) 1300°C (polished), dip coated 2x

Figure 4.38: SEM of LSFAl asymmetric membrane cross sections. Sintering temperature after the final dip coating was 1300°C for all specimens.

The average porosity of the samples after the final dip coating with the 0.5 vol.% suspension and sintering at 1300°C was measured by Archimedes' method and reported in Table 4.1. The calculations and raw data are given in Appendix F.

Table 4.1: Archimedes' porosity of LSFAl supports pre-sintered at different temperatures. Measured after the final dip coating and sintering at 1300°C.

Calcination temperature [°C]	Open porosity [%]	Total porosity [%]
1200	62.3	63.3
1250	50.1	51.1
1300	65.0	65.6
1300-polished	72.0	72.8

One of the supports pre-sintered at 1250°C was dip coated with the 0.75 vol.% suspension. The SEM image showing the result after the first and third dip coating and sintering cycle is given in Figure 4.39a.

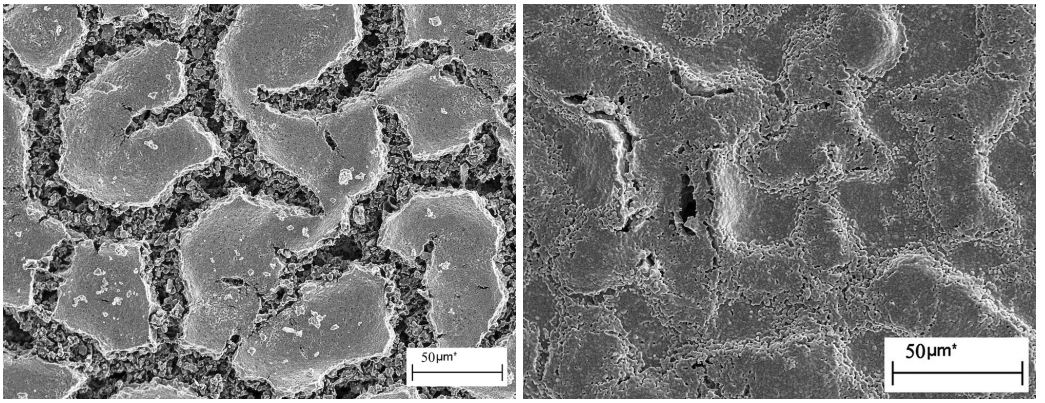

(a) Dip coated 1x (b) Dip coated 3x

Figure 4.39: Top surface SEM image of an LSFAl porous support dip coated with the 0.75 vol.% solid loading suspension.

4.3.4 Phase purity and stability

In all of the SEM images of the LSFAl asymmetric membrane top surface some smaller grains are visible both in-between and in the middle of the grains of the main structure. The SEM backscatter detector image in Figure 4.40 reveals that these smaller grains have a different composition than the rest of the structure. The figure also highlights the points of the image that were analyzed by EDS. The results of the point analysis are presented in Table 4.2 and show that the smaller grains are enriched by Al and Sr compared to the larger grains. From the result-curve, spectrum point 6 is interpreted as a hole (the result-curves may be found in Appendix H). A XRD-pattern of the membrane top surface is shown in Figure 4.41. As shown in Figure 4.42 no good matches were obtained for the secondary phases.

Table 4.2: Results of EDS point analysis of the LSFAl asymmetric membrane top surface given in weight %. The spectrum points where the analysis is made are shown in Figure 4.40. Result curves may be found in Appendix H.

Spectrum nr.	La	Sr	Fe	Al	O	C
5	15.83	35.25	23.43	2.52	19.11	3.86
8	9.36	39.04	15.92	11.45	24.23	0

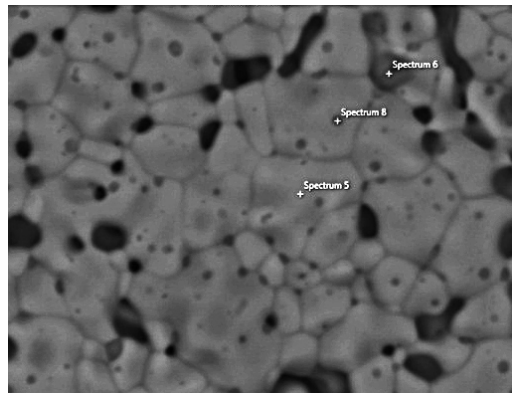

Figure 4.40: SEM backscatter detector image of the LSFAl asymmetric membrane top surface. The spectrum points show the points that were analyzed by EDS.

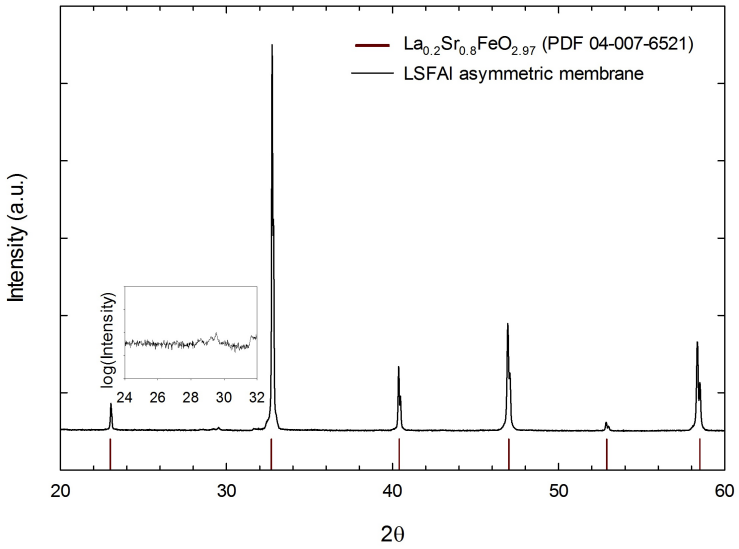

Figure 4.41: XRD pattern of the LSFAl asymmetric membrane top surface. Inserted graph highlights the area of 2θ 24 – 32 by showing the logarithm of the intensity.

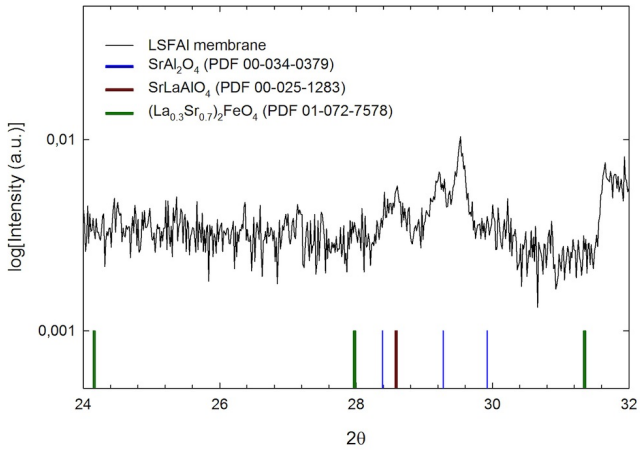

Figure 4.42: XRD of LSFAl asymmetric membrane top surface. The figure is a re-plot of Figure 4.41 highlighting the area of $24 \leq 2\theta \leq 32$. The reference peaks belong to the previously reported impurity phases present in the synthesis of LSFAl [20].

Secondary electron and backscatter electron SEM images of the LSFAl pellet top surface made are shown in Figure 4.43. The pellet was made by uniaxial pressing and sintering the powder at 1300°C for 2 hours. From the BSE-image no significant amount of secondary phases are apparent.

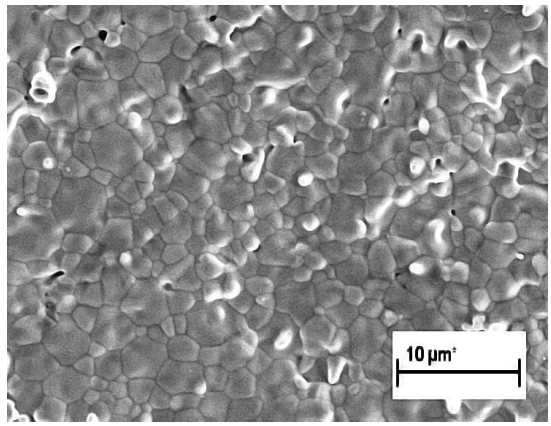

(a) Secondary electron image

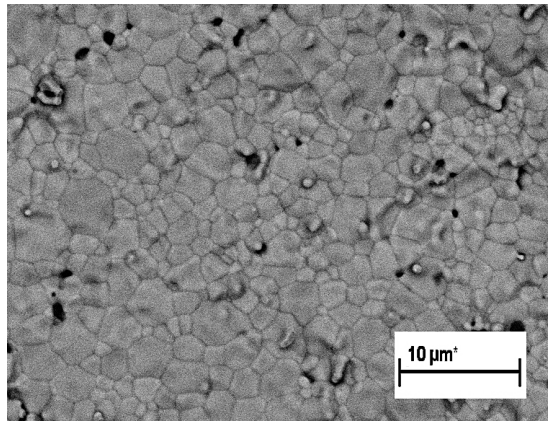

(b) Backscatter electron image

Figure 4.43: SEM of LSFAl pressed pellet made by the as-received spray pyrolysis powder.

4.3.5 Strength of LSFAl porous supports

The calculated strength of LSFAl porous supports tested by the ball-on-ring method is given in Table 4.3. Because the samples prepared were not completely flat and uniform, the given thickness is an average of three measurement points along each sample. Some of the supports had curled slightly during sintering, these are specified as "not flat" in the table. The total porosity of three samples was measured by Archimedes' method and is reported in Table 4.3. Details about the porosity measurements are given in Appendix F. The Weibull curve for the probability of failure is given in Figure 4.44. The slope of the linear regression line gives a Weibull modulus (m) equal to 5.9±1.8 and the characteristic strength, σ_0, is calculated to 10.7±0.5 MPa. All of the raw-data and details about the calculations may be found in Appendix G. The typical fracture surface cross section of the porous supports is shown in Figure 4.45a. Sample 4 was observed to have some areas of poor lamination between the layers, as evident in Figure 4.45b.

Table 4.3: Ball-on-ring fracture strength of LSFAl porous supports sintered at 1300°C. Thickness is the average from three measurement points on each sample. The load is the maximum measured load before failure.

Sample ID	Thickness [mm]	Max load [N]	Fracture strength [MPa]	Total porosity [%]	Comment
1	0.876	3.85	13.19	61.4	
2	0.822	2.49	9.76		Not flat
3	1.132	4.77	9.15		Not flat
4	0.958	3.05	8.47	64.5	
5	1.033	3.78	8.86		
6	0.959	3,45	9.62	64.4	
7	0.874	2.72	9.31		Not flat
8	1.124	3.97	7.74		Not flat
9	0.921	3.55	10.84		
10	0.836	3.34	12.65		
11	0.782	2.35	10.28		

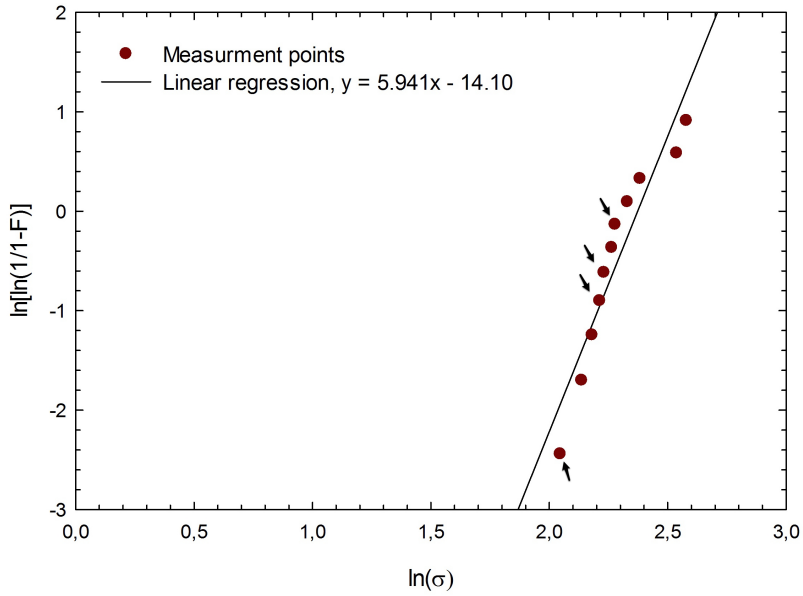

Figure 4.44: Weibull curve for the probability of failure of LSFAl porous supports sintered at 1300°C. The points are from the ball-on-ring measurement. The arrows show the specimens labeled "not flat" in Table 4.3.

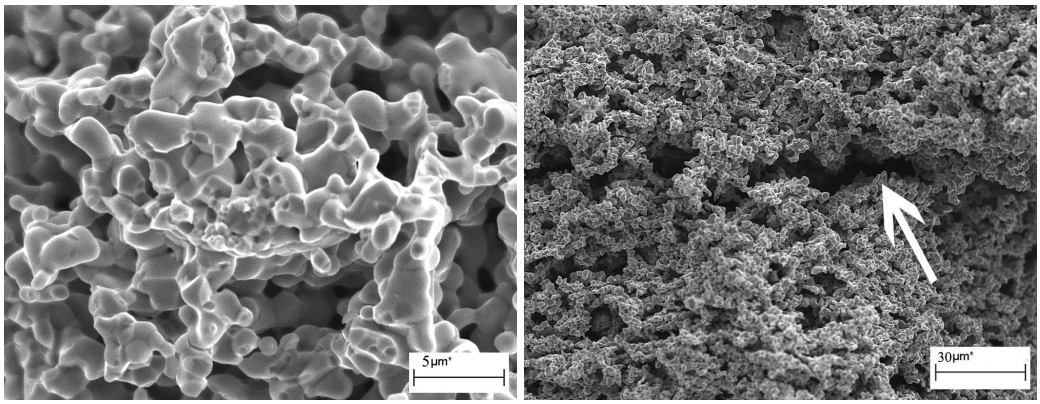

(a) Typical surface (b) De-lamination (sample 4)

Figure 4.45: SEM of LSFAl porous supports fracture surface after ball-on-ring strength testing.

4.3.6 Oxygen flux of LSFAl asymmetric membrane

The asymmetric membrane made from the support calcined at 1250°C was mounted into the flux furnace and heated for sealing. Gas chromatography measurement of the primary (air) side outlet gas detected considerable amounts of helium gas. After cooling down and taking the specimen out of the furnace, a crack was discovered in the asymmetric membrane. Because of time limitations, no more membranes were attempted measured in the flux furnace.

Chapter 5

Discussion

5.1 Powder properties in relation to synthesis method

The XRD-results showed that phase pure LSFTa was successfully synthesized by both solid state reaction (SSR) and spray pyrolysis (SP). The wider peaks in the pattern of the SP powder compared to the SSR powder can be related to the smaller crystallite size of the former. From the XRD-results the LSFAl powder synthesized by solid state reaction also appears to be phase pure. This is encouraging considering that Lagergren experienced difficulties with obtaining phase purity while using this synthesis method in previous work [20]. The only apparent difference in the procedure of the current work is that ball milling was used instead of planetary milling to mix the precursor powders before calcination. Different methods for milling and mixing of powders are known to give different results in terms of powder morphology and particle size [55]. And as stated in Section 2.1.1 it is essential for the success of solid state synthesis that the precursor powders are of a small size and uniformly mixed. The better results obtained in this work suggest that ball milling was more effective than planetary milling in fulfilling these criteria. For the LSFAl-SP powder however, the XRD-pattern did show one small secondary phase peak around 2θ = 25. The peak did not give a good match with the previously reported secondary phases in the synthesis of LSFAl ($\mathrm{SrAl_2O_4}$ and $\mathrm{(LaSr)_2FeO_4}$ [20]), nor other related compositions. Because the powder was not synthesized by the author it is difficult to determine other possible origins of the secondary phase. However, based on the relative intensity of the peaks the amount of secondary phase present appears to be limited.

Characterization of the powders clearly reveals the great difference in quality between the powders synthesized by spray pyrolysis and those synthesized by solid state reaction. The SP-powder has a smaller particle size and a more narrow particle size distribution, the morphology is spherical and after milling the degree of agglomeration is very low. For both of the SSR-powders, the calculated average particle size from the measured BET surface area differs from the results obtained by laser diffraction. The reason for this discrepancy is found by inspecting the SEM images; it is evident from these that the assumption of equally sized, spherical particles is invalid. For the SP-powders however, the particle size calculated from BET is in better agreement with the other results, i.e. laser diffraction and SEM.

Due to the larger surface area of the SP powders, the driving force for sintering will be greater compared to the SSR powder. This is confirmed by comparing the DIL-analysis for the two LSFAl powders (Figure 4.11 and 4.15). The onset of densification was found to be at a temperature 150 °C lower for the SP powder compared to the SS powder, while the maximum from the derivative curve is found at a temperature 320°C lower. It is important to realize that the DIL analysis were carried out on pressed pellets of the powders and that the behavior during sintering may change with a change in the method of green forming. It should also be noted that the analysis for the LSFTa-SS powder was carried out on the as-synthesized powder, while the powder in the tape casting slip is considerably broken down during the procedure of dispersion milling. Even so, the differences in the dilatometry analysis results of the SP and SSR powders will be reflected in the behavior during co-sintering and the consequence of this will be discussed in further detail below.

5.2 Determining the optimum amount of dispersant for LSFTa

The XRD patterns of LSFTa exposed to pH 4.5 to 10.7 did not detect any changes compared to the parent structure. This does not necessarily mean that the powder did not dissolve or decompose, as the degree of change taken place could have been below the detection limit of the diffractometer ($\sim$ 2 %) or of a type

that did not affect the structure. However, for simplicity it will be assumed in the following that the powder did not dissolve or decompose during the course of the zeta potential measurements. All measured changes in zeta potential are thus solely due to adsorption of water related species on the oxide surface or due to dissociation of the dispersant. The results given in Figure 4.17 showed that the isoelectric point (IEP) for pure LSFTa powder in distilled water was located at pH 6.7. Assuming there are no adsorbed ions on the oxide surface other than water related species, the IEP can be taken as point of zero charge (PZC) [3] at which the number of positive and negative sites on the oxide surface are equal. A negative zeta potential measured above the IEP can then be interpreted as the negatively charged surface sites being in surplus. This is in agreement with what can be expected from theory: at high pH values the surface will be covered with $-O^-$ groups giving a negative surface charge, while at low pH values $-OH^+$ groups on the surface will result in a positive charge [32]. The results of the zeta potential measurements can be used as an aid to explain the problems with obtaining a homogeneous and defect free tape in previous work where Poly(vinylpyrrolidone) (PVP) was used as the dispersant for LSFTa in the tape casting slip [16]. As stated in Section 2.1.3, PVP is a basic polymer that will adsorb most strongly onto the surface of acidic powders like carbon black. The measured IEP of LSFTa indicates that the surface character of this powder is mostly basic [29] and it can thus not be expected that PVP will adsorb strongly onto the surface. Any stabilizing effect achieved must then primarily have been due to a depletion mechanism (ref. Figure 2.3).

Darvan CN is a dispersant reported to have good abilities of dispersing basic powders [56, 34]. As stated in Section 2.1.2, the functional group of Darvan CN, COOH will dissociate to COO^- as the pH increases, giving a greater electrostatic repulsion. However, for the dispersant to be attached to the LSFTa powder surface by simple positive-negative interactions, the zeta potential results show that the pH ideally should be as low as possible. There is thus a compromise between the amount of polyelectrolyte attached to the particle surface and the amount of polyelectrolyte that is dissociated. It could be expected that this compromise was found somewhere around neutral conditions, but as the results in

[3] This assumption requires the oxide powder to be 100 % pure, which is unlikely to be the case here as the powder was not prepared and handled in a clean room. However, in most practical cases the PZC does not deviate much from the IEP and the approximation is thus considered to be reasonable.

Figure 4.17 revealed, the highest value of the zeta potential, corresponding to the highest degree of stabilization, is found above pH 10 for all investigated amounts of Darvan CN. This indicates that the interaction between Darvan CN and the LSFTa powder takes place in the form of adsorption rather than coulombic attraction. The increase in zeta potential at increasing pH is then simply explained by an increasing degree of dispersant dissociation. From a practical point of view it is encouraging that the results show that the highest absolute values of zeta potential are found for high pH values as this does not make it necessary to adjust the pH of the tape casting slip (the pH of pure LSFTa in water was measured to be $\sim$ 10.5). The observed overall decrease in zeta potential absolute value from 0.68 wt.% to 0.83 wt.% addition of Darvan CN may be attributed to a modification of the double layer structure. An increase in the concentration of counter-ions (in this case NH_4^+) leads to a neutralization of the diffuse layer and a compression of the double layer [32]. The high standard deviation for the results of the suspension containing 0.47 wt.% Darvan CN could be an effect of particle settling during the measurements, which was observed after inspecting the capillary cell. The settling may have been due to poor dispersion of the suspension or if the particle size distribution was very different compared to the other suspensions. This is not considered to be unlikely because of the wide particle size distribution of the powder it self. A lower standard deviation may have been achieved if the experiment was repeated with a new suspension, but because the overall results of the 0.47 wt.% Darvan CN sample did not seem promising compared to the other concentrations, this was not done.

At this point it is important to comment some of the uncertainties associated with the zeta potential results. The first is, as already mentioned above, the wide particle size distribution of the LSFTa-SS powder. Due to the very small amount of powder used for preparing each of the suspensions for the zeta potential measurement (< 0.2 g) it is considered likely that the particle size distribution in the different test-solutions was not equal. A better way to prepare the samples would have been to mill the powder in higher concentrations with the different amounts of Darvan CN and subsequently dilute to the solid loading suitable for the zeta potential measurements. This procedure would have made the test-solutions more similar to the situation in the tape casting slip. The second possible error is in the use of the autotitrator to adjust the pH while executing the measurements. Because the given time to stabilize the test-solution after each addition of acid and base was very short (< 5 min), there is a chance that the surface reactions did

not reach equilibrium before a measurement point was recorded. Again, it would have been more accurate if the pH of the test-solutions was adjusted in advanced and left for at least 24 hours to stabilize before performing the measurements. The final uncertainty when using the zeta potential results for determining the optimum amount of dispersant is the low solid loading in the samples compared to the desired solid loading in the tape casting slip (0.05 vol.% vs. 15 vol.%).

Due to the uncertainties listed above it was necessary to confirm the zeta potential results by investigating the rheology of higher solid loading suspensions. The shear stress vs. shear rate curves in Figure 4.20 showed the formation of a positive hysteresis between the upward and downward curve segments for all dispersant quantities. This is characterized as thixotropic behavior and involves an increase of the viscosity over time when the suspension is at rest, which could be an effect of flocculation if the suspension was not fully stabilized [28]. The thixotropic behavior has in literature also been explained by the formation of short-range ordering in the dispersant's polymer network [29]. It is believed that the network ordering creates a glass matrix-like structure over time that makes the suspension more resistant against shear. In any case the thixotropic behavior is not desired, but is a problem that can be avoided by storing the suspensions under continuous shear. The results of the viscosity measurements given in Figure 4.21 showed that a first possible minima in viscosity is found at 0.4 wt.% Darvan CN, but that the viscosity is even lower at 0.6 wt.% of Darvan CN. Because the zeta potential measurements also pointed towards $\sim$ 0.6 wt.% being the optimum, 1.58 $\mathrm{mg/m^2}$ dispersant per surface area of LSFTa is taken as the value where complete coverage of the particles is achieved. Although the particle size distribution of the as-synthesized LSFTa-SS powder was initially wide with a significant portion of particles above 10 μm, milling of the powder together with Darvan CN proved to be successful in reducing the particle size considerably down to a more narrow range of 0.3–3 μm. Some portion of larger particles around 10–20 μm are still present, but this type of bimodal size distribution is just considered as an advantage for tape casting slips because it leads to a lower viscosity compared to a more narrow distribution [57].

5.3 Tape casting

The main difference in the two LSFTa tape casting slip prepared was the amount of powder relative to solvent, i.e. the solid loading. As could be seen in Figure 4.24, the slip with 15.8 vol.% solid loading had a lower viscosity than the slip with 16.7 vol.% solid loading, as is also expected because of the less amount of particle–particle interactions. Due to the addition of binder, the viscosity is higher compared to the suspension containing only the powder and dispersant in water, but the measured viscosity of 2000-3000 cP is still within the range of viscosity values reported to be suitable for tape casting in literature (500-6000 cP) [27]. For both of the slips the viscosity was seen to decrease with increasing shear rate, which is a characteristic of pseudoplastic slips and a desired property for tape casting slips. This property means that the slip will have a lower viscosity under the shear of the doctor blade and a higher viscosity after being cast on the carrier film; allowing for the casting of thicker tapes without the risk of lateral spreading [27]. As could be seen in Figure 4.22, there was a considerable difference in quality of the two LSFTa tapes casted. The slip with the highest solid loading resulted in a tape that cracked up during drying and was more fragile than the tape casted from the slip with the lower solid loading. A too high solid loading is known to prevent proper dissolution of the binder [26], which could explain the observed results. A solid loading of 15.8 vol.% powder in the slip is therefor considered the optimum to produce a thick tape while still allowing for proper mixing of the organic additives.

The accepted "standard" way of preparing tape casting slips is following a procedure similar to that given in the flow chart of Figure 3.1 and used in preparation of the LSFTa tapes, i.e. dispersion milling of the powder before introducing the binder and other additives [27]. This ensures complete coverage of the particles by the dispersant and aids in avoiding a possible competitive adsorption of binder with an accompanying increase in viscosity [26]. However, an attempt to prepare the LSFAl tape casting slip following this procedure resulted in a slip that coagulated and became almost foam-like. These observations give reasons to believe that some kind of unwanted reaction takes place between the LSFAl powder and the PVP dispersant. Because the process of dispersion milling breaks down the powder to expose a larger surface area and brings the powder into closer contact with the dispersant, there is a larger probability for the possible reaction to take

place compared to when the alternative tape casting procedure is followed. Further on, if it can be assumed that the surface properties of the LSFTa and LSFAl powders are similar, there are additional reasons to believe that PVP is unsuited as a dispersant for LSFAl. The tape made following the alternative procedure was however found to be of overall good quality, the only defects being evenly distributed pin-holes in the dried tape. These were created due to improper de-airing of the slip, which most likely is a consequence of too high slip viscosity. Because the tape was indented for the porous support and several layers were laminated together, the pin-holes are not considered to be a major problem.

5.4 LSFAl secondary phases

The secondary phases observed in all SEM images of the LSFAl membranes were found to be enriched with Al compared to the main composition. Unfortunately, the EDS results cannot be used directly to determine the composition of the secondary phase since the interaction volume is similar to the thickness of the membrane layer [58]. It was not succeeded to determine the composition from the XRD-patter either and as clarified in Figure 4.42 the peaks did not match with those previously reported to be present in the synthesis of LSFAl [20]. Because the secondary peaks of the diffractogram were located at different 2θ values compared to that found in the pattern of the as-received LSFAl-SP powder, there was a suspicion that an impurity had been introduced during processing. This suspicion is strengthened by the fact that the SEM BSE image of a pressed and sintered pellet of the powder did not show the presence of any secondary phases (Figure 4.43). Based on the EDS-results showing an enrichment of mainly Al, a plausible impurity could be Al_2O_3. Al_2O_3 is used as a detergent for cleaning the YSZ-balls in between use and it could be the case that the balls were not properly rinsed after this cleaning procedure. Since the the powder is heated up to 1300°C after the possible introduction of the impurity, the cations would have sufficient mobility to mix and disturb the stoichiometry of the parent structure. Whether or not this impurity affected the properties of the membrane is not possible to determine since it was not succeded to measure the oxygen permeation flux of the LSFAl asymmetric membrane.

5.5 Strength of LSFAl porous support

The characteristic fracture strength value of the porous LSFAl supports was found to be 10.7±0.5 MPa. The SEM images of the fracture surface cross sections revealed pore cluster in all of the specimens and in some cases very larger pores that can be attributed to poor lamination. The pore clusters and areas with de-lamination will act as stress concentrators, a single, ideally spherical pore will for instance increase the local stress by a factor of three [59]. From inspection of the fracture surfaces it is therefor concluded that the volume defects are the typical origins for fracture of the specimens. The Weibull modulus of 5.9±1.8 indicates a relatively low material reliability and is usually connected to a large size variation of the volume defects and an inhomogeneous microstructure [24]. The large standard deviation of the Weibull modulus is a consequence of the limited number of available specimens. It should also be noted that four of the specimens tested were not completely flat, as is a requirement in the ball-on-ring testing procedure; this contributes to lower the reliability of the results. Since all of the specimens were prepared from the same tape following the same procedure, it is difficult to be sure of what the origin of this production defect was, but a possible explanation could be found in the lamination step, where water was manually dispersed on the tapes using an air brusher before pressing them together. A slightly increased water content in some of the laminated stacks could have lead to the curling of the specimen during binder burn-out.

Considering the reported characteristic strength of LSCF with 46 % porosity (18±2 MPa, Table 2.1), the characteristic strength of the LSFAl porous support is found to be very promising. It should be noted that the reported strength values are for the porous support alone and that the strength for the asymmetric membrane can be expected to be higher. It should also be noted that a porosity of $\sim$ 64 % as in the case of the supports tested here, is probably way above what is required for the support not to limit the overall oxygen flux across the asymmetric membrane. Previous work on LSFTa supports [16], indicates that a porosity as low as 35–40 % should be sufficient. Decreasing the porosity will naturally increase the strength and provide better structural support for the dense membrane.

5.6 Dip coating and sintering of asymmetric membranes

Out of the different procedures for dip coating that were investigated the best results were achieved after two dip coating cycles when using the LSFTa support pre-sintered at 1190°C and the LSFAl supports pre-sintered at 1200°C and 1250°C. However, the obtained thicknesses of the dense layers were considerably less than those reported by Wagner [15] and Gurauskis et al. [13]. For the LSFTa composition a possible explanation to why the thickness was so much lower than for the previous reported work (6–7 μm after two dip coating cycles vs. 15 μm after a single dip coating cycle), could be that the dip coating suspension was not optimized. The particle size distribution in Figure 4.25 showed a wide range of sizes with a considerable amount being above 1 μm, while inspecting the SEM-image of the sintered asymmetric membrane top surface shows that most of the grains in the functional layer are in the sub-micrometer range. This means that the larger particles measured by laser diffraction must have been agglomerates that were formed as a consequence of the dispersion not being stable. The presence of agglomerates in the suspension could have hindered an even deposition of the dense layer. The lower stability of the dip coating suspension in this work is probably because the suspension was prepared on a wt.% basis when following the recipe provided by Gurauskis et al. [13]. It was thus not taken into account that the surface areas of the two powder batches used were different (13.2 m^2/g vs. 18.0 m^2/g).

For the LSFAl composition, the main problem was the presence of pores in the top surface even after four repeated dip coating cycles. As seen in Figure 4.35d these pores are located both at the grain boundaries and in the middle of some grains. Extensive grain growth as a consequence of the sintering temperature being too high could serve as a potential explanation for this observation. As can be seen from the DIL-analysis of the LSFAl-SP powder (Figure 4.15), there is no further densification of the LSFAl-SP powder measured above 1250°C; increasing the sintering temperature for the asymmetric membrane above this level will thus only act to increase the driving force for grain growth. Too rapid grain growth is known to lead to the entrapment of pores in the middle of grains, making it impossible to eliminate them at a later stage [40]. The elevated sin-

tering temperature for the final heat-treatment was chosen because of the low degree of densification of the porous supports at lower temperatures. As shown in Figure 4.33, the LSFAl support pre-sintered at 1200°C cracked repeatedly during the first dip coating cycle such that a specimen large enough to be tested in the oxygen flux furnace could not be produced. Due to the limited amount of densification taking place at this temperature the strength of the support can be expected to be very low. When being submersed in the dip coating suspension, the supports are subjected to a stress from the latex constraining them to the glass strip and from the suspension liquid filling up the pores. It is believed that this stress is what caused the cracking of the support. Another issue that needs to be commented is the low porosity of the specimen pre-sintered at 1250°C compared to those sintered at higher and lower temperatures (see Table 4.1). This indicates that some of the dip coating suspension may have gone into the support and thereby reduced it's porosity. Since all the supports were dip coated the same way, there is no clear explanation to why this has only happened to one of the specimens.

Based on the overall observations made during the different dip coating trials, three factors are believed be important for the membrane layer formation. These will be related to the observed results and discussed in the following.

(1) **Pore channel radius**. As stated in Section 2.1.4, pore channel radius determines the capillary pressure. Although the pores in the produced supports clearly are not circular, equation 5 underlines the importance of the size; i.e. more narrow pores result in a larger capillary pressure. SEM-images of the LSFAl supports revealed that for all the temperatures investigated, the resulting pores were very large. The capillary pressure experienced during the first dip coating cycle is therefor expected to have been very low. During the second and following dip coatings there is however believed to be an increasing contribution from capillary pressure due to the formation of a new surface layer with smaller pores. The consequence of this is that the layer growth will be faster at these remaining pores than at the rest of the surface. This leads to an gradual smoothening of the surface and has previously been described as a "self-repairing" mechanism of the dip coating procedure [60, 61]. A smoothing effect can indeed be observed for the LSFAl support initially calcined at 1250°C (comparing Figure 4.35a and 4.35b). It was also observed for dip coating of the LSFTa porous support where the second dip coating cycle was successful in almost completely covering up

the surface pores. The few remaining pores that were visible are believed to be created by the presence of impurities or dust on the surface.

(2) **Pore size vs. particle size**. As also mentioned in Section 2.1.4, the formation of a cake layer will depend on the size of the surface pores relative to the size of the particles in the dip coating suspension. When the surface pores are much larger than the particles, as is the case here, there is a risk of the support becoming saturated with the dispersing liquid before any considerable cake formation takes place. The consequence of this is the same as above, the support will need to be coated several times before all the pores are covered up. The effect of surface pore size can clearly be seen by comparing the two LSFAl supports pre-sintered at 1300°C, where the top surface for one of the specimens was polished before dip coating (Figure 4.31c and 4.31d). Since the pre-sintering temperature was the same, the total porosity and the size of the pore channels leading up to the surface can be assumed to be approximately the same, making the surface structure the only differentiating factor. After one dip coating cycle, the top layer of the unpolished specimen is seen to be generally more smooth and covered by a greater amount of dense layer (comparing Figure 4.36a and 4.37).

(3) **Support shrinkage**. The importance of avoiding discordance in the shrinkage of the support and membrane layers has previously been discussed by Jin et al. [8]. When the supports are sintered prior to dip coating, some or all of the driving force for shrinkage available for later heat-treatments is lost. If the support is not allowed to shrink together with the membrane layer it might be difficult to achieve full densification and could further on increase the risk of producing defects like cracks. The effect of support pre-sintering temperature can be seen by comparing the two extremes investigated for the LSFAl material, i.e. 1200°C and 1300°C. From SEM images of the top surfaces the result of dip coating might appear to be similar, but a distinction can be made by comparing the cross sections (ref. Figure 4.38). In the membrane layer of the support sintered at 1300°C, the particles deposited during dip coating appear to have coarsened or agglomerated into larger units, while for the support sintered at 1200°C the membrane layer is seen to be smooth and homogeneous. The observation is believed to be an effect of the support pre-sintered at 1300°C not being able to shrink together with the dense layer. Because the particles that are deposited during dip coating are constricted to the support, densification is only possible in the direction perpendicular to the support surface, thereby promoting the formation

of the observed "agglomerates" in the top surface.

It should be emphasized that although the discussion above treats the three different factors as separate contributions, they will in practice affect the results of dip coating simultaneously. There is thus an obvious mismatch between the optimum support pre–sintering temperature to give the smallest pores and the optimum temperature to give the largest "remaining driving force" for later shrinkage. The easiest way to achieve a compromise is if the support and membrane layers have similar shrinkage properties and the porosity is controlled by the addition of pore formers. This is the case for the asymmetric membrane of the LSFTa composition; comparing the particle size distributions of the powder in the support and membrane layers (Figure 4.19 and 4.25, respectively) it is seen that these are quite similar. The resulting porosity ($\sim$ 38 % open porosity) is also close to the amount of pore former added to the tape casting slip (40 vol.%). While for the LSFAl composition (Figure 4.10 and 4.32) there is a large mismatch between the average particle sizes and thus a larger discordance in sintering behavior. The resulting porosity in the support is also considerably larger than the amount of pore former added to the tape casting slip (up to 65 % open porosity vs. 40 vol.% pore former). The shrinkage mismatch between the membrane and support layers could also explain the better results obtained in previously reported work by Wagner and Gurauskis et al. In these works spray pyrolysis powder was used for both the membrane and support layers of the asymmetric membrane [15, 13]. From a practical application point-of-view, the membrane layer should ideally be thicker than what was achieved here. Recent work by Lohne [62] suggests that the critical thickness of both LSFTa and LSFAl materials is in the range of 100–150 μm (depending on temperature and atmosphere). Although the contribution of bulk diffusion is still present down to about 1/10 of the critical thickness, the oxygen permeation flux increase when reducing the thickness below this level is in many cases not enough to make up for the loss in strength and the increased risk of gas leakages and kinetic demixing associated with thin layers [63]. Besides, the oxygen permeation flux of $\sim$ 20 μm thick LSFAl and LSFTa membranes is reported to be very promising (ref. Section 2.3) and further improvements to the oxygen permeation flux could rather be made by surface structuring [19] than reducing the thickness further below 20 μm.

Before the discussion about dip coating is completed, some general comments

about the experimental procedure will be made. First of all, the dip coating in this work was performed manually, which leads to a very limited control of withdrawal speed from the suspension. Due to the extremely low solid loading in the suspension (0.5 vol.%) it is however believed that the coating mostly was promoted by the capillary pressure mechanism, making the withdrawal speed less influential. Still, the reproducibility of the work would have been better if an accurate withdrawal speed could be stated. The second issue is the SEM-images of the asymmetric membrane cross sections, which are taken of the fracture surface. Because ceramic material in general fail along their weakest line, the images may not give a 100 % correct representation of the cross sections, especially in the porous support layer. A better way to make the images would have been to cast the specimens in epoxy and reveal the cross sections by polishing. The reason why this was not done was because it was desired to use the specimens for flux-characterization.

Chapter 6

Further work

To improve the density and thickness of the functional membrane layer, the following is suggested:

- **Decrease the particle size of the solid state reaction powder**. As shown for the LSFTa-composition, the particle size of the solid state reaction powder can be considerably reduced by milling with an appropriate dispersant. Due to the reaction between LSFAl and PVP the same could unfortunately not be done for this composition. Further work should therefor include an investigation of a new dispersant for LSFAl. Darvan CN could be a suitable choice considering the good results obtained for the LSFTa composition.
- **Dip coat the supports with suspensions of increasingly higher solid loading**. Dip coating the supports with a higher solid loading suspension the first time was seen to create an un-even surface with areas of coated and uncoated support and surface cracks with repeating dip coating (see Figure 4.39). However, if the support is "prepped" by dip coating with a lower solid loading suspension the first time, the succeeding dip coating with a higher solid loading might aid in creating a thicker membrane layer.

If the above mentioned suggestions fail, alternative procedures for producing the asymmetric membrane need to be considered. As mentioned several times, using spray pyrolysis powder in both support and membrane layers has given good results previously [13, 15], but this would naturally increase the cost of the membrane. An alternative approach could be direct dip coating of the green porous support as suggested by Jin et al. [8]. In this method, a high solid loading suspension (10–15 vol.%) is employed to make use of the film-coating mechanism. Another alternative is to tape cast the functional membrane layer and laminate with the porous support before co-sintering, as done by Fontaine et al. [64]. It

is however emphasized that a more similar densification behavior in the support and membrane layers will be of importance for the success of these alternative procedures as well.

Chapter 7

Conclusions

- Coarse $La_{0.2}Sr_{0.8}Fe_{0.8}Ta_{0.2}O_{3-\delta}$ (LSFTa) and $La_{0.2}Sr_{0.8}Fe_{0.8}Al_{0.2}O_{3-\delta}$ (LSFAl) powders were successfully synthesized by solid state reaction, while sub-micrometer sized LSFTa powder was made by spray pyrolysis. The powders were characterized in terms of particle size, surface area, morphology and shrinkage behavior.

- The optimum amount of Darvan CN to disperse LSFTa in an aqueous suspension was investigated by measuring the zeta potential as a function of pH and by characterizing the rheology of suspensions containing different amounts of dispersant. Scaled to the surface area of the powder 1.58 $\mathrm{mg/m^2}$ was determined to be the optimum. The particle size of the solid state synthesized powder could be considerably reduced by milling with this dispersant.

- It was not possible to produce a LSFAl tape casting slip following the standard procedure of dispersion milling the powder before introducing the other additives. Based on the observations made it is believed that some kind of unfavorable reaction takes place between PVP and the LSFAl powder, making this an unsuitable dispersant for the powder.

- Supports pre-sintered at various temperatures were dip coated with an ethanol-based suspension to produce a dense functional layer. In general, the best result were obtained when the support was sintered at the lowest possible temperature before it was dip coated. The most promising results were achieved for the LSFTa composition, where dip coating twice and final sintering at 1230°C resulted in a 6–7 μm thick and dense functional layer and a support with 38 % open porosity. Improvements for the dip coating procedure are suggested in this report.

- The biaxial fracture strength of highly porous LSFAl supports was determined by the the ball-on-ring testing procedure. Testing of 11 specimens resulted in a characteristic strength equal to 10.7$\pm$0.5 MPa and a Weibull modulus equal to 5.9$\pm$1.8 MPa.

References

[1] S.M. Hashim, A.R. Mohamed, and S. Bhatia. Current status of ceramic-based membranes for oxygen separation from air. *Advances in colloid and interface science*, 160(1):88–100, 2010.

[2] J. Sunarso, S. Baumann, JM Serra, WA Meulenberg, S. Liu, YS Lin, and JC Diniz da Costa. Mixed ionic-electronic conducting (MIEC) ceramic-based membranes for oxygen separation. *Journal of Membrane Science*, 320(1):13–41, 2008.

[3] Stefan Diethelm, Joseph Sfeir, Frank Clemens, and Daniel Favrat. Planar and tubular perovskite-type membrane reactors for the partial oxidation of methane to syngas. *Journal of Solid State Electrochemistry*, 8(9):611–617, 2004.

[4] Henny J.M. Bouwmeester. Dense ceramic membranes for methane conversion. *Catalysis Today*, 82:141 – 150, 2003. 5th International Conference on Catalysis in Membrane Reactors.

[5] PJ Gellings and HJM Bouwmeester. *The CRC Handbook of Solid State Electrochemistry*. CRC Press, 1997.

[6] HJM Bouwmeester, H. Kruidhof, and AJ Burggraaf. Importance of the surface exchange kinetics as rate limiting step in oxygen permeation through mixed-conducting oxides. *Solid State Ionics*, 72:185–194, 1994.

[7] Gregory Etchegoyen, Thierry Chartier, and Pascal Del-Gallo. An architectural approach to the oxygen permeability of a $\mathrm{La_{0.6}Sr_{0.4}Fe_{0.9}Ga_{0.1}O3_{3-\delta}}$ perovskite membrane. *Journal of the European Ceramic Society*, 26(13):2807–2815, 2006.

[8] Wanqin Jin, Shiguang Li, Pei Huang, Nanping Xu, and Jun Shi. Preparation of an asymmetric perovskite-type membrane and its oxygen permeability. *Journal of Membrane Science*, 185(2):237–243, 2001.

[9] Masayuki Ikeguchi, Kentaro Ishii, Yasushi Sekine, Eiichi Kikuchi, and Masahiko Matsukata. Improving oxygen permeability in $\mathrm{srfeco_{0.5}o_x}$ asymmetric membranes by modifying support-layer porous structure. *Materials Letters*, 59(11):1356 – 1360, 2005.

[10] Y. Teraoka, H.M. Zhang, K. Okamoto, and N. Yamazoe. Mixed ionic-electronic conductivity of $\mathrm{La_{1-x}Sr_xCo_{1-y}Fe_yO_{3-\delta}}$ perovskite-type oxides. *Materials Research Bulletin*, 23(1):51 – 58, 1988.

[11] Ørjan Fossmark Lohne, Jonas Gurauskis, Tan Nhut Phung, Mari-Ann Einarsrud, Tor Grande, Henny J.M. Bouwmeester, and Kjell Wiik. Effect of B-site substitution on the stability of $\mathrm{La_{0.2}Sr_{0.8}Fe_{0.8}B_{0.2}O_{3-\delta}}$, B=Al, Ga, Cr, Ti, Ta, Nb. *Solid State Ionics*, 225(0):186 – 189, 2012.

[12] Peter Vang Hendriksen, Peter Halvor Larsen, Mogens Mogensen, Finn Willy Poulsen, and Kjell Wiik. Prospects and problems of dense oxygen permeable membranes. *Catalysis Today*, 56(1-3):283–295, 2000.

[13] J. Gurauskis, Ø.F. Lohne, H.L. Lein, and K. Wiik. Processing of thin film ceramic membranes for oxygen separation. *Journal of the European Ceramic Society*, 32(3):649–655, 2011.

[14] J. Gurauskis, Ø.F. Lohne, and K. Wiik. $\mathrm{La_{0.2}Sr_{0.8}Fe_{0.8}Ta_{0.2}O_{3-\delta}}$ based thin film membranes with surface modification for oxygen production. *Solid State Ionics*, 225:703–706, 2012.

[15] Nils Wagner. Permeation and stability properties of asymmetric and disk shaped oxygen permeable membranes intended for syn-gas production. Master's thesis, NTNU, 2012.

[16] Belma Talic. Permeability of optimized LSFTa porous supports for syn-gas production membranes, 2012. Project report, NTNU.

[17] Petter Wibe. Optimization of strength and permeability of tape casted porous $\mathrm{La_{0.2}Sr_{0.8}Fe_{0.8}Ta_{0.2}O_{3-\delta}}$. Master's thesis, NTNU, 2012.

[18] Julia D. Meyer. Processing and mechanical properties of tape casted films with composition $\mathrm{La_{0.2}Sr_{0.8}Fe_{0.8}Ta_{0.2}O_{3-\delta}}$ as membranes for syngas-production. Master's thesis, NTNU, 2011.

[19] Espen Tjønneland Wefring. Nanostructuring of oxygen permeable membranes by chemical etching techniques. Master's thesis, NTNU, 2011.

[20] Dan Stræte Lagergren. Permeation and mechanical properties of porous supports intended for asymmetric membranes based on $La_{0.2}Sr_{0.8}Fe_{0.8}Al_{0.2}O_{3-\delta}$. Master's thesis, NTNU, 2012.

[21] Xiwang Qi, YS Lin, and SL Swartz. Electric transport and oxygen permeation properties of lanthanum cobaltite membranes synthesized by different methods. *Industrial & engineering chemistry research*, 39(3):646–653, 2000.

[22] Gary L. Messing, Shi-Chang Zhang, and Gopal V. Jayanthi. Ceramic powder synthesis by spray pyrolysis. *Journal of the American Ceramic Society*, 76(11):2707–26, 1993.

[23] Lesley E. Smart and Elaine A. Moore. *Solid state chemistry*. CRC Press, Boca Raton, Florida, 3 edition, 2005.

[24] David W Richerson. *Modern Ceramic Engineering*. CRC Press, Boca Raton, Florida, 3 edition, 2006.

[25] Cerpotech AS. Illustration of the spray pyrolysis process, November 2012.

[26] Rodrigo Moreno. The role of slip additives in tape casting technology: Part II-binders and plasticizers. *American Ceramic Society Bulletin*, 71(11):1647–1657, 1992.

[27] Richard E. Mistler and Eric R. Twiname. *Tape Casting, theory and practice*. The American Ceramic Society, Wsterville, Ohio, 1 edition, 2000.

[28] Rodrigo Moreno. The role of slip additives in tape casting technology: Part I-solvents and dispersants. *American Ceramic Society Bulletin*, 71(10):1521–1531, 1992.

[29] Kunio Esumi, Koichi Takamin, Makoto Ono, Takahiro Osada, and Shuji Ichikawa. The interaction of poly(vinyl pyrrolidone) and solid particles in ethanol. *Journal of colloid and interface science*, 161:321–324, 1993.

[30] Kunio Esumi, Kenji Ishizuki, Hidenori Otsuka, Matoko Ono, Shuji Ichikawa, and Chie Yanase. The effect of binary solvents on adsorption of poly(vinylpyrrolidone) on titanium dioxide and graphite particles. *Journal of colloid and interface science*, 178:549–554, 1996.

[31] Kenji Ishiduki and Kunio Esumi. Adsorption characteristics of poly (acrylic acid) and poly(vinyl pyrrolidone) on alumina from their mixtures in aqueous solution. *Journal of colloid and interface science*, 185(1):274–277, 1997.

[32] Daniel J. Shanefield. *Organic Additives and Ceramic Processing*. Kluwer Academic Publishers, 2 edition, 1996.

[33] Bimal P. Singh, Sarama Bhattacharjee, Laxmidhar Besra, and D.K. Sengupta. Electrokinetic and adsorption studies of alumina suspensions using Darvan C as dispersant. *Journal of Colloid and Interface Science*, 289:592–596, 2005.

[34] Joseph Cesarano and Ilhan A. Aksay. Processing of highly concentrated aqueous α-alumina suspensions stabilized with polyelectrolytes. *Journal of the American Ceramic Society*, 71(12):1062–1067, 1988.

[35] B.C. Bonekamp. Chapter 6: Preparation of asymmetric ceramic membrane supports by dip-coating. In A.J. Burggraaf and L. Cot, editors, *Fundamentals of Inorganic Membrane Science and Technology*, volume 4 of *Membrane Science and Technology*, pages 141 – 225. Elsevier, 1996.

[36] Yunfeng Gu and Guangyao Meng. A model for ceramic membrane formation by dip-coating. *Journal of the European Ceramic Society*, 19(11):1961 – 1966, 1999.

[37] Duncan J Shaw and Richard Williams. *Introduction to colloid and surface chemistry*. Butterworth-Heinemann Oxford, 1992.

[38] A.F.M Leenaars and A.J Burggraaf. The preparation and characterization of alumina membranes with ultrafine pores. 2. The formation of supported membranes. *Journal of Colloid and Interface Science*, 105(1):27 – 40, 1985.

[39] Frank M. Tiller and Chun-Dar Tsai. Theory of filtration of ceramics: I, slip casting. *Journal of the American Ceramic Society*, 69(12):882–887, 1986.

[40] J.E. Blendell. Solid-state sintering. In K.H.J. Buschow, editor, *Encyclopedia of materials: Science and Technology*. Elsevier Science Ltd., 2001.

[41] M.N. Rahaman. Kinetics and mechanisms of densification. In Z.Z. Fang, editor, *Sintering of Advanced Ceramics - Fundamentals and Processing*. Woodhead Publishing, 2010.

[42] Stephen F. Corbin and Prasad S. Apte. Engineered porosity via tape casting, lamination and the percolation of pyrolyzable particulates. *Journal of the American Ceramic Society*, 82:1693–1701, 1999.

[43] Waloddi Weibull. A statistical distribution function of wide applicability. *Journal of applied mechanics*, 18(3):293–297, 1951.

[44] Hilde Lea Lein. *Mechanical Properties and Phase Stability of Oxygen Permeable Membranes* $La_{0.5}Sr_{0.5}Fe_{1-x}Co_xO_{3-\delta}$. PhD thesis, Norwegian University of Science and Technology, 2005.

[45] Nina Orlovskaya, Kjersti Kleveland, Tor Grande, and Mari-Ann Einarsrud. Mechanical properties of $\mathrm{LaCoO_3}$ based ceramics. *Journal of the European Ceramic Society*, 20(1):51–56, 2000.

[46] M. Lipinska-Chwalek, J. Malzbender, A. Chanda, S. Baumann, and R.W. Steinbrech. Mechanical characterization of porous $\mathrm{Ba_{0.5}Sr_{0.5}Co_{0.8}Fe_{0.2}O_{3-\delta}}$. *Journal of the European Ceramic Society*, 31(15):2997 – 3002, 2011.

[47] G. Pecanac, S. Foghmoes, M. Lipinska-Chwalek, S. Baumann, T. Beck, and J. Malzbender. Strength degradation and failure limits of dense and porous ceramic membrane materials. *Journal of the European Ceramic Society*, pages –, 2013. article in press.

[48] Andreas Borger, Peter Supancic, and Robert Danzer. The ball on three balls test for strength testing of brittle discs: stress distribution in the disc. *Journal of the European Ceramic Society*, 22:1425–1436, 2002.

[49] Dinesh K Shetty, Alan R Rosenfield, Paula McGuire, GK Bansal, and Winston H Duckworth. Biaxial flexure tests for ceramics. *American Ceramic Society Bulletin*, 59(12), 1980.

[50] Henrik Lund Frandsen. The small displacement elastic solution to the ball-on-ring testing method. *Mechanics of Materials*, 55(0):33 – 40, 2012.

[51] Tommy Mokkelbost, Øystein Andersen, Ruth Astrid Strøm, Kjell Wiik, Tor Grande, and Mari-Ann Einarsrud. High-temperature proton-conducting $\mathrm{LaNbO_4}$-based materials: Powder synthesis by spray pyrolysis. *Journal of the American Ceramic Society*, 90(11):3395–3400, 2007.

[52] S.E. Dann, D.B. Currie, M.T. Weller, M.F. Thomas, and A.D. Al-Rawwas. The effect of oxygen stoichiometry on phase relations and structure in the system $La_{1-x}Sr_xFeO_{3-\delta}$ ($0 \leq x \leq 1, 0 \leq \delta \leq 0.5$). *Journal of Solid State Chemistry*, 109(1):134 – 144, 1994.

[53] Ørjan Fossmark Lohne. Theoretical density of LSFTa2882, calculated from XRD-results using the lattice parameters. PhD student at Norwegian University of Science and Technology. e-mail: orjan.f.lohne@ntnu.no.

[54] T. N. Phung. Theoretical density of LSFAl2882. PhD student at University of Twente. e-mail: t.phungnhuttan@tnw.utwente.nl.

[55] Fred F Lange. Powder processing science and technology for increased reliability. *Journal of the American Ceramic Society*, 72(1):3–15, 1989.

[56] Bimal P Singh, Sarama Bhattacharjee, Laxmidhar Besra, and Dilip K Sengupta. Evaluation of dispersibility of aqueous alumina suspension in presence of Darvan C. *Ceramics international*, 30(6):939–946, 2004.

[57] G.W. Phelps and M.G. McLaren. Particle-size distribution and slip properties. In Onoda and Hench, editors, *Ceramic Processing Before Firing*. John Wiley & Sons, New York, 1978.

[58] Joseph Goldstein, Dale E Newbury, David C Joy, Charles E Lyman, Patrick Echlin, Eric Lifshin, Linda Sawyer, and Joseph R Michael. *Scanning electron microscopy and X-ray microanalysis*. Springer, 2003.

[59] Brian Lawn. *Fracture of brittle solids*. Cambridge university press, 1993.

[60] Jonas Gurauskis. Deposition via dip coating technique of dense yttrium stabilized zirconia layers. *International Journal of Applied Ceramic Technology*, 10(1):79–86, 2013.

[61] Changrong Xia, Shaowu Zha, Weiguang Yang, Ranran Peng, Dingkun Peng, and Guangyao Meng. Preparation of yttria stabilized zirconia membranes on porous substrates by a dip-coating process. *Solid State Ionics*, 133(3):287–294, 2000.

[62] Ørjan Fossmark Lohne. Oral communication about unpublished work. PhD student at NTNU. e-mail: orjan.f.lohne@ntnu.no.

[63] M Martin. Materials in thermodynamic potential gradients. *The Journal of Chemical Thermodynamics*, 35(8):1291–1308, 2003.

[64] M.-L. Fontaine, J.B. Smith, Y. Larring, and R. Bredesen. On the preparation of asymmetric $CaTi_{0.9}Fe_{0.1}O_{3-\delta}$ membranes by tape-casting and co-sintering process. *Journal of Membrane Science*, 326(2):310 – 315, 2009.

Appendix A

Flow charts for making spray pyrolysis precursors

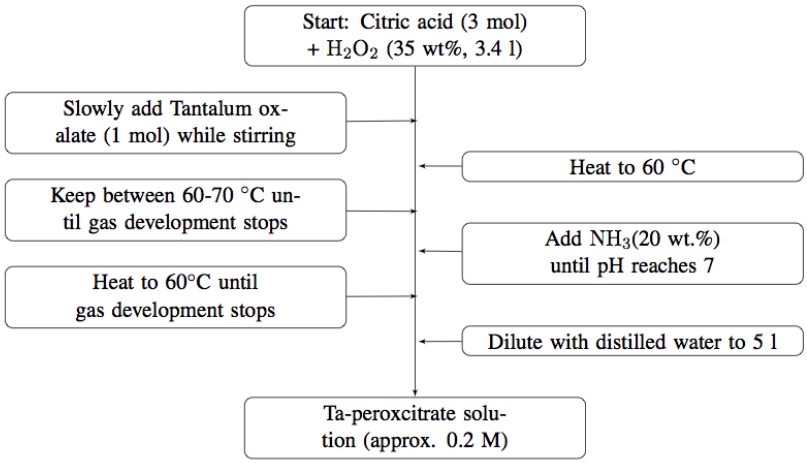

Figure A.1: Flowchart for making Ta-peroxcitrate precursor

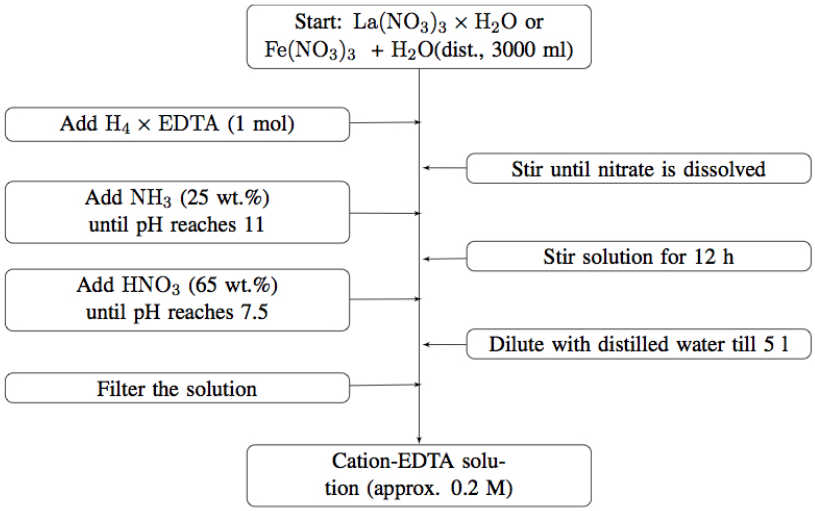

Figure A.2: Flowchart for making cation-EDTA precursors

Appendix B

Standardization of the LSFTa spray pyrolysis precursor solutions

The three precursor solutions for making LSFTa powder by spray pyrolysis were standardized by heating an alumina crucible containing a small amount of the precursor solution at 800°C for 12 hours. During this heat treatment the nitrate solution is oxidized and the amount of cation per gram of precursor solution may be determined by comparing the weight of the crucibles before and after the heat treatment. Four parallels were measured for each of the precursor solutions.

Amount of nitrate, $m_{nitrate}$ is the weight of the precursor solution before heat treatment, amount of oxide, m_{oxide} is the weight of the remainder after the heat treatment. The molar amount of oxide, n_{oxide} is calculated from the amount of oxide times the molar weight of the oxide:

$$n_{oxide} = m_{oxide} \times M_M oxide \tag{B.1}$$

The concentration of the precursor solution in the amount of cation per gram of precursor solution is then found from:

$$Concentration_{precursor} = \frac{f_{oxide/nitrate} * n_{oxide}}{m_{nitrate}} \tag{B.2}$$

where the ration between nitrate and oxide, $f_{oxide/nitrate}$, in all cases is 2.

Table B.1: Standardization of Ta-oxalate

$m_{nitrate}$ [g]	m_{oxide} [g]	n_{oxide} [mol]	Concentration [mol/g]
2.4227	0.0700	0.000162028	1.3376E-04
3.2268	0.0958	0.000216791	1.3437E-04
2.5762	0.0765	0.000173116	1.3440E-04
3.3386	0.0990	0.000223127	1.3367E-04
Concentration (average) = 1.3405×10^{-4}			
Std. deviation = 3.895×10^{-7}			

Table B.2: Standardization of La-EDTA precursor solution

$m_{nitrate}$ [g]	m_{oxide} [g]	n_{oxide} [mol]	Concentration [mol/g]
3.9512	0.1000	0.000297097	0.000150
3.0633	0.0750	0.000230188	0.000150
3.7454	0.0907	0.000278375	0.000149
2.3293	0.0570	0.000176171	0.000151
Concentration (average) = 1.5015×10^{-4}			
Std. deviation = 1.090×10^{-6}			

Table B.3: Standardization of Fe-EDTA precursor solution

$m_{nitrate}$ [g]	m_{oxide} [g]	n_{oxide} [mol]	Concentration [mol/g]
3.6617	0.08	0.000522295	0.000285
2.9534	0.0671	0.000420215	0.000285
3.2927	0.075	0.000469689	0.000285
3.727	0.085	0.000531688	0.000285
Concentration (average) = 2.8511×10^{-4}			
Std. deviation = 3.656×10^{-7}			

Appendix C

Thermogravimetric analysis of LSFTa spray pyrolysis powder

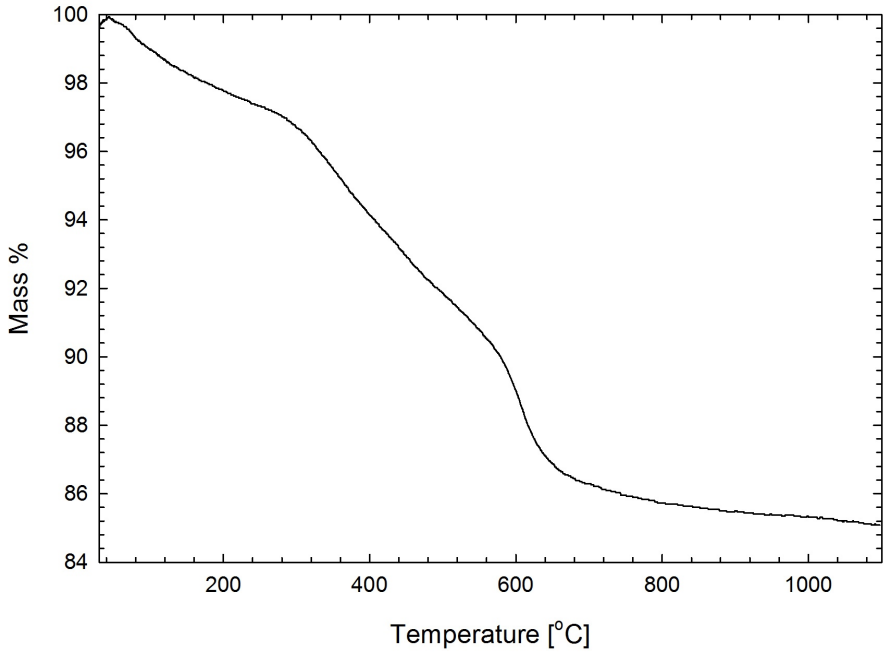

Figure C.1: Thermogravimetric analysis of "raw" LSFTa spray pyrolysis powder.

Appendix D

BET-results

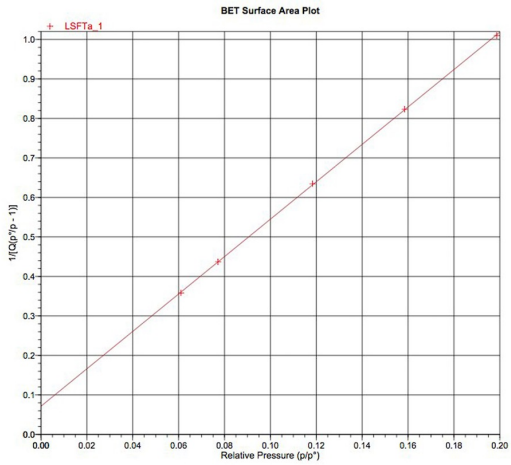

BET Surface Area Report

BET Surface Area: 0.9057 ± 0.0040 m²/g
Slope: 4.734906 ± 0.021181 g/cm³ STP
Y-Intercept: 0.071447 ± 0.002814 g/cm³ STP
C: 67.271601
Qm: 0.2081 cm³/g STP
Correlation Coefficient: 0.9999700
Molecular Cross-Sectional Area: 0.1620 nm²

Relative Pressure (p/p°)	Quantity Adsorbed (cm³/g STP)	1/[Q(p°/p - 1)]
0.060976577	0.1814	0.358052
0.077166627	0.1913	0.437023
0.118342734	0.2115	0.634500
0.158501209	0.2288	0.823157
0.198610965	0.2454	1.009832

Figure D.1: BET-result of solid state synthesized LSFTa powder - sample #1.

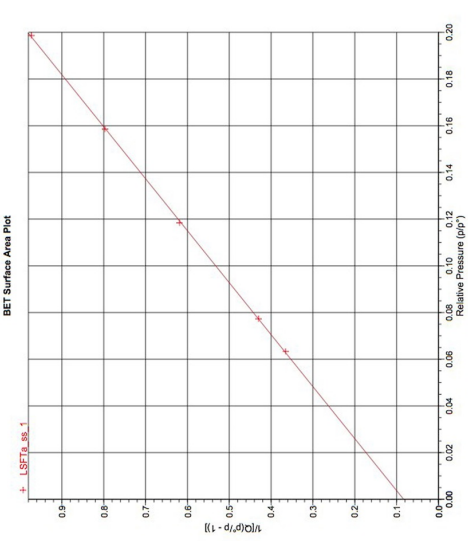

BET Surface Area Report

BET Surface Area: 0.9516 ± 0.0059 m²/g
Slope: 4.491384 ± 0.028084 g/cm³ STP
Y-Intercept: 0.083329 ± 0.003738 g/cm³ STP
C: 54.899420
Qm: 0.2186 cm³/g STP
Correlation Coefficient: 0.9999414
Molecular Cross-Sectional Area: 0.1620 nm²

Relative Pressure (p/p°)	Quantity Adsorbed (cm³/g STP)	1/[Q(p°/p - 1)]
0.063329358	0.1851	0.365323
0.077291990	0.1947	0.430148
0.118372080	0.2170	0.618864
0.158515988	0.2364	0.796754
0.198627796	0.2548	0.972865

Figure D.2: BET-result of solid state synthesized LSFTa powder - sample #2.

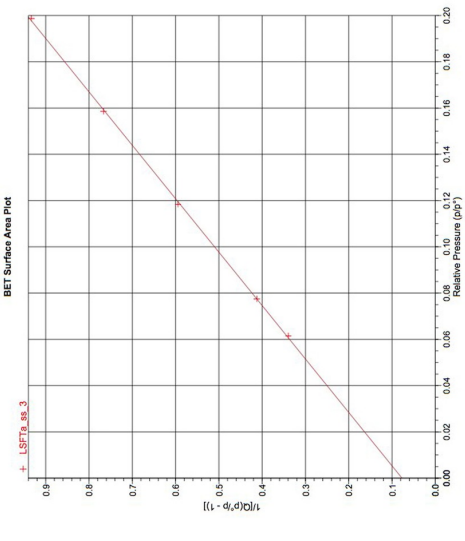

BET Surface Area Report

BET Surface Area: 0.9880 ± 0.0089 m²/g
Slope: 4.328934 ± 0.039460 g/cm³ STP
Y-Intercept: 0.077129 ± 0.005247 g/cm³ STP
C: 57.125599
Qm: 0.2270 cm³/g STP
Correlation Coefficient: 0.9998754
Molecular Cross-Sectional Area: 0.1620 nm²

Relative Pressure (p/p°)	Quantity Adsorbed (cm³/g STP)	1/[Q(p°/p - 1)]
0.061444624	0.1928	0.339517
0.077452018	0.2036	0.412368
0.118388347	0.2259	0.594436
0.158548650	0.2459	0.766311
0.198671490	0.2657	0.933168

Figure D.3: BET-result of solid state synthesized LSFTa powder - sample #3.

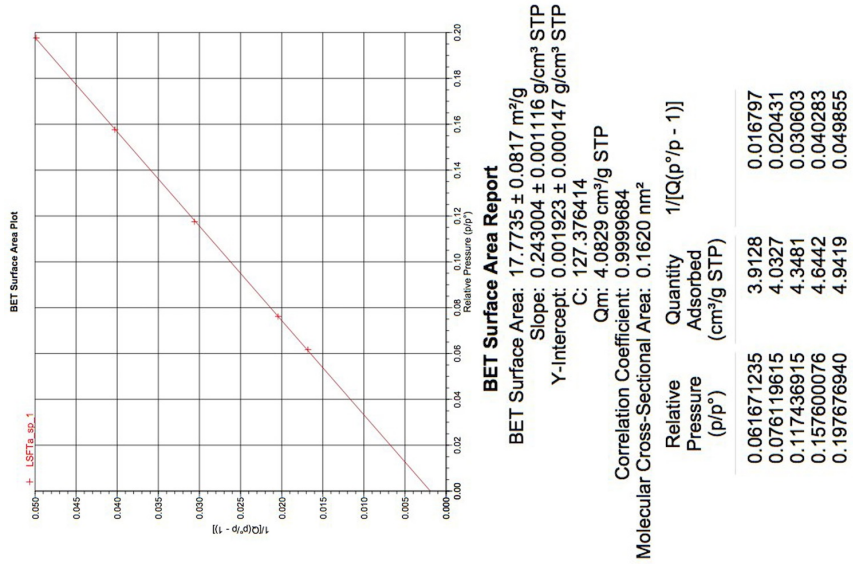

BET Surface Area Report

BET Surface Area: 17.7735 ± 0.0817 m²/g
Slope: 0.243004 ± 0.001116 g/cm³ STP
Y-Intercept: 0.001923 ± 0.000147 g/cm³ STP
C: 127.376414
Qm: 4.0829 cm³/g STP
Correlation Coefficient: 0.9999684
Molecular Cross-Sectional Area: 0.1620 nm²

Relative Pressure (p/p°)	Quantity Adsorbed (cm³/g STP)	1/[Q(p°/p - 1)]
0.061671235	3.9128	0.016797
0.076119615	4.0327	0.020431
0.117436915	4.3481	0.030603
0.157600076	4.6442	0.040283
0.197676940	4.9419	0.049855

Figure D.4: BET-result of LSFTa powder made by spray pyrolysis - sample #1.

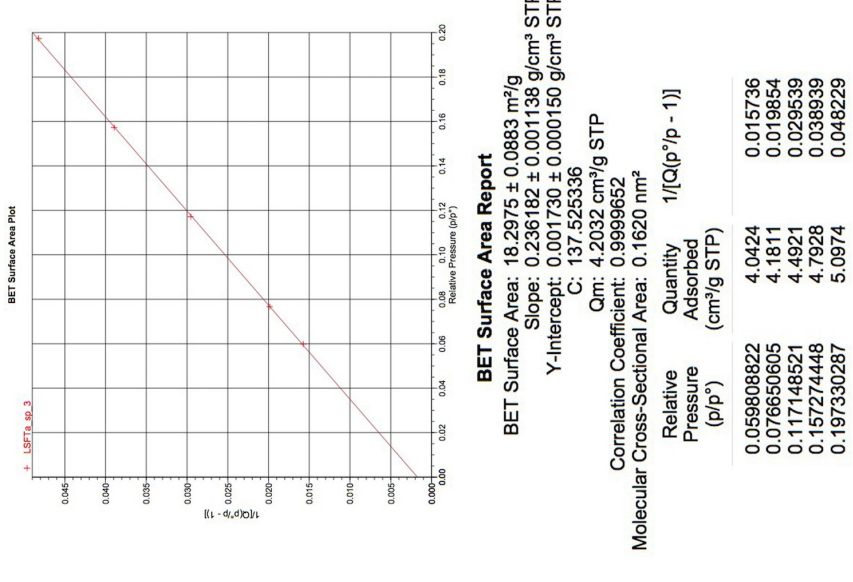

BET Surface Area Report

BET Surface Area: 18.2975 ± 0.0883 m²/g
Slope: 0.236182 ± 0.001138 g/cm³ STP
Y-Intercept: 0.001730 ± 0.000150 g/cm³ STP
C: 137.525336
Qm: 4.2032 cm³/g STP
Correlation Coefficient: 0.9999652
Molecular Cross-Sectional Area: 0.1620 nm²

Relative Pressure (p/p°)	Quantity Adsorbed (cm³/g STP)	1/[Q(p°/p - 1)]
0.059808822	4.0424	0.015736
0.076650605	4.1811	0.019854
0.117148521	4.4921	0.029539
0.157274448	4.7928	0.038939
0.197330287	5.0974	0.048229

Figure D.5: BET-result of LSFTa powder made by spray pyrolysis - sample #2.

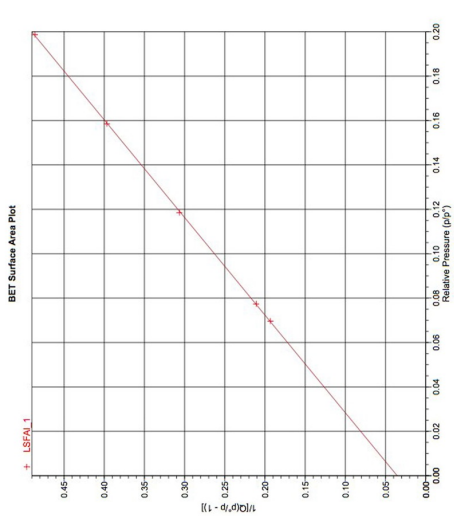

BET Surface Area Report

BET Surface Area: 1.8852 ± 0.0083 m²/g
Slope: 2.273477 ± 0.010032 g/cm³ STP
Y-Intercept: 0.035630 ± 0.001342 g/cm³ STP
C: 64.808838
Qm: 0.4331 cm³/g STP
Correlation Coefficient: 0.9999708
Molecular Cross-Sectional Area: 0.1620 nm²

Relative Pressure (p/p°)	Quantity Adsorbed (cm³/g STP)	1/[Q(p°/p - 1)]
0.069631242	0.3870	0.193371
0.077336763	0.3973	0.210951
0.118463547	0.4387	0.306325
0.158539826	0.4750	0.396657
0.198670254	0.5097	0.486406

Figure D.6: BET-result of solid state synthesized LSFAl powder.

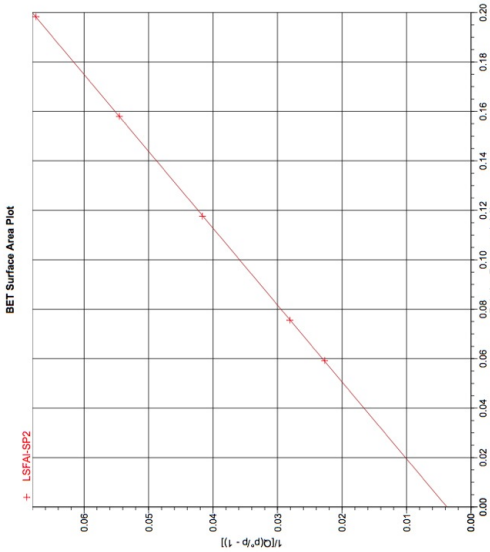

BET Surface Area Report

BET Surface Area: 13.3824 ± 0.0326 m²/g
Slope: 0.321547 ± 0.000785 g/cm³ STP
Y-Intercept: 0.003745 ± 0.000104 g/cm³ STP
C: 86.864848
Qm: 3.0742 cm³/g STP
Correlation Coefficient: 0.9999911
Molecular Cross-Sectional Area: 0.1620 nm²

Relative Pressure (p/p°)	Quantity Adsorbed (cm³/g STP)	1/[Q(p°/p - 1)]
0.059198325	2.7744	0.022680
0.075557114	2.9095	0.028091
0.117605537	3.1992	0.041661
0.158017531	3.4408	0.054544
0.198299487	3.6662	0.067467

Figure D.7: BET-result of LSFAl spray pyrolysis powder after milling 24 hours.

Appendix E

Zeta potential measurement - raw data

The standard deviation is calculated from:

$$\sigma = \sqrt{\frac{1}{N}\sum_{i=1}^{N}(x_i - \mu)^2} \tag{E.1}$$

where N is the number of samples, x_i is the value of the zeta potential and μ is the average zeta potential.

Darvan C - 0					
pH	average	Zeta potential	average	difference	standard deviation
9,83		-19,5		3,121	
9,83	9,83	-16,7	-17,733	1,068	1,255
9,82		-17		0,538	
8,77		-17		0,810	
8,82	8,82	-16,3	-16,100	0,040	0,829
8,87		-15		1,210	
7,48		-16,3		10,890	
7,53	7,53	-10,2	-13,000	7,840	2,515
7,59		-12,5		0,250	
7,01		-5,94		1,488	
7,04	7,05	-3,07	-4,720	2,723	1,210
7,09		-5,15		0,185	
6,06		9,58		0,006	
6,1	6,10	9,72	9,657	0,004	0,058
6,14		9,67		0,000	
5,09		22		0,001	
5,15	5,15	23,3	22,033	1,604	1,021
5,21		20,8		1,521	

Figure E.1: Zeta potential measurement raw data - 0 wt.% Darvan CN

0.2 wt.% Darvan CN					
pH	average	Zeta potential	average	difference	standard deviation
4,19		-19,3		18,490	
4,2	4,20	-13,1	-15,000	3,610	3,047
4,21		-12,6		5,760	
4,97		-13,6		44,001	
4,96	4,96	-23,7	-20,233	12,018	4,692
4,96		-23,4		10,028	
5,92		-25,1		9,201	
5,93	5,93	-29,1	-28,133	0,934	2,191
5,94		-30,2		4,271	
8,73		-30		6,084	
8,56	8,56	-32,8	-32,467	0,111	1,893
8,39		-34,6		4,551	
9,14		-36,4		25,334	
9,09	9,09	-43,2	-41,433	3,121	3,611
9,05		-44,7		10,671	
9,47		-45,8		4,840	
9,45	9,45	-49,3	-48,000	1,690	1,564
9,43		-48,9		0,810	
9,89		-48,5		0,040	
9,88	9,88	-49,1	-48,700	0,160	0,283
9,87		-48,5		0,040	
11		-50,8		0,934	
11	11,00	-52,4	-51,767	0,401	0,694
11		-52,1		0,111	

Figure E.2: Zeta potential measurement raw data - 0.2 wt.% Darvan CN

0.4 wt.% Darvan CN					
pH	average	Zeta potential	average	difference	standard deviation
4,16		-25		0,160	
4,17	4,17	-24,4	-24,600	0,040	0,283
4,17		-24,4		0,040	
5,22		-24,8		4,000	
5,18	5,18	-29,3	-26,800	6,250	1,871
5,15		-26,3		0,250	
6,21		-26,9		6,934	
6,2	6,20	-30,7	-29,533	1,361	1,866
6,2		-31		2,151	
6,81		-31,2		3,361	
6,78	6,78	-33,4	-33,033	0,134	1,372
6,76		-34,5		2,151	
7,97		-36,8		0,871	
7,87	7,87	-37,4	-37,733	0,111	0,929
7,78		-39		1,604	
8,97		-39,7		4,000	
8,92	8,91	-41,7	-41,700	0,000	1,633
8,85		-43,7		4,000	
9,91		-46,2		153,512	
9,89	9,89	-8,03	-33,810	664,608	18,234
9,86		-47,2		179,292	
10,8		-50,8		198,246	
10,8	10,80	-2,06	-36,720	1201,316	24,652
10,8		-57,3		423,536	

Figure E.3: Zeta potential measurement raw data - 0.4 wt.% Darvan CN

0.6 wt.% Darvan CN					
pH	average	Zeta potential	average	difference	standard deviation
6,16		-53,5		0,401	
6,27	6,27	-52,3	-52,867	0,321	0,492
6,38		-52,8		0,004	
6,96		-52,1		0,160	
6,97	6,97	-52,1	-52,500	0,160	0,566
6,98		-53,3		0,640	
7,78		-53,7		0,028	
7,79	7,79	-54,1	-53,867	0,054	0,170
7,81		-53,8		0,004	
8,86		-54,5		0,640	
8,88	8,88	-54,8	-55,300	0,250	0,927
8,89		-56,6		1,690	
9,93		-55,5		6,934	
9,93	9,93	-60,3	-58,133	4,694	1,987
9,93		-58,6		0,218	
11		-60,6		3,484	
11	11,00	-62	-62,467	0,218	1,746
11		-64,8		5,444	

Figure E.4: Zeta potential measurement raw data - 0.6 wt.% Darvan CN

0.8 wt.% Darvan CN					
pH	average	Zeta potential	average	difference	standard deviation
5,9		-35,9		8,410	
5,94	5,94	-37	-38,800	3,240	3,354
5,98		-43,5		22,090	
6,82		-40,6		0,054	
6,8	6,80	-40,1	-40,367	0,071	0,205
6,79		-40,4		0,001	
7,9		-41		1,778	
7,83	7,83	-42,8	-42,333	0,218	0,957
7,76		-43,2		0,751	
8,92		-43,5		1,521	
8,88	8,88	-45	-44,733	0,071	0,918
8,84		-45,7		0,934	
9,87		-48		2,560	
9,85	9,85	-50,9	-49,600	1,690	1,203
9,83		-49,9		0,090	
11		-64,8		13,938	
11	11,00	-72,1	-68,533	12,721	2,983
11		-68,7		0,028	

Figure E.5: Zeta potential measurement raw data - 0.8 wt.% Darvan CN

Appendix F

Determination of porosity by Archimedes' method - raw data

The porosity of a specimen can be determined using the Archimedes method specified in ISO 5017:1998. The bulk density, ρ_b, is calculated from:

$$\rho_b = \frac{m_1}{m_3 - m_2} \times \rho_{liq} \tag{F.1}$$

From this the apparent porosity, π_a, and the true porosity, π_t can be found from:

$$\pi_a = \frac{m_3 - m_1}{m_3 - m_2} \times 100 \tag{F.2}$$

$$\pi_t = \frac{\rho_t - \rho_b}{\rho_t} \times 100 \tag{F.3}$$

In the equations above m_1 is the mass of the dry test piece, m_2 is the mass of the test piece immersed by a liquid, m_3 is the mass of the test piece immersed by a liquid with the surface liquid film removed. ρ_{liq} is the density of the immersion liquid and ρ_t is the true density of the compound. The density of the immersion liquid, iso-propanol, depends on temperature according to:

$$\rho_{liq} = (-0.0009 \times T) + 0.8018 \tag{F.4}$$

Where T is the temperature in °C. Table F.1 gives the measured masses of the samples investigated together with the values calculated from the equations above.

Table F.1: Calculated bulk density and porosity for all samples measured with Archimedes' method. Symbols are explained in the text above. True densities for the two materials are: ρ_{LSFTa} = 6.3g/cm^3 and ρ_{LSFAl} = 5.54g/cm^3.

Sample ID	m_1 [g]	m_2 [g]	m_3 [g]	T [°C]	ρ_b [g/cm^3]	π_a [%]	π_t [%]
Dip coated LSFAl porous supports							
C1200	0.2727	0.2331	0.3382	20.2	2.03	62.3	63.3
C1250	0.7266	0.6218	0.8320	20.,2	2.71	50.1	51.1
C1300	0.8634	0.739	1.0944	20.2	1.90	65.0	65.6
C1300-P	0.4923	0.4207	0.6766	21.0	1.51	72.0	72.8
LSFAl porous supports used for ball-on-ring strength testing							
1	0.1245	0.1066	0.1522	20.4	2.14	60.7	61.4
4	0.4551	0.3892	0.5704	20.4	1.97	63.6	64.5
6	0.3434	0.2937	0.4301	20.5	1.97	63.6	64.4
Dip coated LSFTa porous supports							
C1190	0.8564	0.7469	0.9235	21.0	0.7829	38.0	39.7

Appendix G

Strength measurements - raw data

The strength of the porous support is calculated according to:

$$\sigma_{max} = \frac{3P(1+\nu)}{4\pi t^2}\left[1 + 2ln\left(\frac{a}{b}\right) + \frac{1-\nu}{1+\nu}\left(1 - \frac{b^2}{2a^2}\right)\frac{a^2}{r^2}\right] \tag{G.1}$$

where P is the load[N]; ν is Poisson's ratio; t is the specimen thickness[mm]; a is the radius of the specimen support[mm]; b is the radius of uniform loading (b=t/3) [mm] and r is the specimen radius[mm].

Table G.1 gives the raw-data for the samples tested. Because the samples prepared were not completely flat and uniform, the given thickness is the average of three measured points on the samples. The radius of the specimen support (a) is 10.0 mm. The Poisson ratio for LSCF6428[4]of 0.30 has been used as an approximation for the Poisson ratio of LSFAl.

The Weibull distribution of probability for failure is plotted by ranking the obtained ball-on-ring results by increasing strength and estimating the probability for failure from:

$$F = \frac{n}{N+1} \tag{G.2}$$

where F is the probability for failure, n is the ranking of each sample and N is the total number of samples. The strength data are then plotted as:

$$ln\left(ln\left(\frac{1}{1-F}\right)\right) = m \times ln(\sigma) - constant \tag{G.3}$$

and the Weibull modulus, m is given by the slope of the curve. The characteristic strength may be found from the intercept with the x-axis.

[4]Kimura et al. Influences of Temperature and Oxygen Partial Pressure on Mechanical Properties of $La_{0.6}Sr_{0.4}Co_{1-y}Fe_yO_{3-\delta}$, *J. Am. Ceram. Soc.* **95** [8] 2608-2613 (2012)

The standard deviations for the Weibull modulus, S_m, and the characteristic strength, S_{σ_0}, are estimated from[5]:

$$S_m = \frac{m}{\sqrt{n}} \tag{G.4}$$

$$S_{\sigma_0} = \frac{\sigma_0}{m\sqrt{n}} \tag{G.5}$$

Table G.1: Fracture strength found from ball-on-ring strength test

Sample ID	t_1 [mm]	t_2 [mm]	t_3 [mm]	Max load, P [N]	Radius, r [mm]	Fracture strength [MPa]
1	0.878	0.895	0.854	3.85	11.67	13,19
2	0.814	0.828	0.825	2.49	12.53	9,76
3	1.152	1.180	1.065	4.77	12.09	9,15
4	0.952	0.960	0.962	3.05	12.88	8,47
5	1.050	1.023	1.027	3.78	12.84	8,86
6	0.950	0.953	0.973	3.45	11.99	9,62
7	0.848	0.940	0.833	2.72	12.44	9,31
8	1.116	1.128	1.127	3.9	12.23	7,74
9	0.904	0.962	0.898	3.55	11.79	10,84
10	0.835	0.828	0.846	3.34	11.99	12,65
11	0.779	0.787	0.781	2.35	12.77	10,28

[5]de With G. *Structure, Deformation, and Integrity of Materials: Volume I: Fundamentals and Elasticity*, John Wiley & Sons, 2006

Appendix H

EDS analysis - result graphs from software

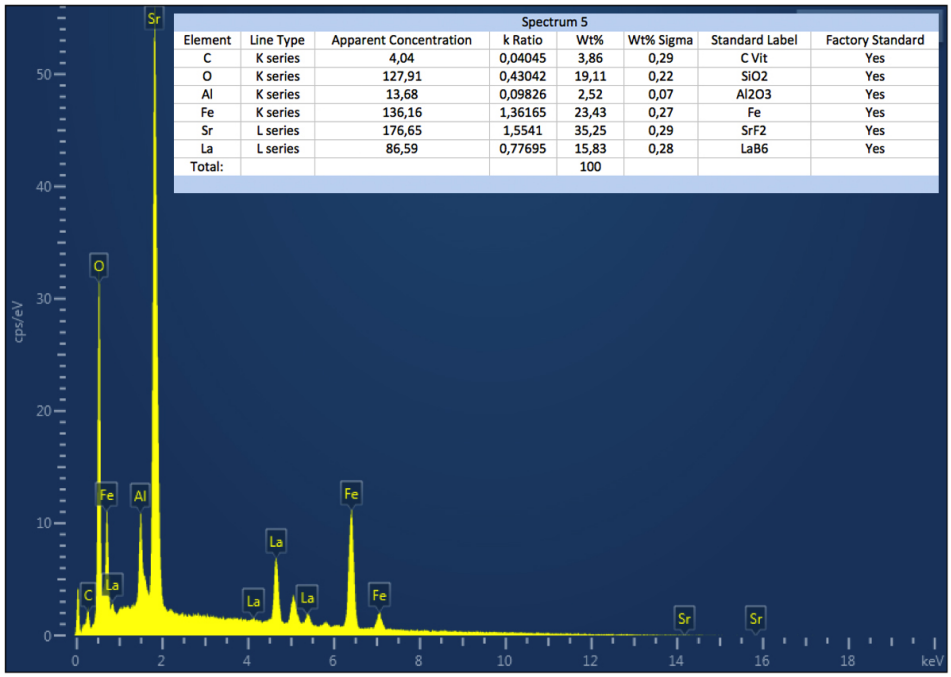

Figure H.1: Result spectrum - Spectrum point 5

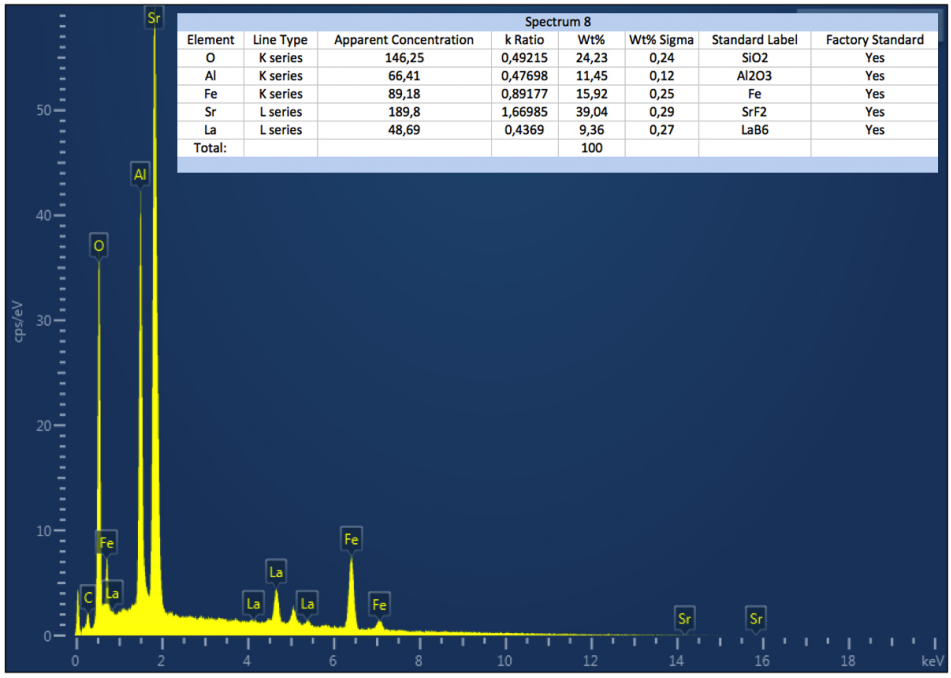

Spectrum 8

Element	Line Type	Apparent Concentration	k Ratio	Wt%	Wt% Sigma	Standard Label	Factory Standard
O	K series	146,25	0,49215	24,23	0,24	SiO2	Yes
Al	K series	66,41	0,47698	11,45	0,12	Al2O3	Yes
Fe	K series	89,18	0,89177	15,92	0,25	Fe	Yes
Sr	L series	189,8	1,66985	39,04	0,29	SrF2	Yes
La	L series	48,69	0,4369	9,36	0,27	LaB6	Yes
Total:				100			

Figure H.2: Result spectrum - Spectrum point 8

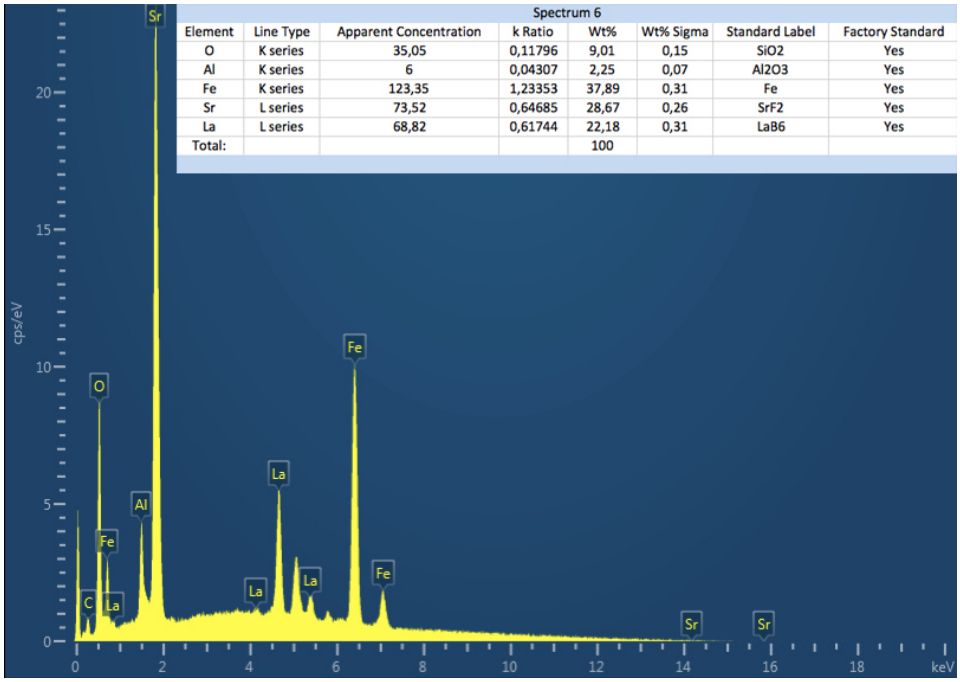

Spectrum 6

Element	Line Type	Apparent Concentration	k Ratio	Wt%	Wt% Sigma	Standard Label	Factory Standard
O	K series	35,05	0,11796	9,01	0,15	SiO2	Yes
Al	K series	6	0,04307	2,25	0,07	Al2O3	Yes
Fe	K series	123,35	1,23353	37,89	0,31	Fe	Yes
Sr	L series	73,52	0,64685	28,67	0,26	SrF2	Yes
La	L series	68,82	0,61744	22,18	0,31	LaB6	Yes
Total:				100			

Figure H.3: Result spectrum - Spectrum point 6